TECHNICAL REPORT STANDARD TITLE PAGE

1. Report No.	2. Government Accession No.	3. Recipient's Catalog No.

4. Title and Subtitle
EVALUATION OF A PRESTRESSED PANEL, CAST-IN-PLACE CONCRETE BRIDGE

5. Report Date
September 1972

6. Performing Organization Code

7. Author(s)
Eugene Buth
Howard L. Furr
Harry L. Jones

8. Performing Organization Report No.
Research Report 145-3

9. Performing Organization Name and Address
Texas Transportation Institute
Texas A & M University
College Station, Texas 77843

10. Work Unit No.

11. Contract or Grant No.
Research Study 2-5-70-145

12. Sponsoring Agency Name and Address
Texas Highway Department
11th and Brazos
Austin, Texas 78701

13. Type of Report and Period Covered
Interim - September 1970
September 1972

14. Sponsoring Agency Code

15. Supplementary Notes Research performed in cooperation with DOT, FHWA.
Research Study Title: "A Study of Prestressed Panels and Composite Action in Concrete Bridges Made of Prestressed Beams, Prestressed Sub-deck Panels, and Cast-in-Place Deck

16. Abstract A relatively new type of beam and slab bridge which makes use of precast, prestressed panels as part of the slab was investigated. In this type of bridge construction, the panels are placed to span between the beams and serve as forms for the cast-in-place portion of the deck. They remain in place to become an integral part of the continuous structural slab. Composite action is obtained in the structure by bonding the prestressed elements together with the cast-in-place portion of the deck. This type of structure incorporates unproven structural details--the bonding of concrete at the interfaces and the inclusion of panel butt joints.

The purpose of this study was to experimentally and theoretically investigate the ability of this type of structure to distribute wheel loads in a satisfactory manner and to behave as a composite unit.

A full-scale, simple span, prestressed panel type bridge was structurally tested in the laboratory. The bridge was subjected to cyclic applications of design loads and finally to static failure loads. It performed satisfactorily under all load conditions.

On the basis of information developed in this study, it was concluded that the use of prestressed panels is a suitable method of highway bridge construction.

17. Key Words	18. Distribution Statement
bridge, prestressed concrete, precast concrete panels, slab, repetitive loads, ultimate load, composite action	

19. Security Classif. (of this report)	20. Security Classif. (of this page)	21. No. of Pages	22. Price
Unclassified	Unclassified	151	

Form DOT F 1700.7 (8-69)

EVALUATION OF A PRESTRESSED PANEL, CAST-IN-PLACE CONCRETE BRIDGE

by

Eugene Buth
Assistant Research Engineer

Howard L. Furr
Research Engineer

Harry L. Jones
Engineering Research Associate

Texas Transportation Institute
Texas A&M University
College Station, Texas

and

A. A. Toprac
Center for Highway Research
The University of Texas
Austin, Texas

Research Report 145-3

A Study of Prestressed Panels and Composite Action in Concrete Bridges Made of Prestressed Beams, Prestressed Sub-deck Panels, and Cast-in-place Deck

Research Study Number 2-5-70-145

Sponsored by

The Texas Highway Department

in cooperation with the
United States Department of Transportation
Federal Highway Administration

September 1972

ABSTRACT

A relatively new type of beam and slab bridge which makes use of precast, prestressed panels as part of the slab was investigated. In this type of bridge construction, the panels are placed to span between the beams and serve as forms for the cast-in-place portion of the deck. They remain in place to become an integral part of the continuous structural slab. Composite action is obtained in the structure by bonding the prestressed elements together with the cast-in-place portion of the deck. This type of structure incorporates unproven structural details--the bonding of concrete at the interfaces and the inclusion of panel butt joints.

The purpose of this study was to experimentally and theoretically investigate the ability of this type of structure to distrubute wheel loads in a satisfactory manner and to behave as a composite unit.

A full-scale, simple span, prestressed panel type bridge was structurally tested in the laboratory. The bridge was subjected to cyclic applications of design loads and finally to static failure loads. It performed satisfactorily under all load conditions.

On the basis of information developed in this study, it was concluded that the use of prestressed panels is a suitable method of highway bridge construction.

Key Words: bridge, prestressed concrete, precast concrete panels, slab, repetitive loads, ultimate load, composite action.

SUMMARY

A single span full-scale prestressed panel type bridge was evaluated experimentally in the laboratory and theoretical studies of the structure were made. The structure was subjected to cyclic applications of design load plus impact and to static failure loads. It performed satisfactorily under all test conditions.

Two million applications of simulated design axle load plus impact were accomplished at three locations on the bridge structure. The bond at the interface between the prestressed panels and the cast-in-place concrete performed without any indication of distress under these cyclic loads.

Two million cycles of design wheel load plus impact alternating on opposite sides of an panel butt joint were applied at one location on the structure without causing distress. Satisfactory performance was exhibited by the bridge slab when subjected to static failure loads. The lowest value of cracking load measured experimentally was 3.8 times the design wheel load plus impact, and the lowest measured ultimate load was 12.5 times the design wheel load plus impact.

The failure surfaces that developed in the static failure tests intersected and continued across the panel to cast-in-place interface and was not influenced by the interface.

The theory presented by Westergaard (the basis of present design specifications) predicts local bending stresses in the slab of the structure with reasonable accuracy if in-plane stresses resulting

from spanwise bending of the entire structure are ignored. An elastic analysis of the structure, including in-plane as well as bending effects was developed for comparison with strains and displacements measured in the bridge.

The following conclusions were drawn from the results of the theoretical and experimental work reported herein.

1. The bond at the interface between the prestressed, precast panels and the cast-in-place concrete performed without any indication of distress under cyclic design loads and static failure loads.
2. Wheel loads were transferred and distributed across transverse panel joints in a satisfactory manner.
3. It is feasible to design for composite action in a prestressed panel bridge of the type studied.

IMPLEMENTATION STATEMENT

It has been demonstrated in the laboratory that a full-scale simple span prestressed panel bridge performed satisfactorily under cyclic applications of design axle and wheel loads and under static failure loads. Comparisons between experimental data and the theory of the AASHO Code indicate that present design practices are satisfactory for prestressed panel bridges.

Some cracking occurred in the upper surface of the cast-in-place portion of the slab above the panel butt joints. This cracking occurred in areas of the slab that had not been loaded as well as in loaded areas. It did not increase with application of cyclic loads and is apparently no serious problem.

The prestressed panel bridge slab does not meet the AASHO requirements for longitudinal distribution steel and considerations should be given to practical means of meeting these requirements. A proven service record exists for structures designed in accordance with AASHO and meeting these requirements would add to the assurance that a prestressed panel bridge slab would perform satisfactorily.

TABLE OF CONTENTS

LIST OF FIGURES

LIST OF TABLES

I. INTRODUCTION

This report describes the laboratory study phase of a three-year investigation of highway bridges constructed with prestressed concrete I-beams, prestressed panel subbdeck and a cast-in-place slab. This type of construction, shown in Figure 1, has certain relatively new features which reduce construction time and cost.

The precast panels serve as forms for the cast-in-place portion of the deck and remain in place to become an integral part of the deck. This feature eliminates the installation and removal of forms and falsework on the underside. The cast-in-place deck is mechanically connected to the beams by the beam stirrups which extend into the deck in the same way as in conventional construction.

The cast-in-place concrete is placed over the surface of the panels and into the space above the beams, thereby bonding all elements together to act as a composite unit. The cast-in-place concrete serves as the riding surface of the deck.

Two major deviations from established practices exist in a prestressed panel type bridge. One is bonding of a new concrete to old concrete with sufficient strength to develop an adequate structural connection at the interface. The other is the inclusion of transverse joints made by butting adjacent prestressed panels together. The latter created some question as to the capacity of the slab to accomplish longitudinal distribution of wheel loads and to resist internal stresses. This transverse joint extends from top to bottom

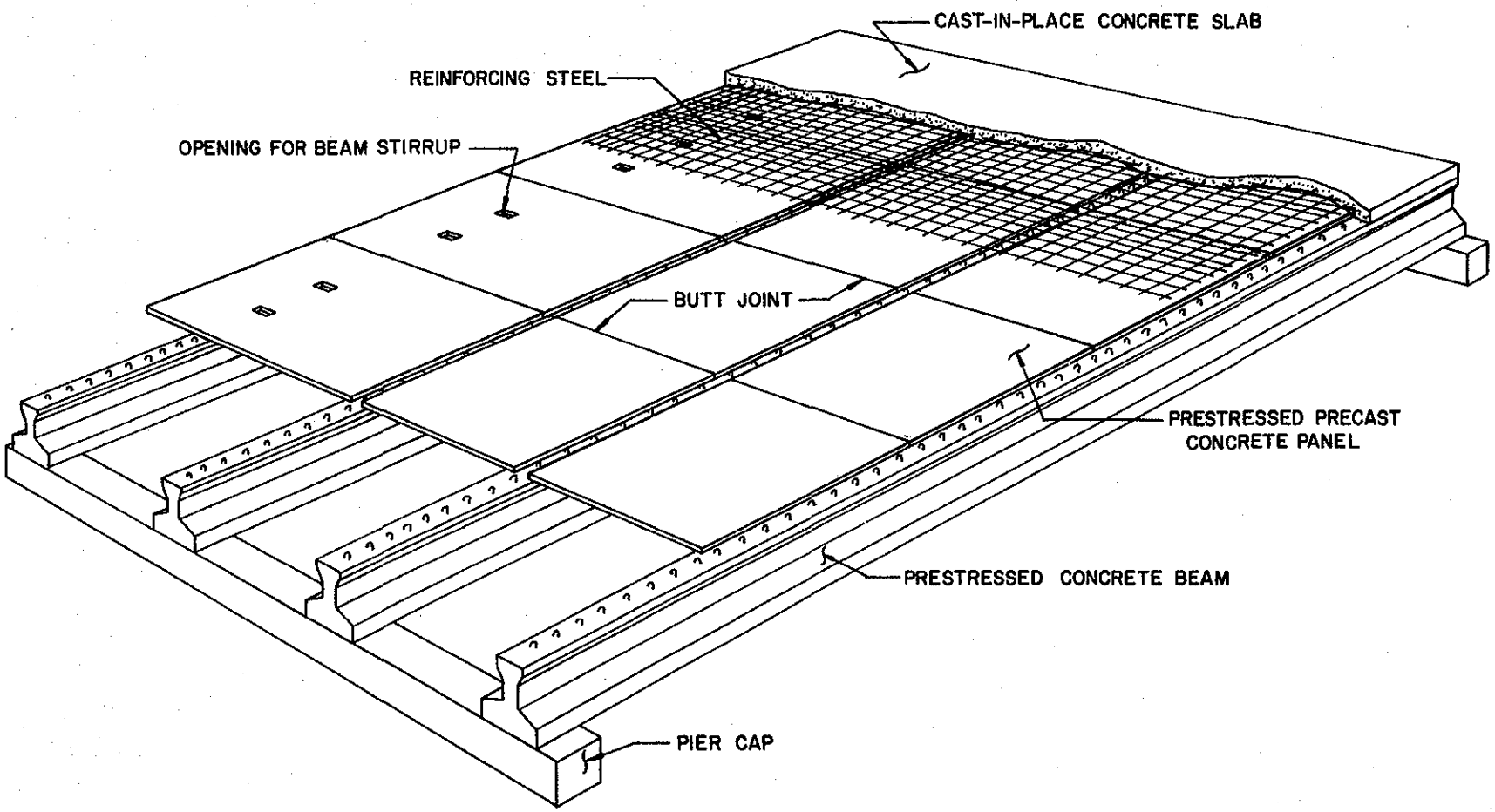

Figure 1. Cut-away View of Prestressed Panel Type Bridge.

of the prestressed panels. It does not extend into the cast-in-place concrete. Present governing specifications, written by the American Association of State Highway Officials (AASHO) (1), do not deal directly or by implication with these two structural details. This report describes the results of an experimental and theoretical investigation of the ability of this type of structure to distribute wheel loads in a satisfactory manner and to behave as a composite unit.

1.1 Related Previous Work

Three bridges of this type were built in Texas in the early 1960's and have been serving satisfactorily since that time. Two of these bridges, located on U.S. Highway 75 in Grayson County, Texas, were examined in the first phase of this study. A visual inspection was conducted and crack patterns on the deck surface were mapped for both bridges. Load tests were performed and core samples were taken from one of the bridges to determine the condition of the bond between prestressed panels and cast-in-place deck. This examination indicated no distress in the bridges nor any signs of bond failure. The details of the study are contained in Research Report 145-1, "Study of In-Service Bridges Constructed With Prestressed Panel Sub-Decks." (2)

The prestressed panels in those bridges in Texas already completed or under construction are typically 3 1/2 in. thick, 4 to 6 ft. wide, and range in length from 5 1/2 to 7 ft. for panels between interior

beams. Prestressing strands are placed in the longitudinal direction of the panels. The question of development length of strands in such short members and the effects of cyclic loads on development length was examined in the second phase of this study. An investigation of 20 specially instrumented panels indicated that for strands prestressed with an initial stress of 162 ksi, 22 in. of development length was required for 3/8 in. diameter strands and 34 in. for 1/2 in. strands. The performance of a typical panel in a bridge structure with these development lengths was examined analytically, and found to perform satisfactorily. The details of this second phase of the study are contained in Research Report 145-2, "Development Length of Strands in Pretressed Panel Sub-Decks." (3)

Sinno and Furr (4) conducted tests in the laboratory to determine the direct shear strength of the bond of new concrete cast on the surface of older concrete. In some tests, the old surface was simply cleaned with water using a hose and nozzle, then damp dried prior to placement of the new concrete. Results of these tests indicated direct shear strengths between the old and new concrete of about 200 psi. In other tests, the old surface was cleaned in the same manner as above and grout was thoroughly brushed on it to aid in bonding the new concrete. Direct shear strengths of 400 to 500 psi were obtained in these tests.

In 1971 Nosseir and Murtha (5) reported the results of tests conducted on eight prestressed concrete split beams. These beams were composite beams constructed by casting concrete onto the

previously cast prestressed portion of the beam. The geometry of the cross section was such that the interface coincided with the neutral surface of the composite section. Ultimate horizontal shear strengths in excess of 400 psi were obtained in beams with smooth interfaces. The effect of a rough interface was to increase the strength by about 100 psi.

1.2 Objective and Plan of Research

The objective of the final phase of this study was to investigate the feasibility of designing for composite action in a highway bridge constructed of prestressed beams, prestressed panel sub-deck, and cast-in-place deck. The research program consisted of theoretical and experimental studies.

In the experimental study a full-scale, single span bridge and a slab segment model were structurally tested in the laboratory. The full-scale bridge was designed and constructed in accordance with applicable sections of the AASHO and Texas Highway Department (THD) Specifications (6). The structure was nominally 23 ft. wide and spanned 50 ft. It was subjected to simulated cylic axle loads representing a design truck axle, and to simulated cyclic wheel loads alternating on either side of a panel butt joint to represent a design truck wheel load rolling across a panel butt joint. The bridge was finally subjected to static failure wheel loads at locations adjacent to selected panel butt joints.

The slab segment model consisted of two prestressed panels

supported on spandrel beams, covered with a cast-in-place slab. The model was subjected to simulated cyclic wheel loads alternating on either side of the butt joint between panels, and then loaded to failure.

The response of the full-scale bridge to static wheel loads was predicted using an elastic analysis, which assumed complete composite action between slab, panels and beams in order to obtain an accurate prediction of strains at any point on the surface of the prestressed panel-cast-in-place deck slab or the prestressed beams.

Electrical resistance strain gages and mechanical displacement gages were installed at various locations on the full-scale bridge model to monitor its response to static, simulated wheel loads. Measured strains and deflections were then compared with values from the analysis of the elastic fully composite structure, and discrepancies between measured and predicted values were sought that would indicate a lack of composite action in the full-scale bridge.

II. EXPERIMENTAL PROGRAM

The experimental segment of this study consisted of simulated wheel loads, applied both statically and dynamically, to a full-scale bridge structure and to a slab segment model constructed from two prestressed panels. After completion of service load testing, the structures were loaded to failure to determine ultimate capacity. Structural response to static loads was measured with electrical resistance strain gages and mechanical displacement gages.

2.1 Full-scale Bridge Model

The full-scale test structure consisted of two simulated bent caps; four prestressed THD Type B beams; 3 1/4-in. thick, prestressed panel subdeck; and conventionally reinforced 3 1/2-in. thick cast-in-place deck. A layout of the structure is given in Figure 2, and Figure 3 is a photograph of the complete structure and testing facility. The 23-ft. wide, 50-ft. long structure, complete except for side rails, simulated two lanes of a four-lane bridge. The deck contained two types of panels; interior panels and exterior panels. Interior panels spanned between prestressed beams and were supported at each end by the top flange of a beam. The exterior panels were supported at one end on a beam and were continuous over the outside beam, with an overhang of approximately 2 ft.-6 in. The panels became an integral part of the continuous structural deck when the top portion of the deck was cast.

The entire structure was designed in accordance with AASHO

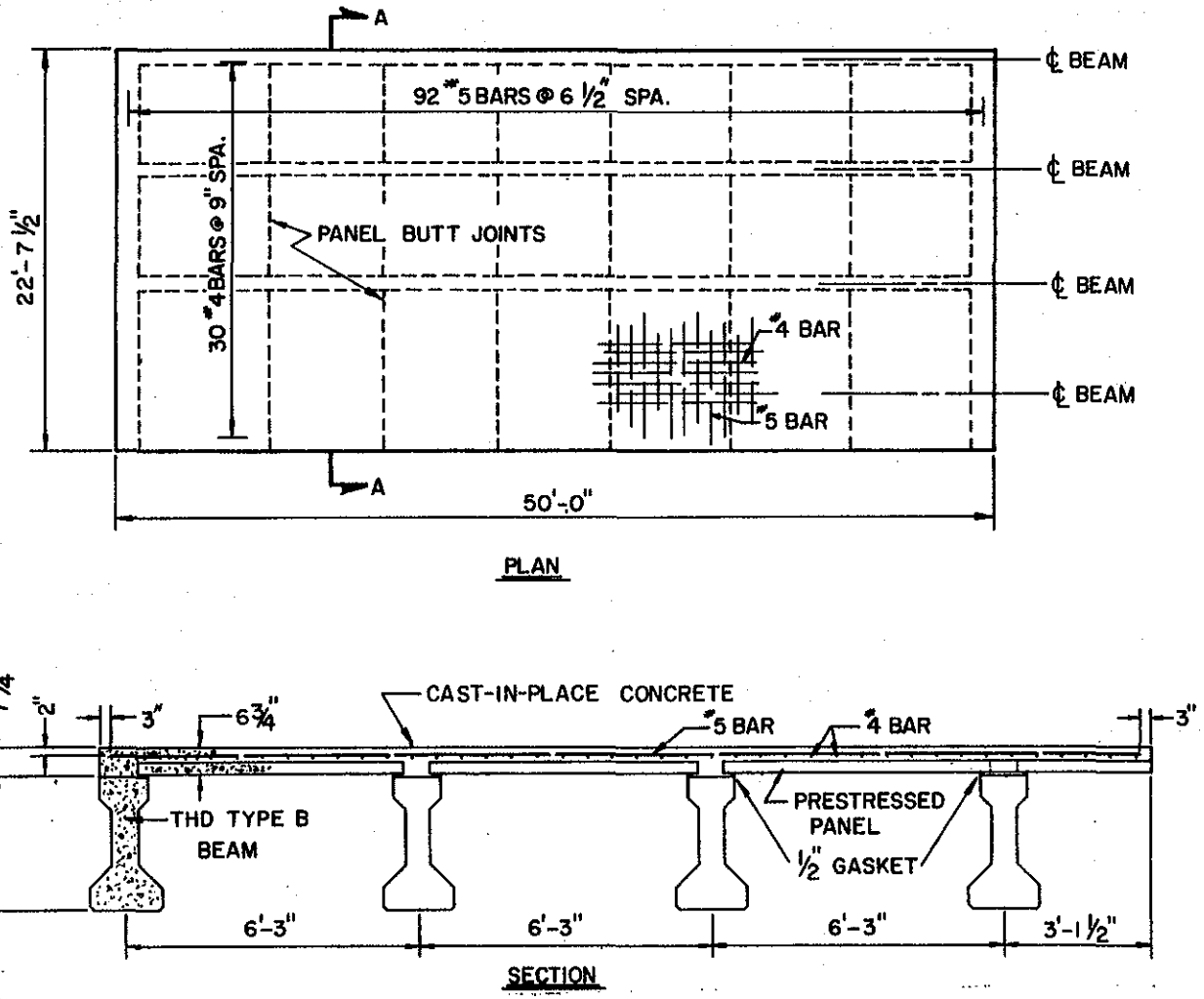

Figure 2. Prestressed Panel Type Bridge Tested in This Study.

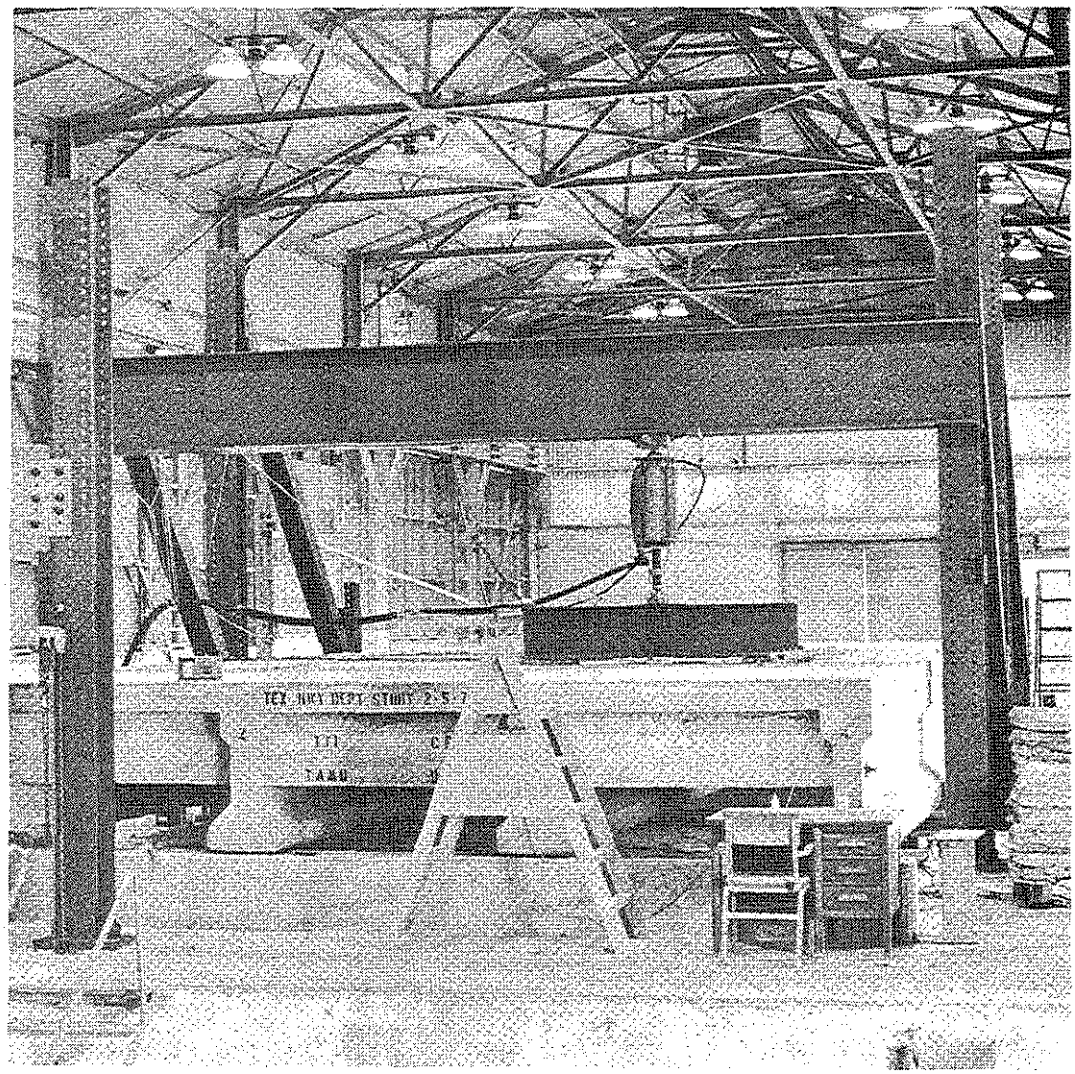

Figure 3. Full-scale Test Bridge and Loading Equipment.

specifications, where applicable, for an HS20-44 loading. The design of the beams was the same as for conventional construction, but one special consideration was necessary in their fabrication. It was necessary to finish the outer portions of the upper surface of the top flange sufficiently smooth to receive the gasket indicated in Figure 2. The dimensions and details of the reinforcement for the beams are given in Figures 4 and 5. The construction loads were carried by the prestressed panels, whereas the AASHO design moment of 3.77 kip-ft./ft. was carried by the composite deck.

The prestressed panels were joined at their ends by the cast-in-place concrete which engaged a 3-in. extension of prestressing steel over the prestressed beams (Fig. 6). At the outside edge of the bridge where the slab was cantilevered beyond the beam, holes were cast in the panel to allow the vertical steel in the beam to extend into the cast-in-place portion of the slab. These details are shown in Figure 7. The panels were joined at the transverse butt joint by the concrete and reinforcing steel placed on top of them. There was no connection in the plane of the panels at this butt joint. Dimensions and details of the reinforcing steel for the panels are given in Figures 8 and 9.

The calculated transverse bending moment capacities of the deck of the bridge model are given in Table 1. These values were computed using the values of concrete strength (obtained from test specimens) given in Table 2, and a mimimum yield strength of 40 ksi for reinforcing steel. The design of the composite prestressed panel,

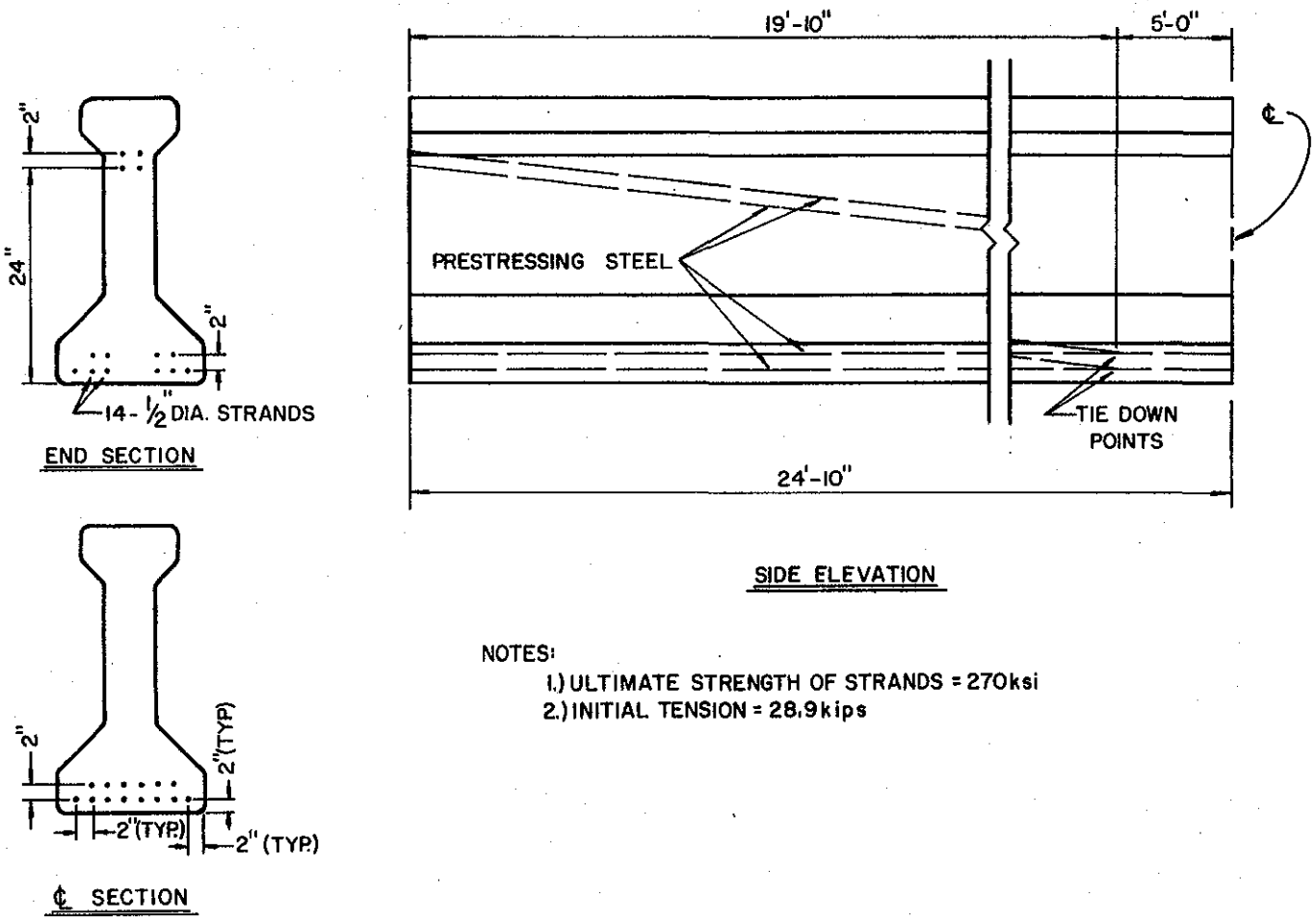

Figure 4. Details of Prestressing Steel in Beams.

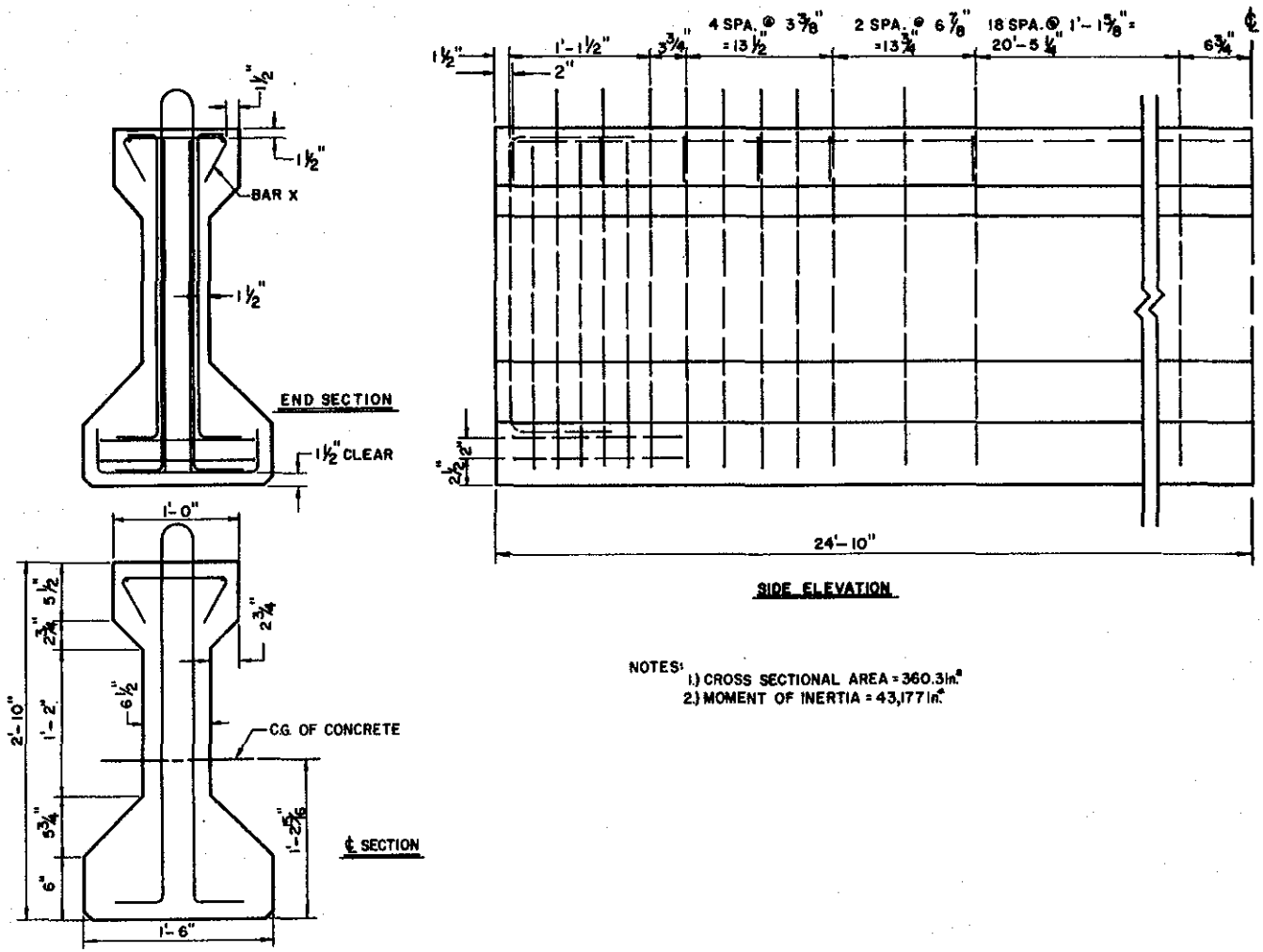

Figure 5. Properties of Beam Cross Section and Details of Conventional Reinforcement.

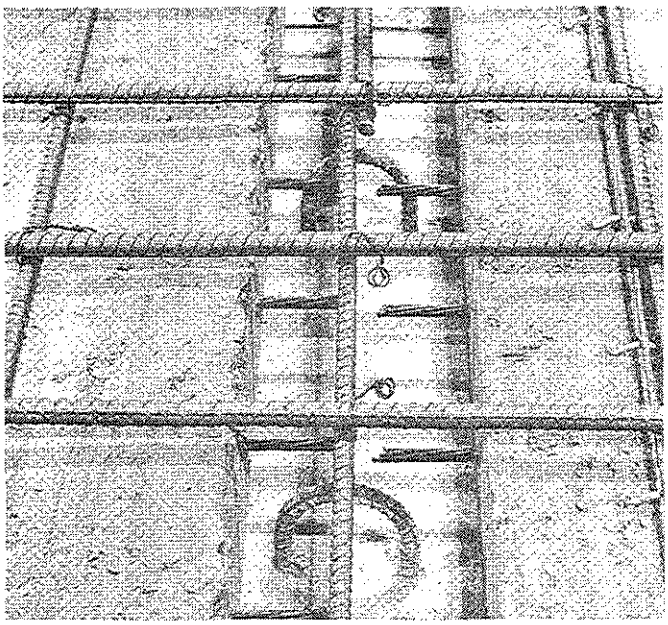

Figure 6. Panel Details at Interior Beam.

Figure 7. Details of Exterior Panel at Exterior Beam.

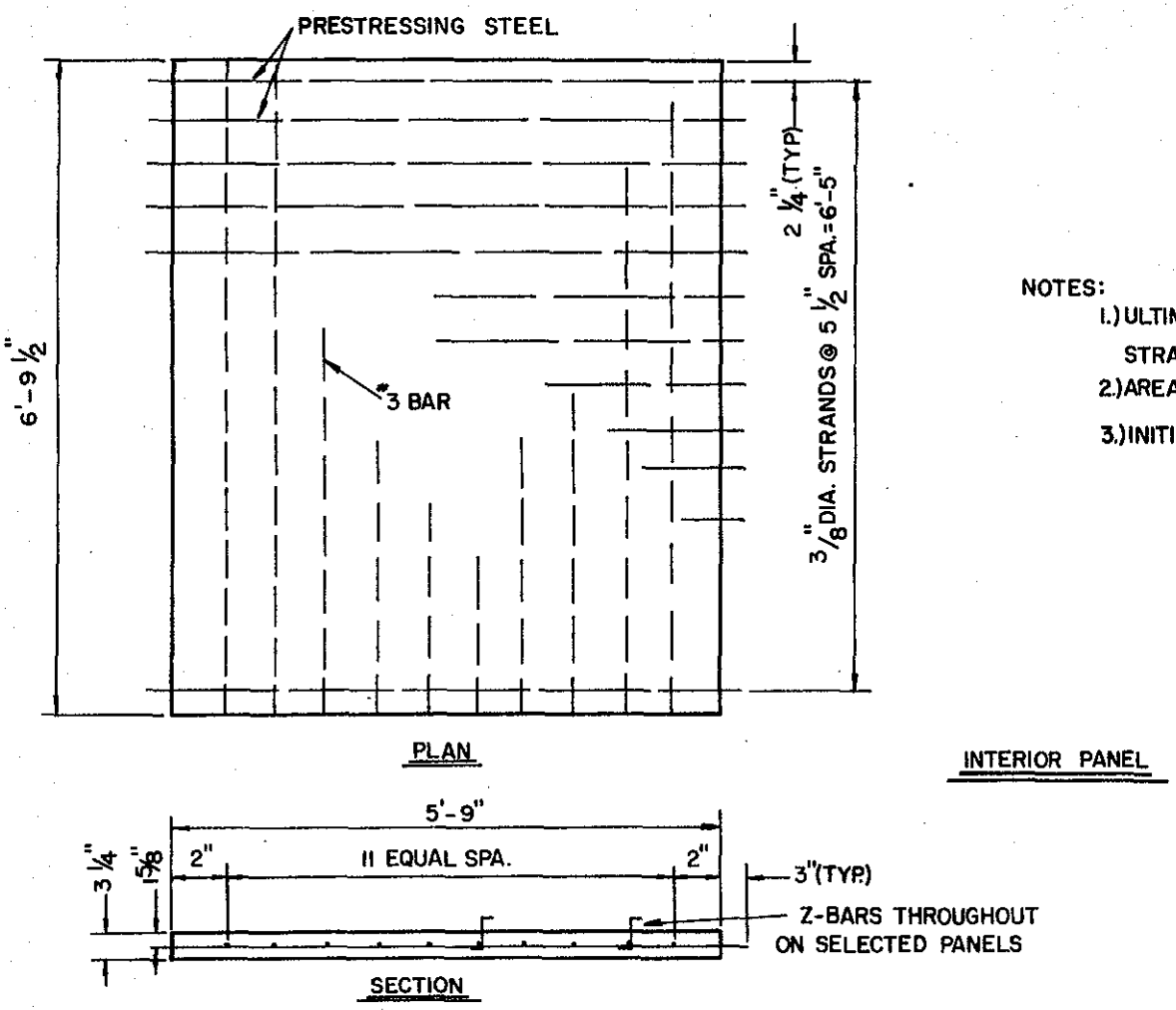

NOTES:

1.) ULTIMATE STRENGTH OF STRANDS = 270 ksi.

2.) AREA OF 3/8" DIA. STRANDS = .08 sq. in.

3.) INITIAL TENSION = 16.1 kips.

Figure 8. Details of Interior Panels Used in Full-scale Bridge.

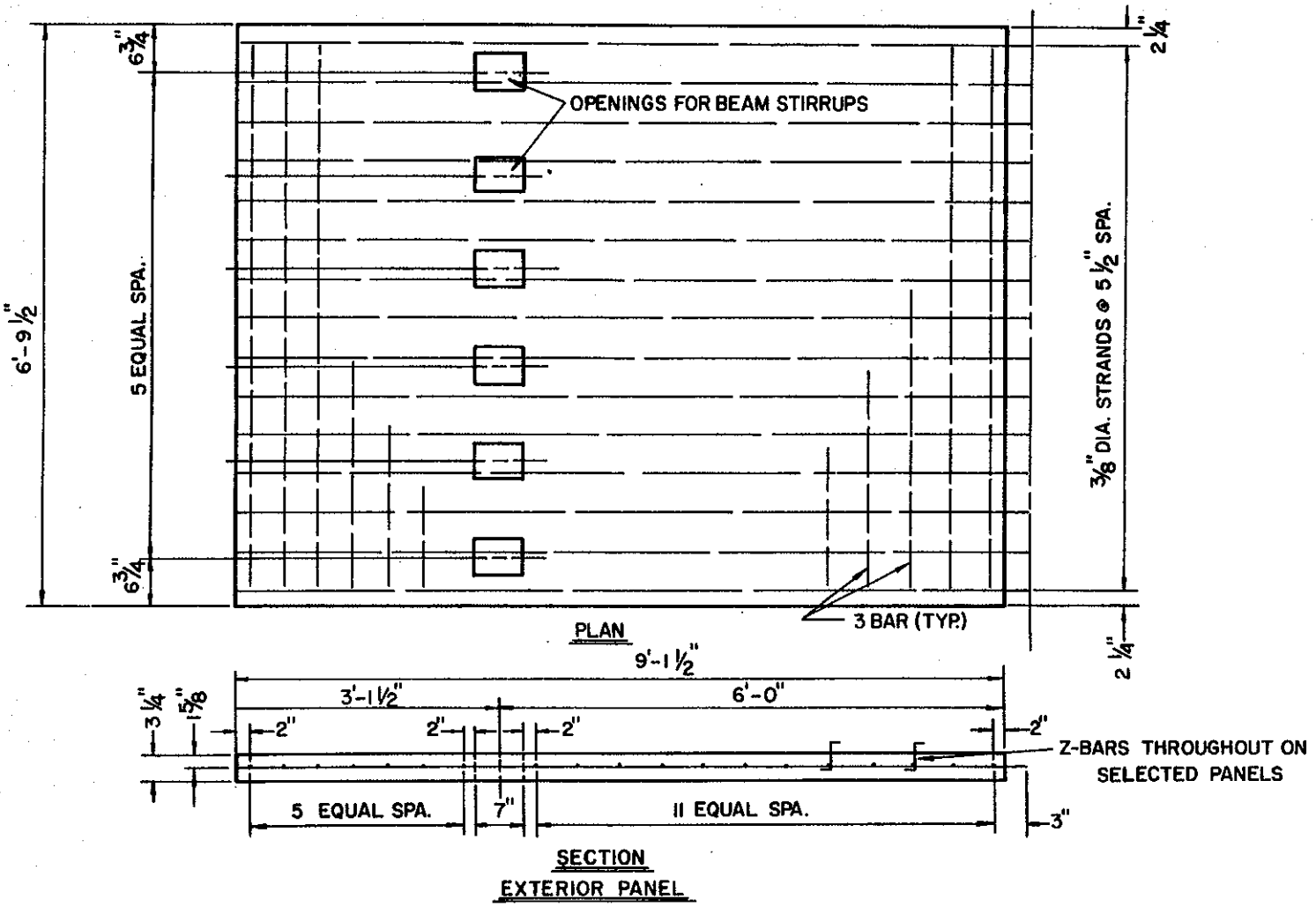

Figure 9. Details of Exterior Panels Used in Full-scale Bridge.

TABLE 1

BENDING MOMENT CAPACITIES OF SLAB

Direction of Bending	Allowable Moment[a] Capacity (kip-ft/ft)	Ultimate Moment[b] Capacity (kip-ft/ft)
Transverse Positive Bending	4.08[c]	18.4
Transverse Negative Bending	4.05	8.67
Longitudinal Positive Bending, Not At Panel Joint	1.72	3.62
Longitudinal Negative Bending, Not At Panel Joint	1.70	3.68
Longitudinal Positive Bending, At Panel Joint	1.16[d]	1.78[d]
Longitudinal Negative Bending, At Panel Joint	1.70	3.68

[a]Calculated in accordance with AASHO Bridge Design Specifications, except f'_c not limited to 4500 psi.

[b]Calculated in accordance with American Concrete Institute 318-71 Building Code.

[c]Maximum moment possible with no net tensile stress in panel.

[d]Calculations based on net section at panel joint. No stress concentration assumed.

TABLE 2

CONCRETE STATISTICS

Item	Date Cast	Fabricator	"Release" Strength (psi)	Compressive Strength (psi) ASTM C 39	Tensile Strength (psi) ASTM C 496	Dynamic Modulus of Elasticity (psi) ASTM C 215
Prestressed Beams	10-29-70 and 10-30-70	Crowe-Gulde Amarillo	4810 4880	7590 @ 28 days and 7130 @ 28 days		6.19×10^6
Prestressed Panels	12-10-70	Span, Inc. Dallas	--[a]	8550 @ 316 days	640 @ 480 days	5.65×10^6
Cast-in-place Deck	2-25-71	TTI[b]		5970 x 240 days	490 @ 400 days	5.23×10^6

[a] Data not available

[b] Texas Transportation Institute

cast-in-place deck was governed by the requirements that: i) under construction loads, no tensile stresses occur in the prestressed panel, ii) the transverse allowable bending moment capacity of the composite section be greater than or equal to the AASHO design moment (3.77 kip-ft./ft.), and iii) no tensile stresses occur in the panel as a result of transverse bending moment on the composite section from service loads. These requirements were satisfied by a 3 1/4 in. thick panel with prestressing as shown in Figure 8, and a 3 1/2 in. thick cast-in-place slab with the transverse reinforcing shown in Figure 2. Although the design thickness of the composite slab was 6 3/4 in., the actual slab measured 7 in., which is within the tolerable limits specified by AASHO and THD. The bending moment capacities shown in Table 1 are based on the measured slab thickness.

The values of longitudinal bending moment capacity of the deck are shown in Table 1. No numerical value of bending moment capacity in the longitudinal direction is specified by AASHO, but adequate capacity in this direction is assured by the requirements of longitudinal distribution steel placed in the bottom of the slab for conventional slab construction. The amount of distribution steel required by the specifications is expressed as a percentage of the main reinforcement and is computed by $220/\sqrt{S}$ with a maximum of 67 percent. This requirement indirectly specifies that the slab be designed to resist a given bending moment in the longitudinal direction and is a conservative approximation of the expression for longitudinal bending moment from plate theory. The ratio of longitudinal to transverse

bending moment, from plate theory, is a function of slab span length, and its maximum value is about 67 percent for a span of 6 ft. (7). This ratio decreases for span lengths either greater or less than this value. By AASHO specifications, the maximum value of 67 percent would control for the test structure. The use of prestressed panels precluded the placement of longitudinal distribution steel in its intended position. Instead, a lesser amount of steel (No. 4 bars at 9 in. spacing) was laid on the surface of the prestressed panels, beneath the No. 5 transverse reinforcing bars (Figs. 6 and 7). Two values are shown in Table 1 for positive longitudinal moment capacity. One set of values was obtained for locations other than a panel butt joint. In this case, the full composite slab thickness of 7 in. was used in the computations. The other set of values pertain to a section through a butt joint. Here, only the depth of the cast-in-place slab is effective in resisting positive bending moments. For positive moment capacity, the longitudinal No. 4 bars were assumed to be effective as flexural reinforcement, although their effectiveness in this capacity would be greatly reduced by any deterioration of the upper surface of the slab. The full depth of the composite section was used to compute the negative moment capacity over a butt joint. The nature of edge surfaces on adjacent panels at a joint make this assumption questionable. Most likely, only those portions of the edges that are in immediate contact with one another along with the cast-in-place deck are effective for negative moment resistance. No account was taken of stress concentrations, which undoubtably exist,

in the computation of moment capacity.

It was assumed in the design that all elements of the structure would act as a composite unit. This assumption required that all elements of the structure be bonded together in a suitable manner to transfer all stresses across the interface between the cast-in-place deck and the prestressed panels and at the slab to beam interfaces. At the latter locations, the same proven methods that are used in conventional beam and slab bridges were employed. Three methods, used as test variables, were employed to bond the cast-in-place concrete to the top surface of the prestressed panels. Z-bars, detailed in Figure 10, were used to provide both shear and tensile bond over a selected portion of the deck. In another area, portland cement grout was thoroughly brushed onto the rough surfaces of the panels to serve as a bonding agent (Fig. 11). The cast-in-place deck was placed over the grout. There was no special treatment over the remainder of the deck (Fig. 12). The locations of these areas on the structure are shown in Figure 13. The surface of the panels was thoroughly cleaned with water from a hose and nozzle and then damp dried shortly before placement of the cast-in-place concrete. The grout, on the selected panels, was applied immediately prior to concrete placement. The progress of the grout brushing operation was regulated so that the grout did not dry prior to placement of the concrete.

At selected transverse butt joints, dowel bars were placed on the surface of the panels and extended across the butt joint (Fig. 14). They were intended to aid in transferring a wheel load across the panel

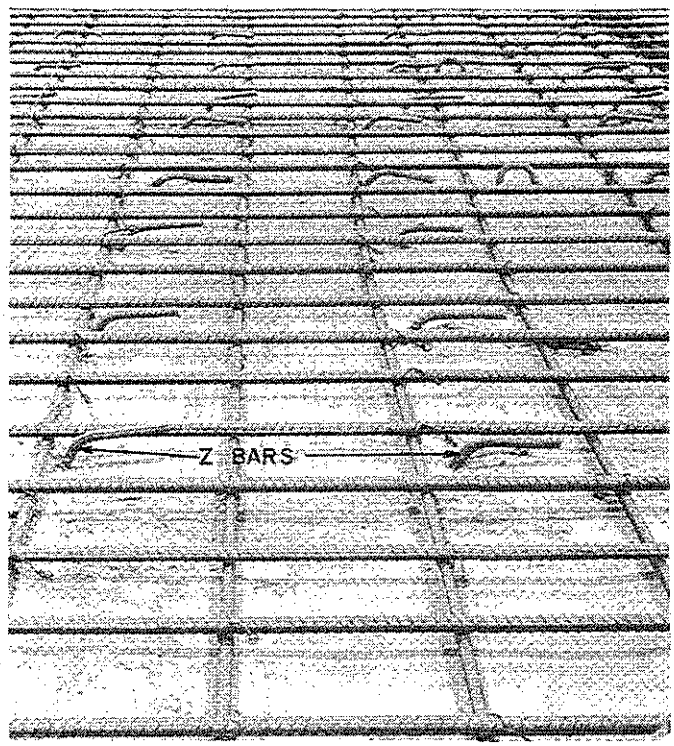

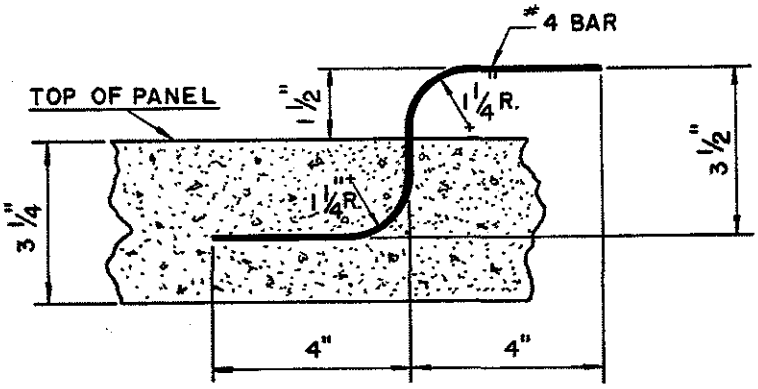

Figure 10. Z-bars Used in Selected Panels to Aid in Providing Structural Connection between Panel and Cast-in-place Deck.

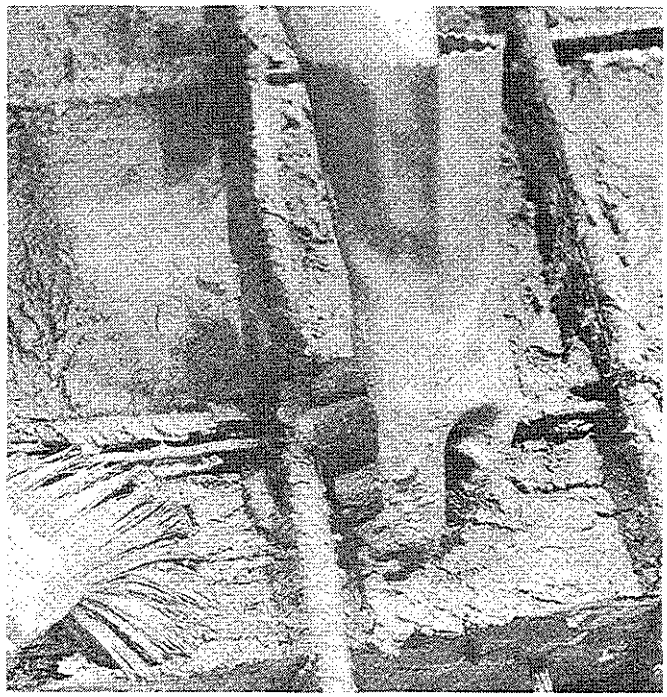

Figure 11. Grout Being Brushed onto Surface of Panel.

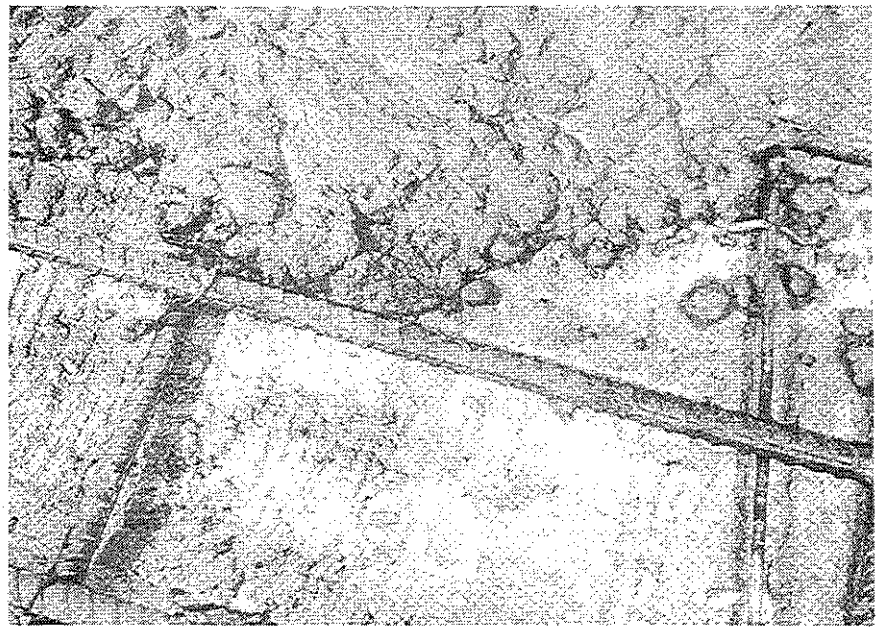

Figure 12. Concrete Being Placed on "Non-grouted" Panel.

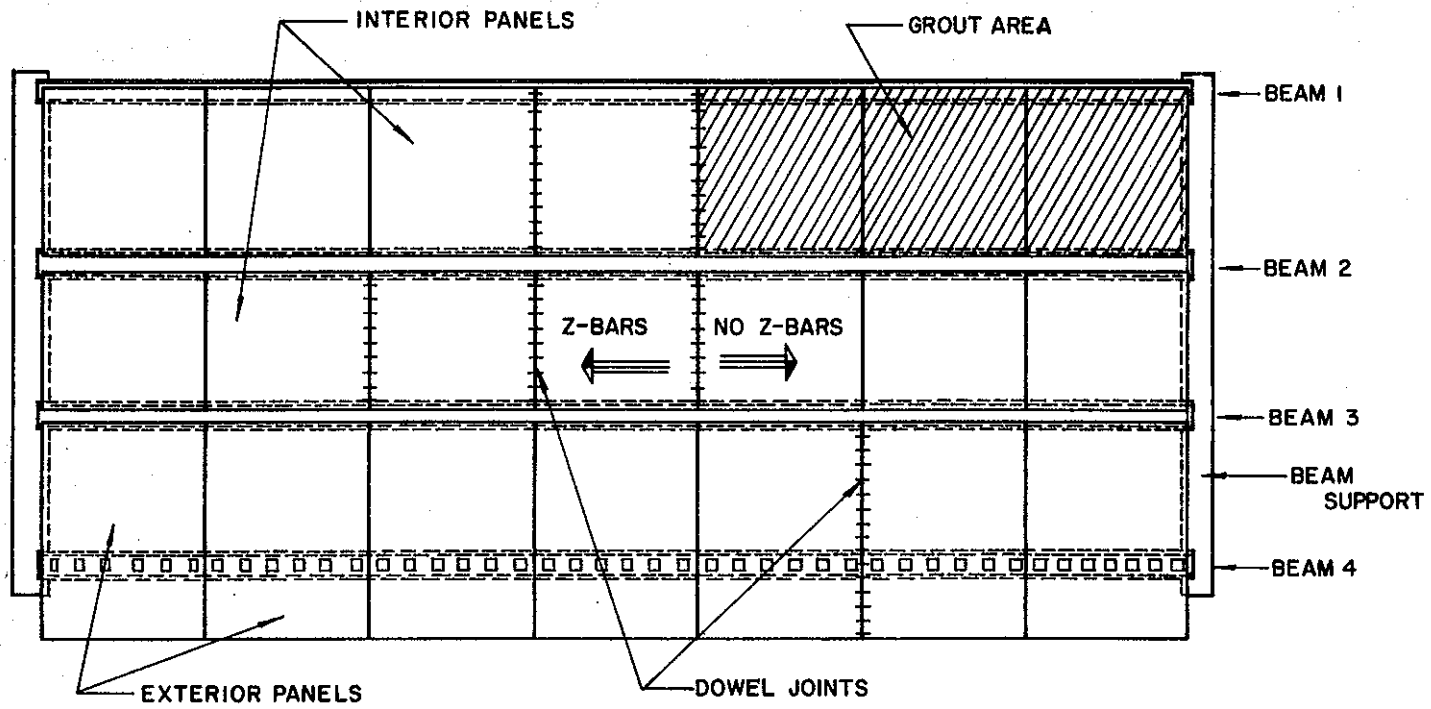

Figure 13. Location and Identification of Various Structural Details in Full-scale Bridge.

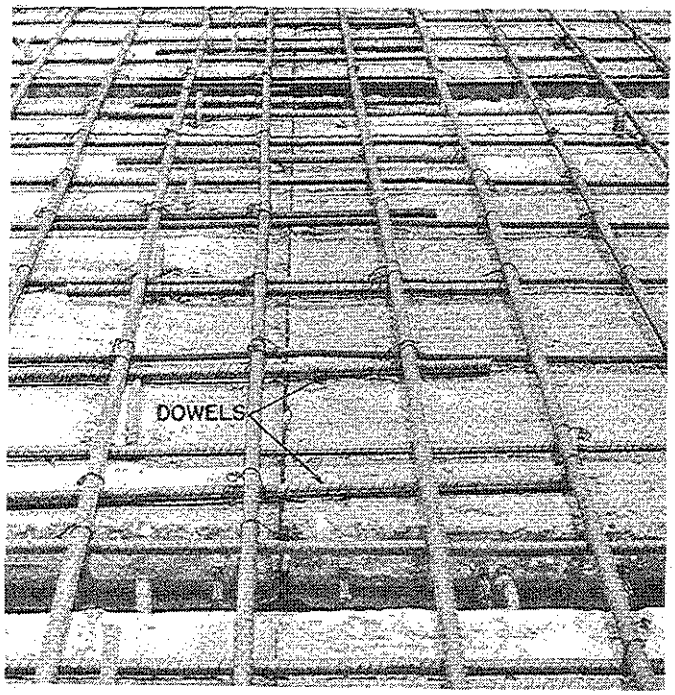

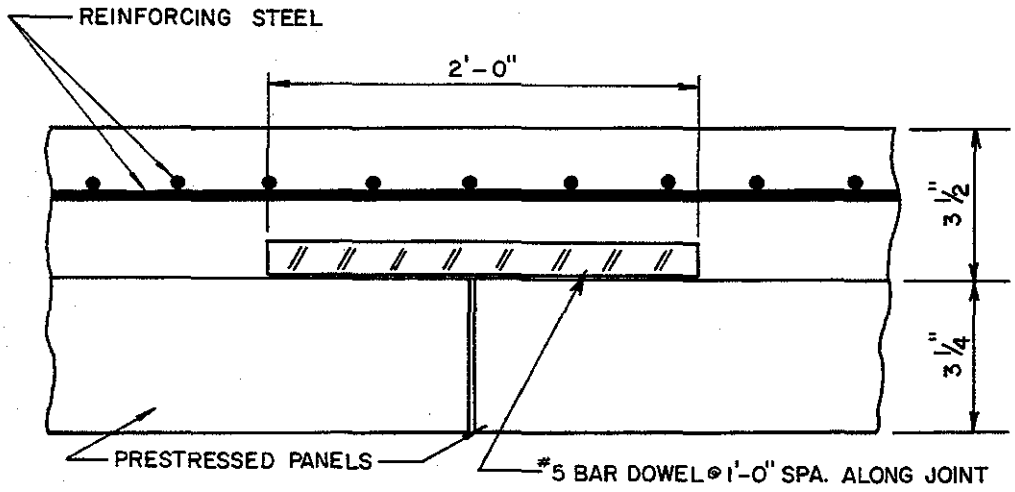

Figure 14. Dowel Bars Used at Selected Panel Butt Joints.

joint and distributing it in the longitudinal direction of the bridge. The joints where dowels were used are also indicated in Figure 13.

2.2 Slab Model

The slab segment model shown in Figure 15 was used to evaluate a panel butt joint reinforcing detail proposed for use on a bridge on IH 635 near Dallas, Texas. Figure 16 shows the mechanical connectors embedded in the two prestressed panels which made up the model. This detail was indentical to the dowel bar detail used in the full-scale bridge model (see Figs. 13 and 14), in that Z-bars and dowel bars were both used. In addition, a No. 4 bar was bent into loops and embedded parallel to and 6 in. from each edge of the panel, as indicated by the V-bars in Figure 16. The dowel bars were layed across the joint through these loops to provide additional anchorage (see Fig. 17). The two prestressed panels rested on sill beams which resisted rotation of the slab, as would occur if they were an integral part of a bridge structure. A 4 1/2 in. thick deck was cast on the panels.

2.3 Instrumentation of Full-scale Bridge Model

Instrumentation was planned to detect a breakdown in the overall performance of the full-scale bridge model and to reveal any local failure that might develop in the vicinity of the applied loads. The structure was instrumented using mechanical gages for measuring deflection and for detecting relative movement between elements, and electrical resistance gages for measuring strains in the beams and deck.

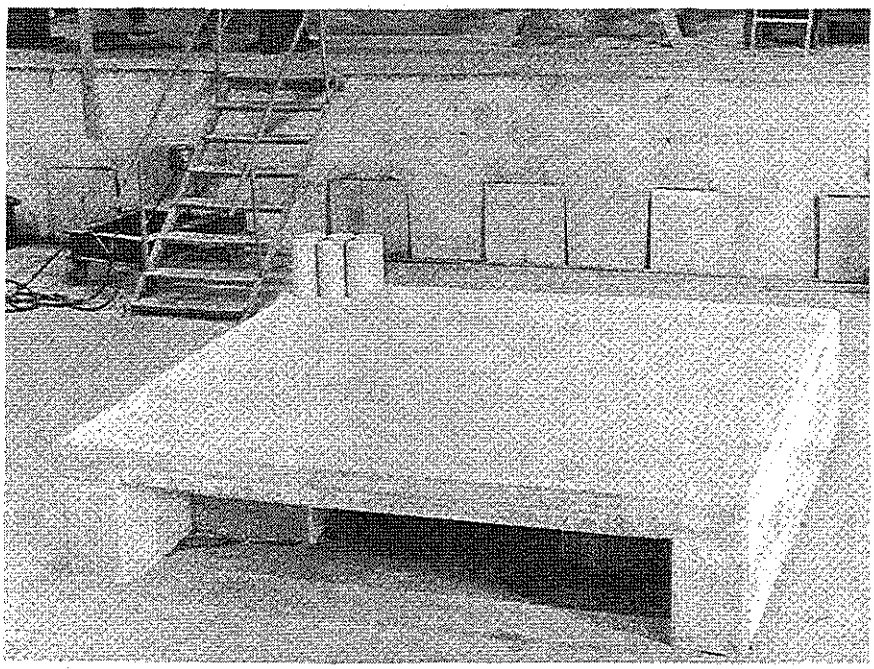

Figure 15. Slab Segment Model.

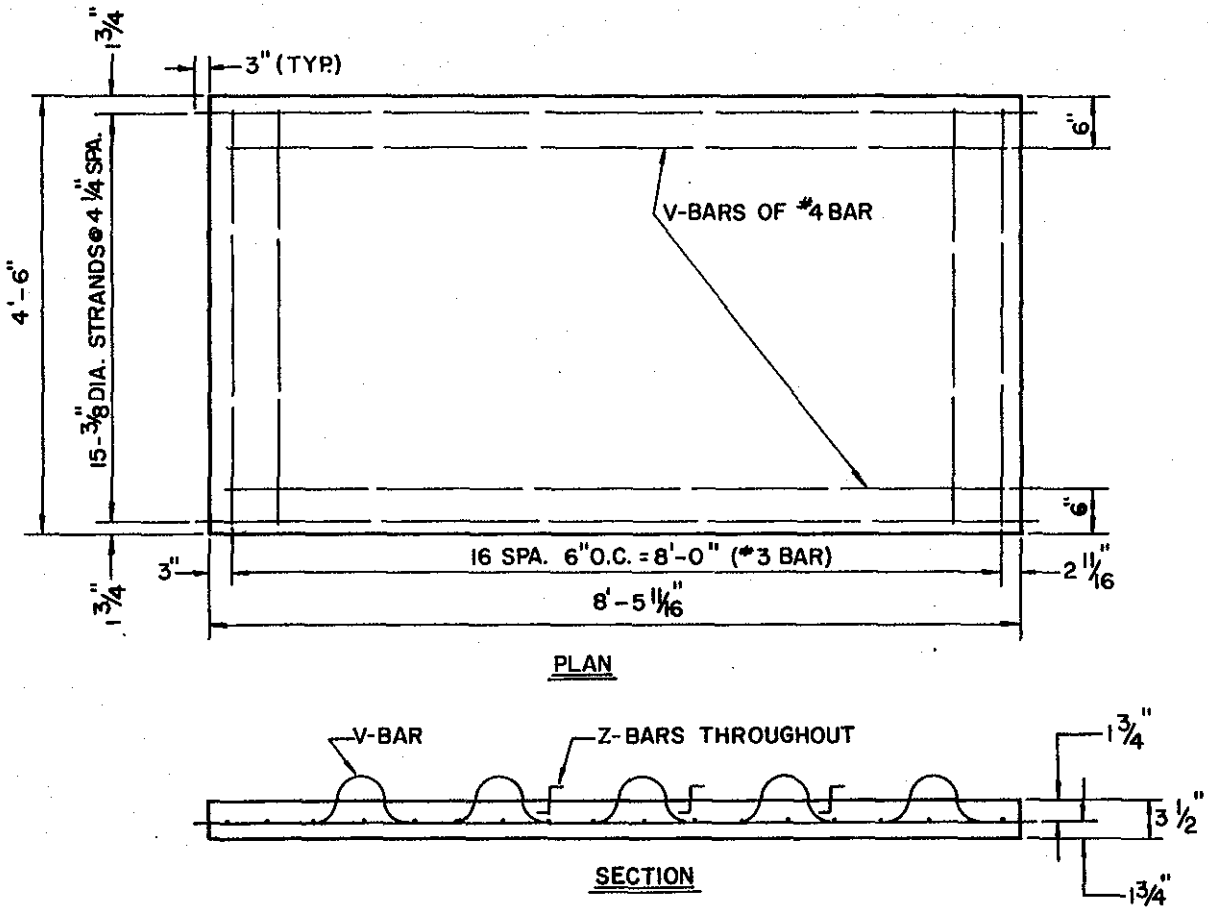

Figure 16. Detail of Panels Used in Slab Segment for Loading No. 4 (Trinity River Bridge Panel).

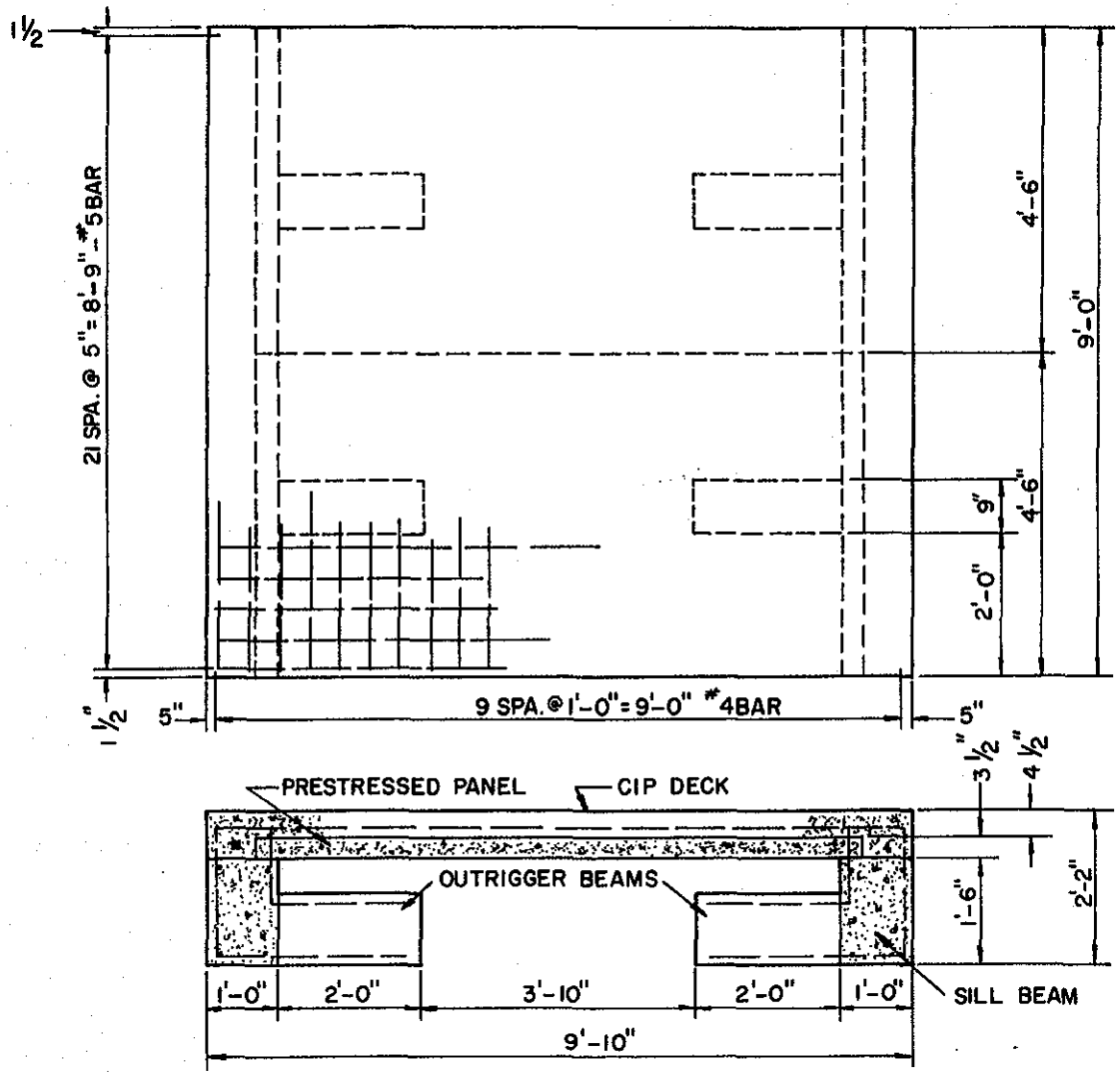

Figure 17. Dimensions and Layout of Slab Segment Model.

The positions of the electrical resistance strain gages on the full-scale structure are shown in Figure 18, and detailed dimensions of typical patterns are given in Figure 19. The gages on the full-scale model, indicated by a number in Figure 18, were mounted on the top of the slab and bottom of the prestressed panel and on the top and bottom of the beams. Gages with odd numbers were on the top, and those with even numbers were on the bottom. The slab gages were designed to provide information that would indicate bond failure between slab and panel if such developed at the gage. These gages were grouped close to the load pads where shear and bending were most severe in the slab.

Signals from these strain gages were channeled through a multi-channel switching and balancing unit to a manually operated strain indicator. The switching and balancing unit was originally capable of accommodating only one temperature compensating gage for the entire system. This caused two immediate problems. First, the single compensating gage did not provide satisfactory temperature induced strain compensation for each of the active gages at the various locations on both the upper and lower surface of the structure. Second, the compensating gage being in the circuit at all times and a given active gage being in the circuit only when that particular gage was selected caused some differential self heating to occur. This differential heating caused the indicated strain reading to drift for a significant time after any given channel was selected. These problems were overcome by the installation of an auxiliary selector

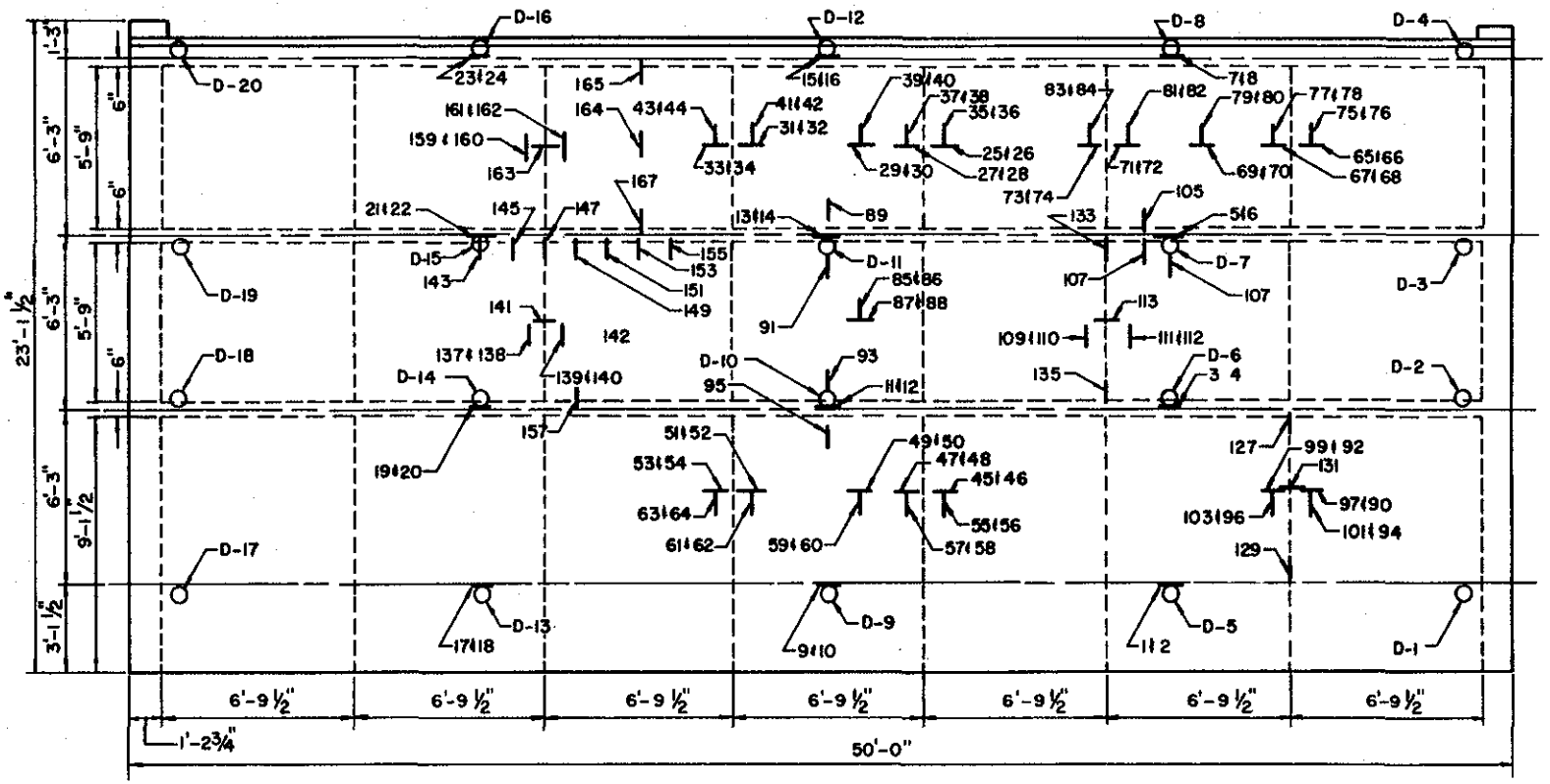

Figure 18. Layout of Electrical Resistance and Beam Deflection Gages on Full-scale Bridge.

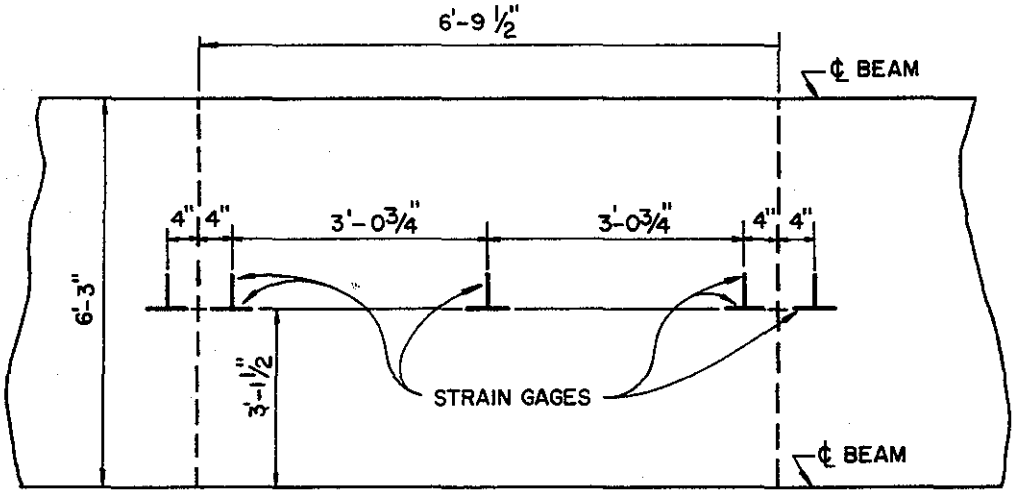

(a) Top of Slab and Bottom of Panel for Axle Load 3, at Quarter Span, (Plan View).

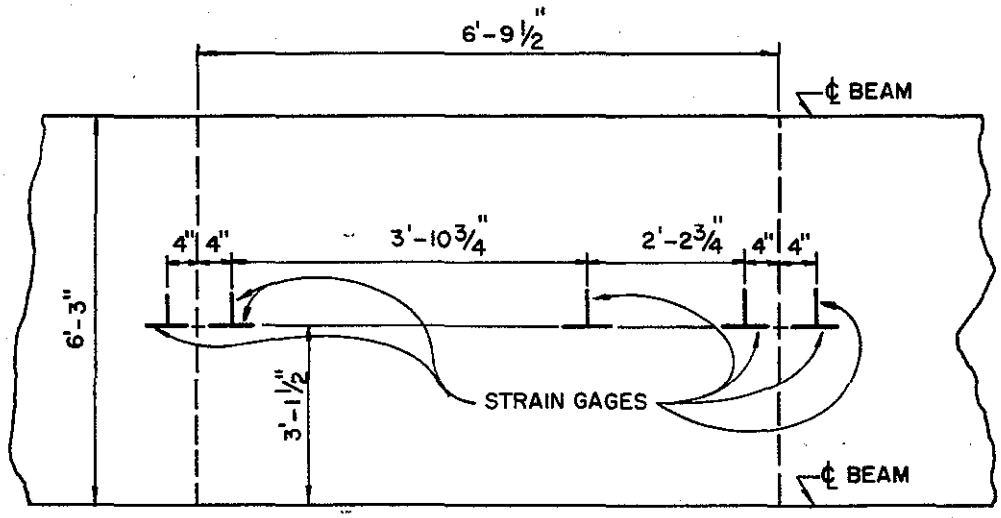

(b) Top of Slab and Bottom of Panel for Axle Loads 1 and 2, at Midspan, (Plan View).

Figure 19. Typical Electrical Resistance Strain Gage Patterns.

switch which allowed multiple compensating gages to be used in the system. Ten compensating gages were installed on a separate concrete slab placed on top of the structure, and an additional ten were used on another slab under the structure. Figures 20 and 21 are photographs of this strain gage system.

Readings under zero load were made at the beginning, and completion of each static load response test and the stability obtained in the system over the relatively short period of time required for this test was sufficient to determine the response of the structure. A zero datum for the strain gages was not maintained throughout the testing program which was conducted over a 10-month period. Such a datum was not considered necessary nor was it considered possible with the system employed. The test area was inside a large metal building, and there was an almost continuous change in temperature and humidity in that area. There were differences, too, in temperatures at various locations on the structure, especially between locations on the top and bottom surfaces. The rate of response of the full-scale structure to transient temperature conditions was different than that in the slabs on which the temperature compensating gages were mounted. For this reason, the static tests were conducted during the time of the day when temperature changes were at a minimum.

Positions for measurement of beam deflections with linear motion dial gages are marked by "d" followed by a number in Figure 18. A dial gage mounted in a holder, Figure 22, was used for making these measurements. Information from the beam deflection and beam strain

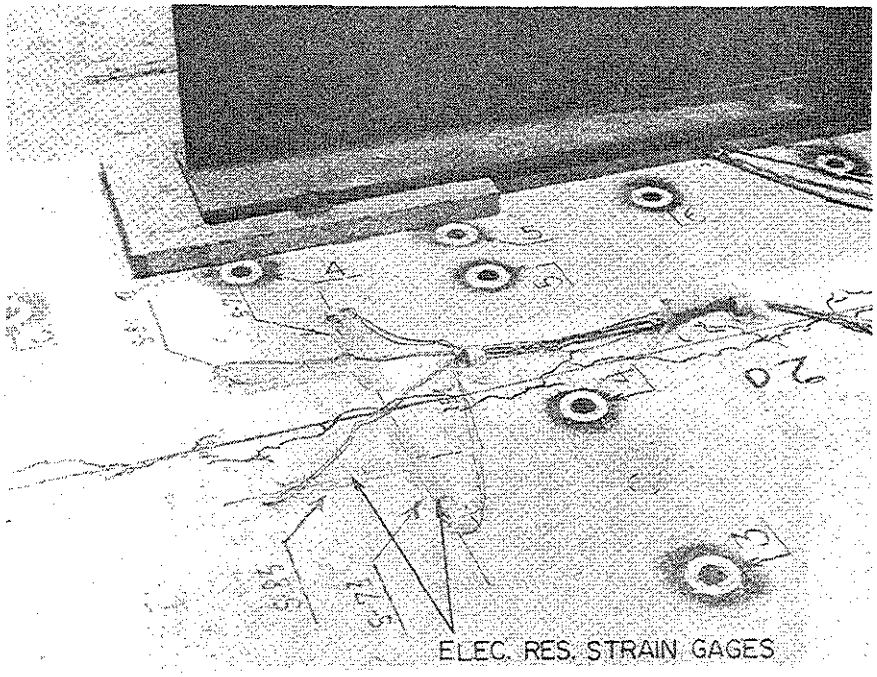

Figure 20. Photograph of Electrical Resistance Strain Gage Pattern on Top of Cast-in-place Concrete.

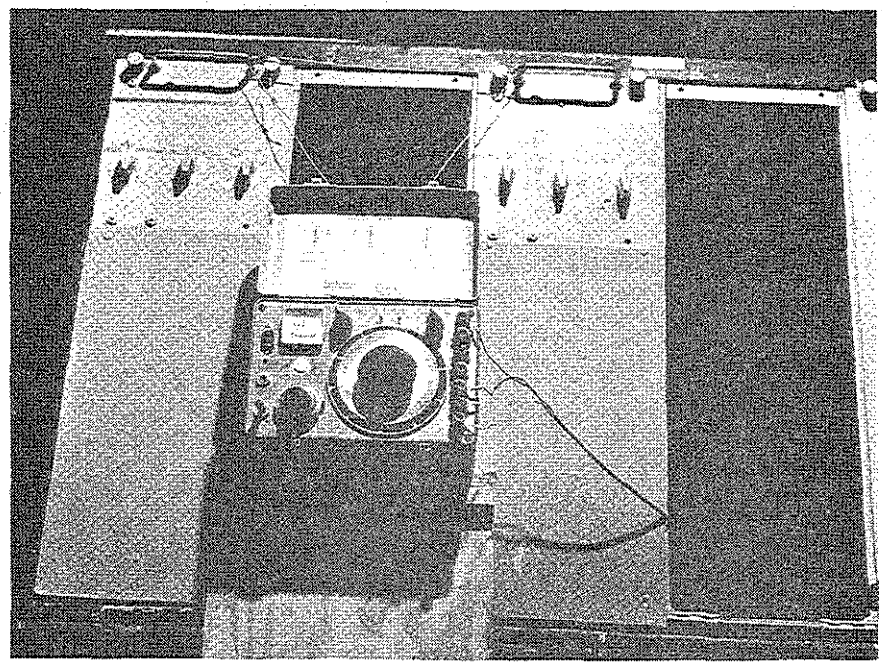

Figure 21. Photograph of Electrical Resistance Strain Gage Switching and Balancing Unit and Readout Unit.

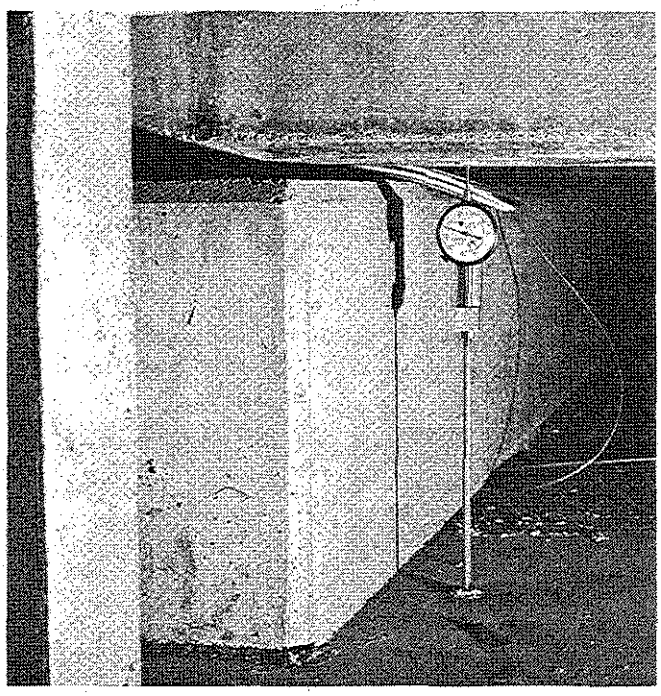

Figure 22. Gage for Measuring Beam Deflection

gages enables one to determine if the overall structure maintains its integrity throughout a loading sequence. Loss of composite action as a result of failure of the bond between the beams and the slab would result in increases in strains and deflections in the beams. These increases would be proportional to the ratio of the section modulus of the composite unit to the sum of the section moduli of the individual elements.

Linear motion dial gages were installed to detect any relative vertical motion between abutting prestressed panels and to detect transverse and longitudinal relative movement between the prestressed panels and beams. Locations of those gages are indicated in Figure 23, and photographs of typical installations are shown in Figure 24. Relative vertical movement between adjacent panels would indicate that either a vertical crack through the cast-in-place slab had developed or that bond between the panel and cast-in-place slab had failed. Either of these vertical movements would indicate a local deficiency in the structure. Any relative horizontal movement that might be detected between the beam and the slab would indicate slippage resulting from failure of the bond between those two elements.

2.4 Instrumentation of Slab Segment Model

The instrumentation for the slab segment model was planned with the same objectives as that for the full-scale bridge model and consisted of electrical resistance strain gages mounted on the top of the cast-in-place deck and on the underside of the prestressed panels

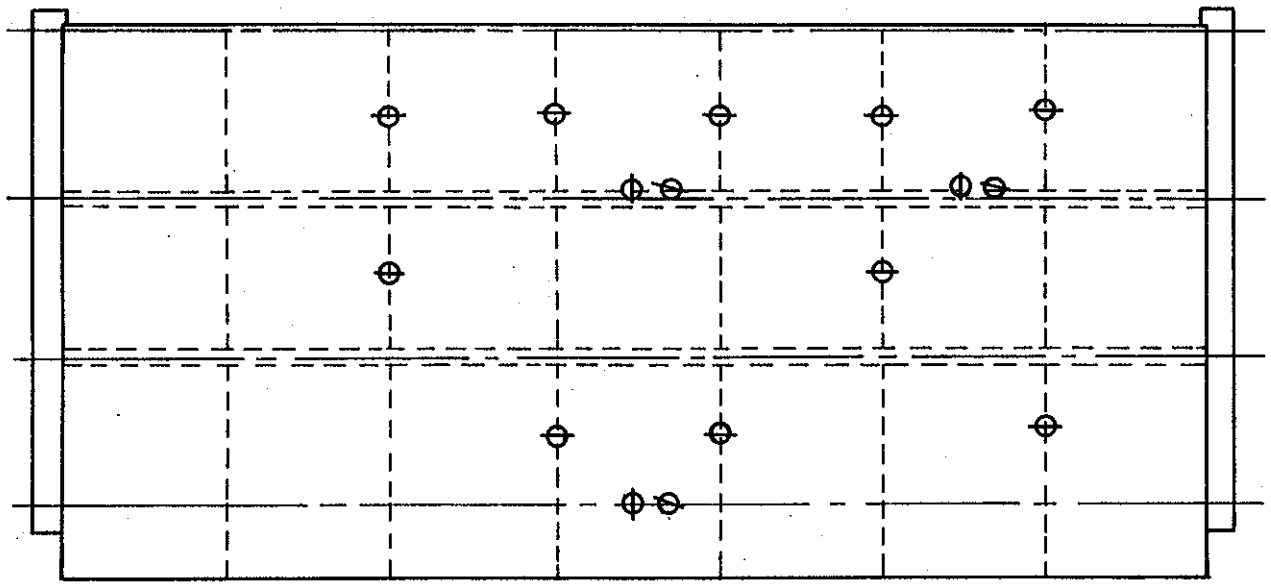

Figure 23. Positions for Panel-to-panel and Panel-to-beam Relative Displacement Dial Gages.

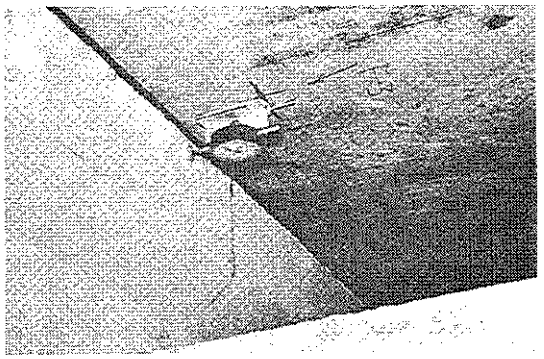

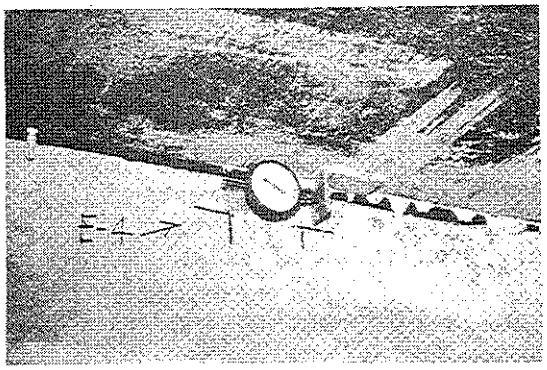

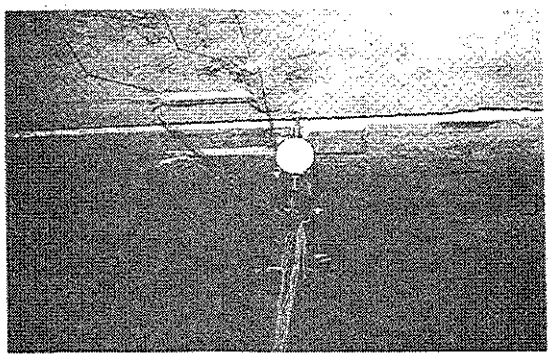

Figure 24. Linear Motion Dial Gages for Detecting Relative Displacements between Panel and Beam and between Adjoining Panels.

and a mechanical gage for measuring differentail vertical movement between panels. The gages were clustered in the vicinity of the butt joint between panels, as illustrated in Figure 25. Gages mounted on the top of the deck have odd numbers, while gages on the underside of the prestressed panels have even numbers. The signals from these gages were channeled through the same switching and balancing unit and strain indicator used for the full-scale bridge model tests. Temperature compensating circuitry was similar to that used in the bridge model.

2.5 Loading System for Full-scale Bridge Model

Two types of loading arrangements were used to simulate loads due to traffic. Simulation of axle loads was accomplished with the hydraulic ram and loading pad arrangement, illustrated in Figures 26 and 27. The two pads representing the dual wheels of a single heavy axle of a design H20 truck were 12 in. by 20 in. in plan and spaced 6 ft. on centers. A Riehle-Los hydraulic testing machine, shown in Figure 28, operated a ram for both the static and dynamic axle loadings. The cyclic loading capability of this equipment was derived from a piston and flywheel arrangement driven by an electric motor. The system resulted in a nearly simusodial loading for these particular tests (Fig. 29).

Pressure gages in the loading system were calibrated by means of a calibrated load cell placed between the ram and the loading pad. Prior to loading in each load position, both static and cyclic load calibrations were made. The load cell was removed during cyclic loading,

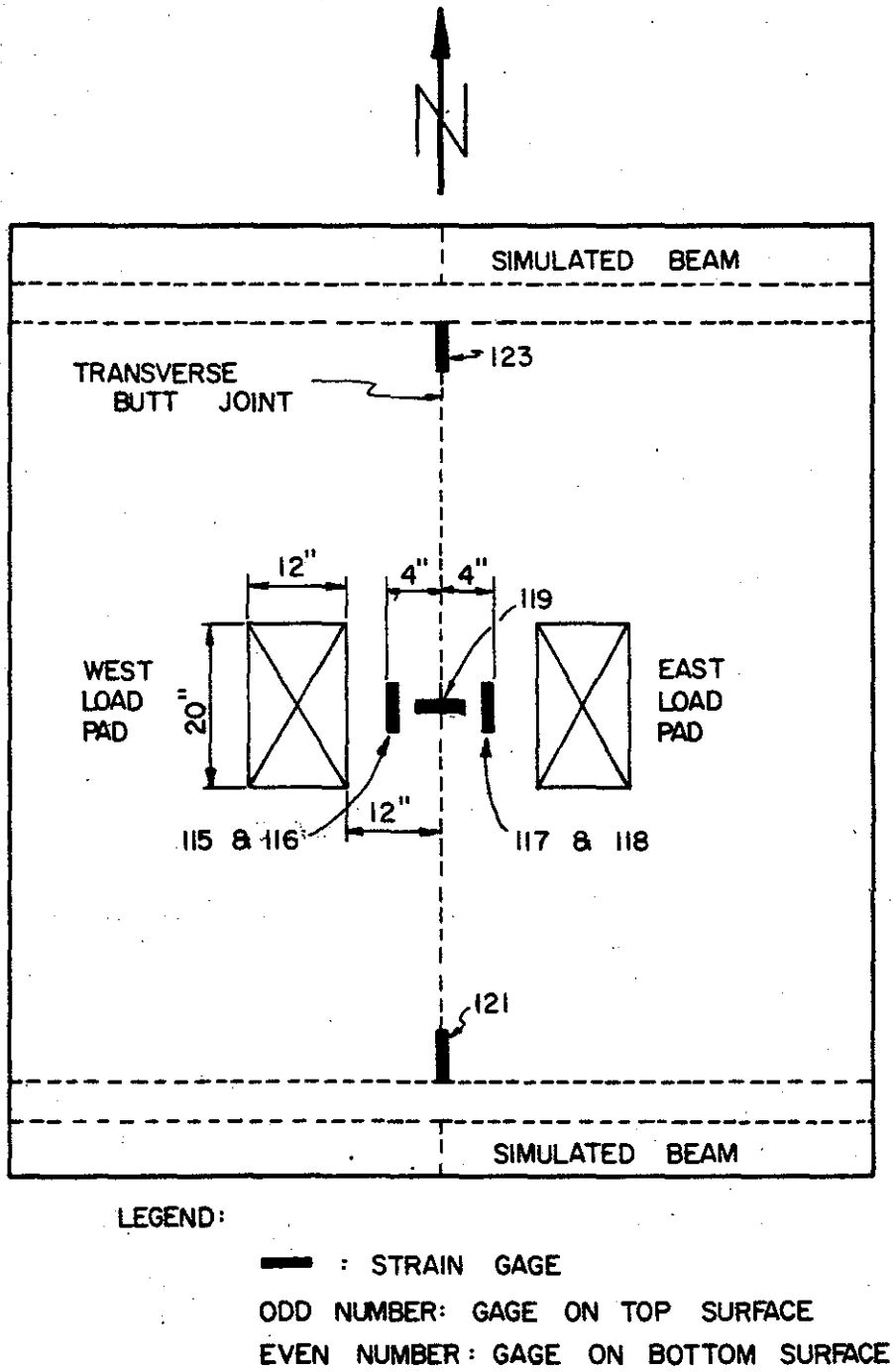

Figure 25. Positions of Strain Gages on Slab Segment Model.

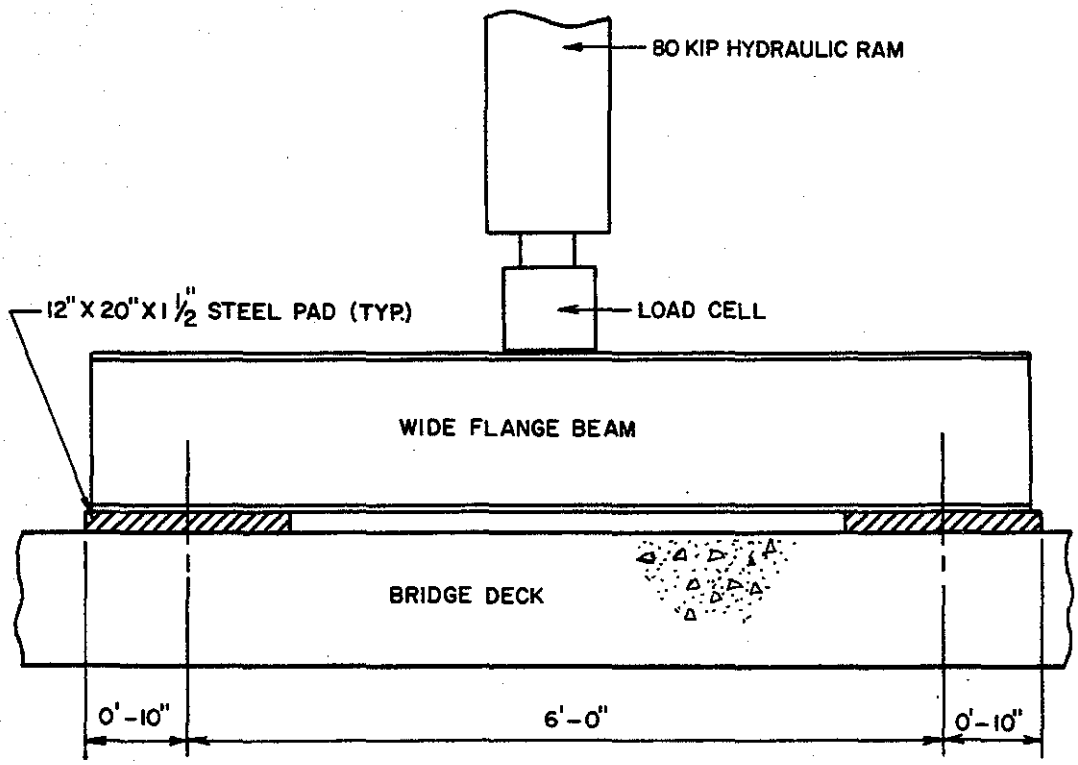

Figure 26. Hydraulic Ram and Loading Pad Arrangement for Applying Simulated Axle Loads.

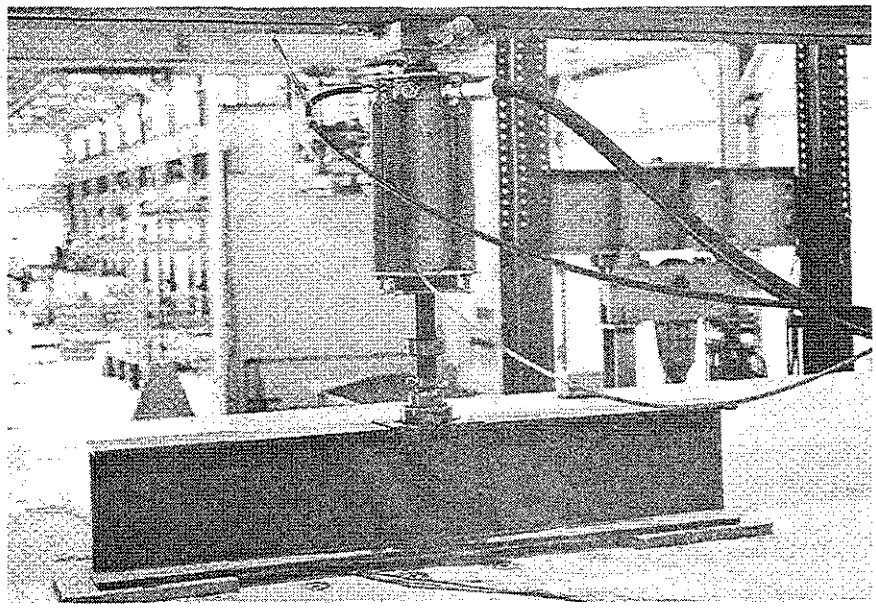

Figure 27. System for Applying Simulated Axle Loads to Full-scale Bridge.

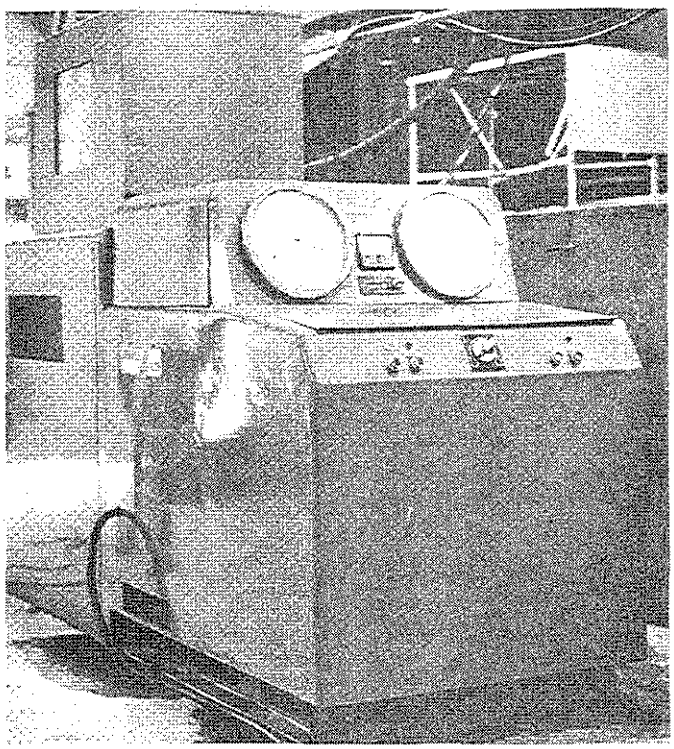

Figure 28. Riehle-Los Pulsating Unit.

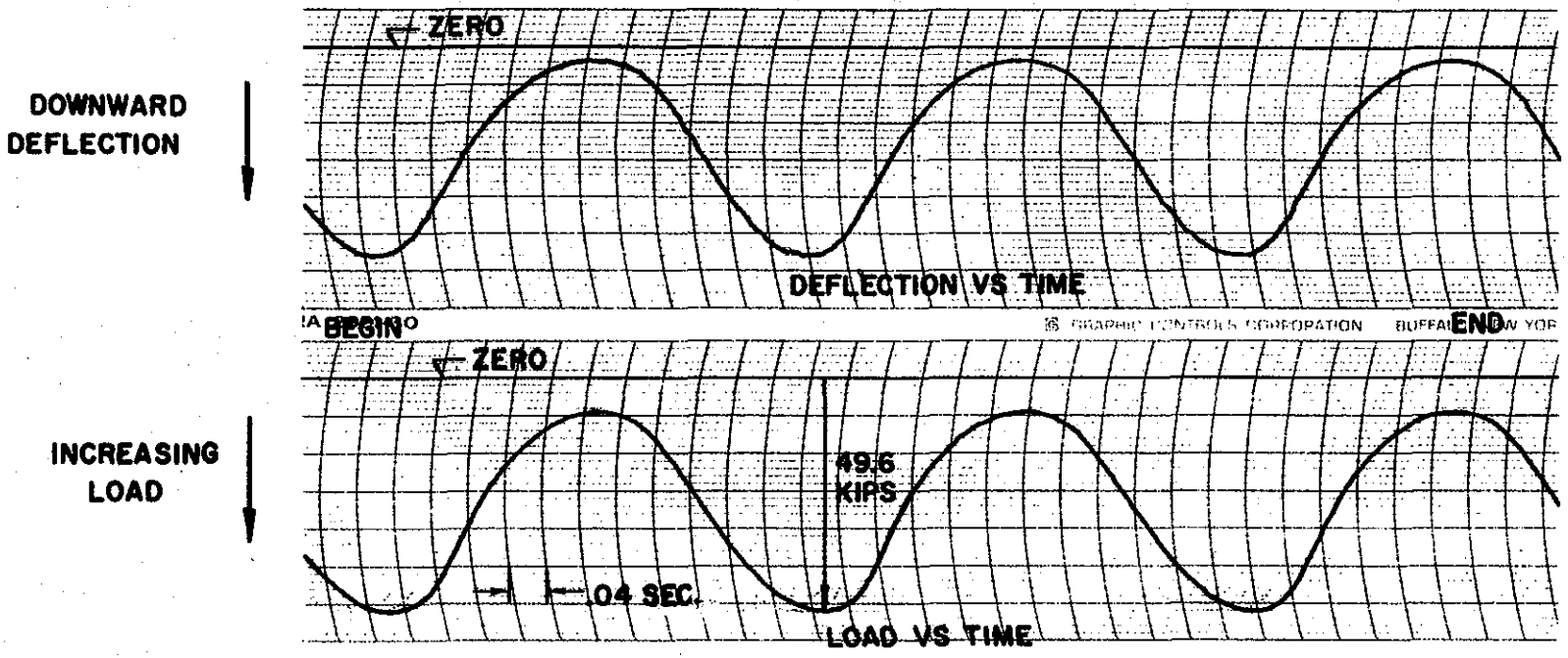

Figure 29. Strip Chart Record of Load and Reflection Recorded during Application of Load 3.

and the pressure gages were used to control the load.

Simulation of a wheel load rolling across a transverse butt joint between prestressed panels was accomplished with two hydraulic rams acting on loading pads positioned on opposite sides of and adjacent to the transverse joint (Fig. 30). The load alternated between the two rams, and one ram loaded and unloaded while the other remained inactive. The pulsator used to produce this alternating wheel loading produced a nearly trapezoidal load-time trace (Fig. 31), with approximately a 21 kip peak.

The static failure load tests were conducted with the hydraulic ram and loading pad, arranged as illustrated in Figure 32. A 400 kip hydraulic ram was used for these tests, and a simple high pressure oil pump was used to supply hydraulic pressure to the ram. A calibrated load cell was used to measure the load applied to the structure.

2.6 Loading System for Slab Segment Model

The purpose of constructing and testing the slab segment model was to evaluate the performance of the reinforcing detail at the butt joint between panels (Figs. 16 and 17) to cyclic simulated service loads and to determine its ultimate strength characteristics. Thus, an alternating load, identical to that used on the full-scale bridge (see Section 2.5), was applied on either side of the panel butt joint to simulate rolling of a wheel across the joint. The positions of the two rams used to produce this effect are shown in Figure 25. The sequence of alternating loads between east and west load pads was the

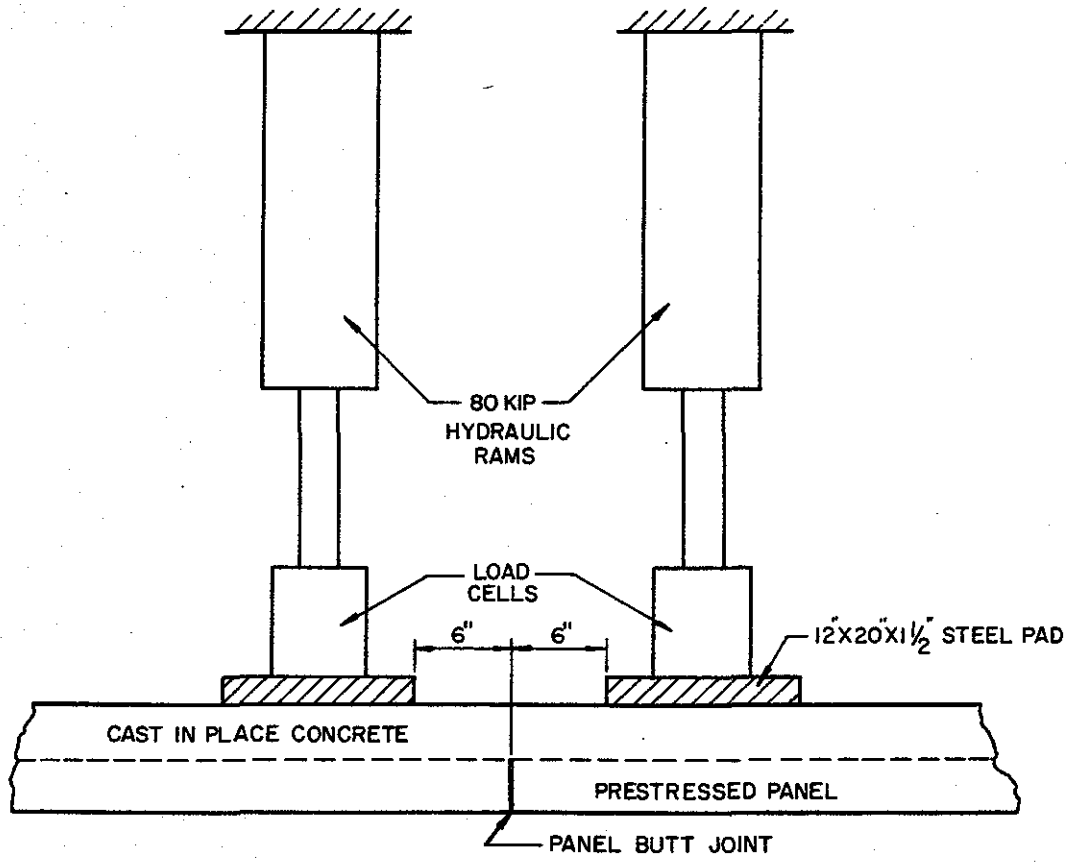

Figure 30. Arrangement of Hydraulic Rams and Loading Pads for Applying Cyclic, Alternating Simulated Wheel Loads.

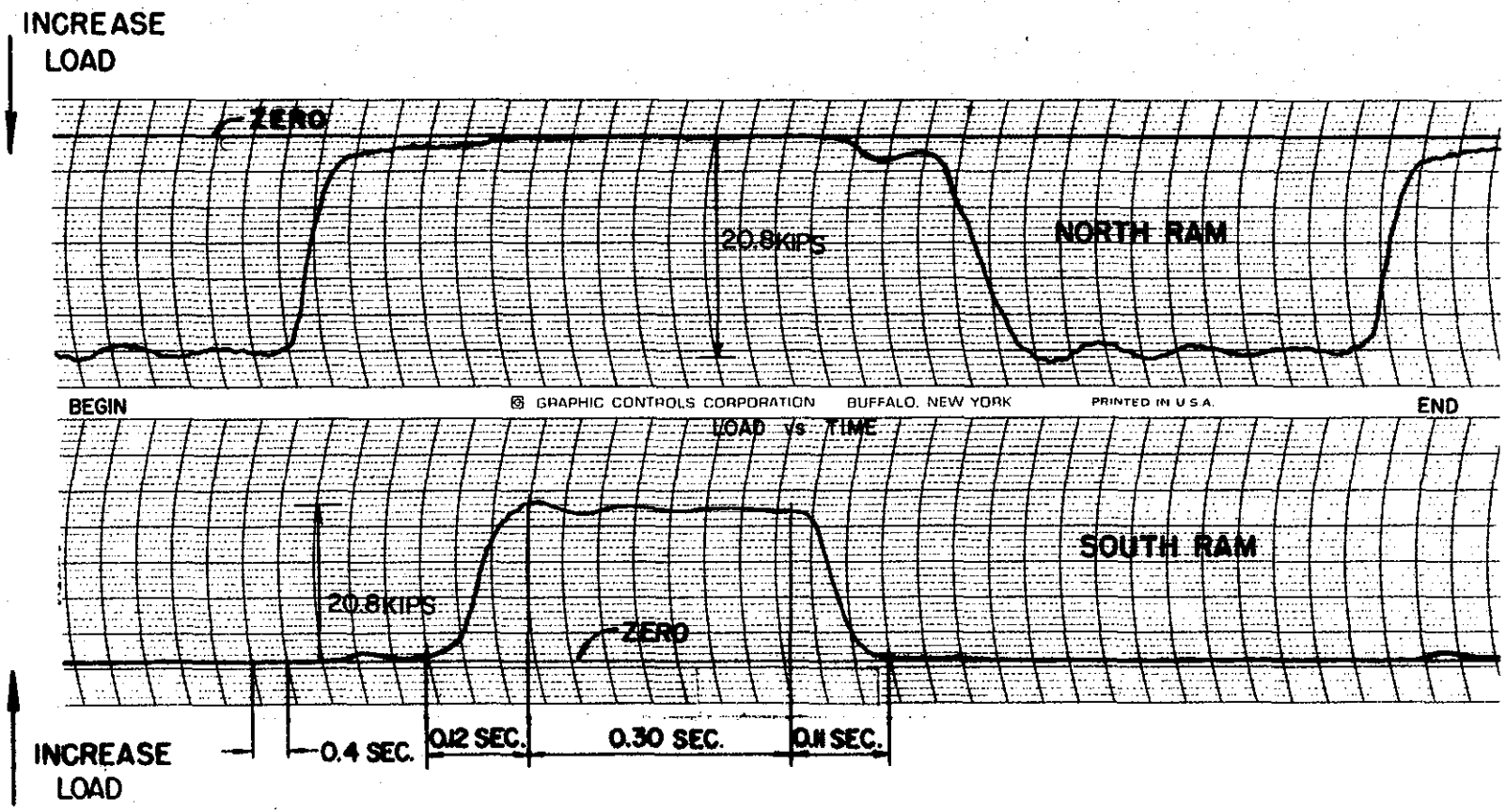

Figure 31. Strip Chart Record of Load vs. Time Recorded During Applications of Load 4.

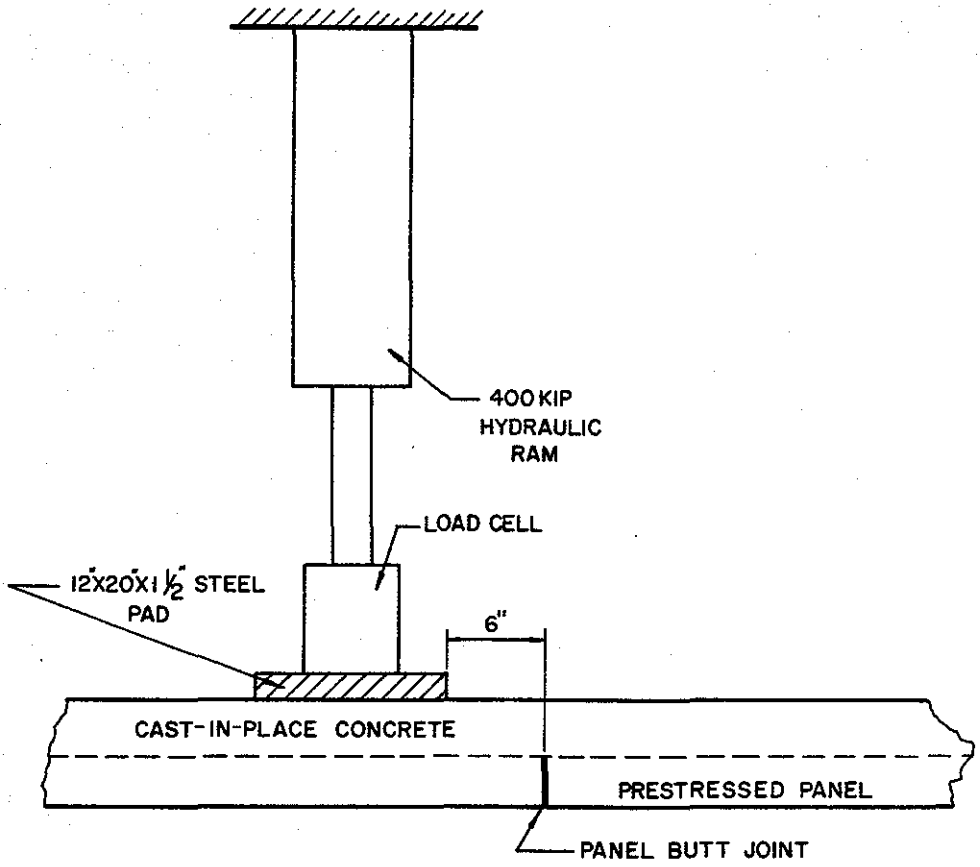

Figure 32. Hydraulic Ram and Loading Pad Arrangement for Static Failure Load Tests.

same at that shown in Figure 31 for the north and south load pads on the bridge model. The peak ampitude load on either pad was approximately 21 kips.

2.7 Program of Tests For Full-Scale Bridge and Slab Segment Models

The structures were subjected to cyclic design loads, and after completion of these, to static failure loads. In the application of the cyclic loads, the condition of the structure was determined by periodically measuring its response to static load. Gage readings under application of a static load were made before the start of cyclic loading, at predetermined intervals, and after completion of cyclic loading at each load position.

The loading plan, designed to accomplish a complete evaluation of the structures, is shown in Table 3. The positions of the loads on the full-scale bridge model are indicated in Figure 33. Loads 1 through 3, applied to the bridge model, were cyclic loads and simulated an AASHO design axle load plus impact of 41.6 kips. Load 4 was a cyclic load and alternated on either side of a panel butt joint to simulate an AASHO design wheel load plus impact of a total 20.8 kips, rolling across the joint. Loading 4A in Table 3 designates the alternating load applied to either side of the butt joint between panels in the slab segment model. Loads 5 through 8 were static failure loads and were applied to the bridge model through a loading pad that simulated a wheel. Load 8A was a single wheel, static load to failure, applied through the west load pad of the slab segment model. The simulated axle loads were designed to evaluate both the

TABLE 3

LOADS APPLIED TO MODELS

Load No.	Type of Simulated Load	Purpose
1	Cyclic axle	To determine behavior of bond between panel and cast-in-place concrete with Z-bars and dowels, but no grout.
2	Cyclic axle	To determine behavior of bond between panel and cast-in-place concrete with Z-bars, but no dowels or grout.
3	Cyclic axle	To determine behavior of bond between panel and cast-in-place concrete with no Z-bars of dowels. One wheel pad was on grouted area, and the other one was not.
4	Cyclic, alternating wheel	To determine ability of deck to support load simulating wheel crossing joint between two panels with no dowels or Z-bars.
4A	Cyclic, alternating wheel	To determine ability of deck to support load simulating wheel crossing joint between two panels with dowels, hair pins, and Z-bars. Panels identical to those in IH635 Trinity River bridge.
5	Static wheel	To determine the failure load of the structure in an area with no dowels or Z-bars.
6	Static wheel	To determine the failure load of the structure in an area with no dowels or Z-bars.
7	Static wheel	To determine the failure load of the structure in an area with Z-bars, but no dowels.
8	Static wheel	To determine the failure load of the structure in an area with Z-bars and dowels.
8A	Static wheel	To determine the failure load of the simulated slab segment panels identical to those in IH635 Trinity River bridge.

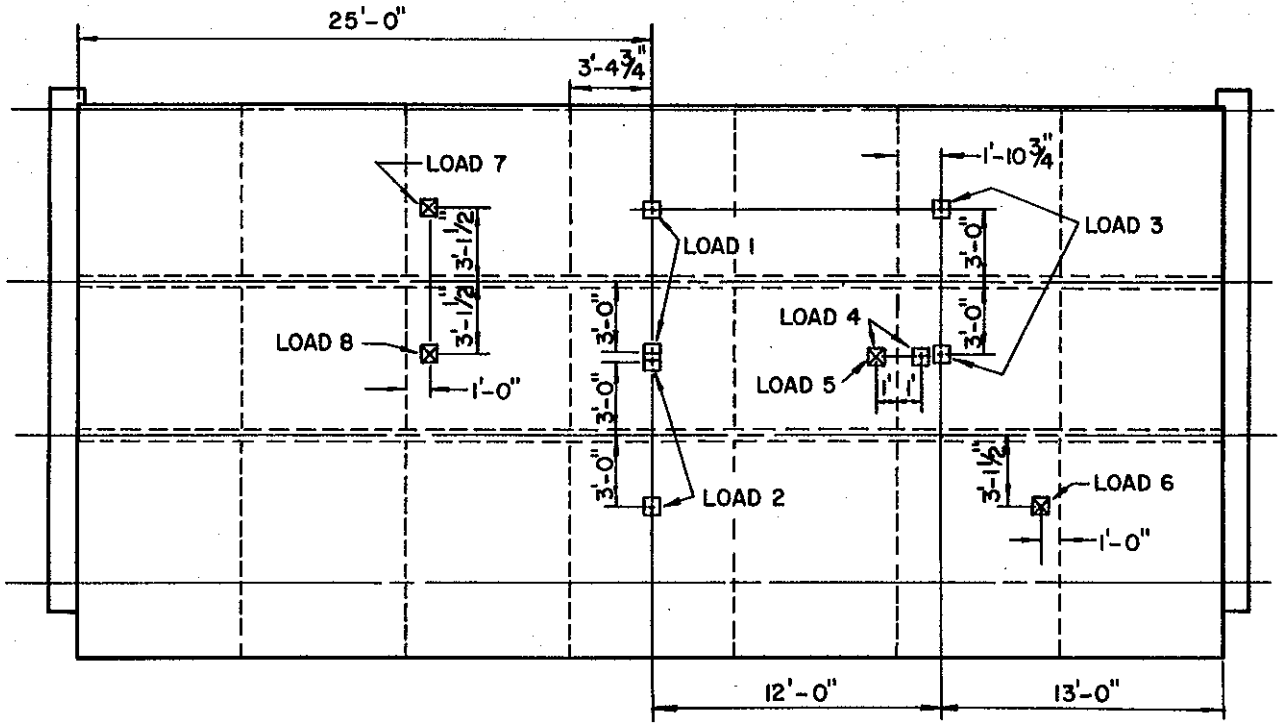

Figure 33. Plan View of Structure Illustrating Load Positions.

overall and local behavior of composite action in the structures. The wheel load was designed to evaluate the local behavior of the slab at a transverse panel butt joint. The static failure loads were designed to determine the magnitude of the failure load, the mode of failure, and to indicate the influence of dowels and Z-bars.

The detailed procedure for evaluation of the behavior of each of the two models under cyclic loading was as follows:

1. Determine the response to a static design load by reading the strains and deflections at all gage locations.
2. Subject the structure to a number of cycles of load.
3. Again determine the response to static load.
4. Visually inspect the structure each time the static load is applied to determine if any form of distress has occurred.
5. Compare the responses to static loads obtained in 1 and 3 above to determine if any distress has occurred in the structure.

For load 1 through 3, static load response tests were conducted as follows:

1. Prior to loading, make initial readings on all beam deflection gages (bridge model only) and all strain gages.
2. Subject the structure to increments of load of 16 kips beginning at zero and continuing to 48 kips axle load.
3. Read all gages at each load increment.
4. Return to zero load in one step and again read all gages.
5. Visually inspect the structure under zero load and under

the full 48 kips axle load.

This static load evaluation was conducted before cyclic loading was started, after 1/2 million cycles, after 1 1/2 million cycles, and at the end of 2 million cycles.

The design axle load, including 30 percent increase for impact, was 41.6 kips. The minimum that the cyclic loading equipment was capable of producing on the low end of the load cycle was 8 kips. Since the stress range as well as the maximum stress is considered to be an influential parameter in fatigue testing, it was decided that the cyclic load range should be the full design value of 41.6 kips and was applied at approximately 160 cycles per minute (2.67 cycles per second). The natural flexural frequency of vibration of the bridge model was calculated to be 9.2 cycles per second as compared to a measured value of 10 cycles per second. The natural frequency of the slab segment model was observed to be much higher but was not calculated.

The static load response tests for load 4 were conducted basically as indicated above except that the loads were alternately applied with each of the two rams.

The cyclic loading equipment used to apply the alternating wheel load was capable of producing a zero load on the low end of the cycle. Therefore, this cyclic load ranged from zero to 20.8 kips and was applied at approximately 50 cycles per minute.

III. THEORETICAL ANALYSES

Two theoretical investigations were made in the course of this study. The first was undertaken to examine the basis for the current AASHO specification and to determine its applicability to bridges constructed with prestressed panel subdeck and cast-in-place slab. Simplified equations for longitudinal and transverse bending moments in a bridge deck in the vicinity of concentrated forces are developed and compared with experimental values. The second theoretical development was a rigorous method of elastic analysis to predict the response of a bridge to static loads. The method incorporates all pertinent effects, with the exception of beam stiffening provided by interior diaphrams and the effect of discontinuities in the deck at butt joints between panels. This method of analysis, which is an adaptation of a technique developed by Goldberg and Leve (10) for folded plate structures, was programmed for digital computer and the results of analyses were compared with experimentally measured strains and displacements in the full-scale bridge to determine if composite action was present under static service load conditions.

3.1 Development of Slab Bending Moment Equations After Westergaard

State and federal highway bridges in the United States are designed to conform to specifications of the AASHO. These specifications, developed through the years, are meant to insure adequate bridge design practices. The concept of the design method for a beam and slab bridge is to transfer the wheel loads to the beams by a

reinforced concrete slab. The slab is designed to resist a specified distribution of bending moments. Distribution of the wheel loads in the longitudinal direction is assured by the use of longitudinal reinforcing commonly referred to as distribution steel. This design method is based on derivations from elastic plate theory and has been shown to be adequate through the performance of bridge decks in service.

The relationships specified by AASHO for computing the magnitude of slab bending moments are based on work by Westergaard. (8). Westergaard applies elastic theory to the problem of bending stresses in bridge slabs assuming the slab material to be homogeneous, isotropic, and linearly elastic. Under these assumptions, the slab behavior is expressed by the classical Lagrange equation:

$$\frac{\partial^4 w}{\partial x^4} + 2\frac{\partial^4 w}{\partial x^2 \partial y^2} + \frac{\partial^4 w}{\partial y^4} = \frac{q}{D} \qquad (1)$$

A concentrated load on the slab is represented by:

$$p = \frac{2P}{S} \sum_{1}^{n} \text{Sin} \frac{n\pi u}{S} \text{Sin} \frac{n\pi u}{S} \qquad (2)$$

Westergaard first considers a slab with a finite span length, S, in the x-direction, unbounded extensions in the y-direction, and simple supports along the edges x=0 and x = S. The slab is subjected to a concentrated load, P, at (u, 0).

The solution to this problem is:

$$w = \frac{PS^2}{2\pi^3 D} \sum_{1}^{n} \frac{1}{n^3} \left(1 + \frac{n\pi y}{S}\right) e^{-n\pi y/S} \text{Sin} \frac{n\pi u}{S} \text{Sin} \frac{n\pi x}{S} \qquad (3)$$

This leads to the following function first introduced by Nadai (2):

$$\phi = D\nabla^2 w = -\frac{P}{\pi}\sum_{1}^{n} e^{-n\pi y/S} \quad \text{Sin}\frac{n\pi u}{S}\,\text{Sin}\frac{n\pi x}{S} \tag{4}$$

The bending and twisting moments are then expressed in terms of ϕ by:

$$M_x = -\frac{1+\mu}{2}\phi + \frac{1-\mu}{2}\, y\,\frac{\partial\phi}{\partial y} \tag{5}$$

$$M_y = -\frac{1+\mu}{2}\phi - \frac{1-\mu}{2}\, y\,\frac{\partial\phi}{\partial y} \tag{6}$$

$$M_{xy} = -\frac{1-\mu}{2}\, y\,\frac{\partial\phi}{\partial y} \tag{7}$$

Westergaard further considers a finite form of Eq. 4, also developed by Nadai. With the origin of coordinates at the center of the span and the concentrated load, P, at (-v, 0), this function is:

$$\phi = D\nabla^2 w = \frac{P}{4\pi}\log_e\frac{B}{A} \tag{8}$$

$$\text{Where : } A = \text{Cosh}\frac{\pi y}{S} + \text{Cos}\frac{\pi(x - v)}{S}$$

$$B = \text{Cosh}\frac{\pi y}{S} - \text{Cos}\frac{\pi(x + v)}{S}$$

Substitution of Eq. 8 into Eqs, 5 through 7 leads to the expressions for moments as follows:

$$M_x = \frac{(1+\mu)P}{8\pi} \log_e \frac{A}{B} + \frac{(1-\mu)}{8S} \text{PySinh} \frac{\pi y}{S} \left(\frac{1}{B} - \frac{1}{A}\right)$$

$$M_y = \frac{(1+\mu)P}{8\pi} \log_e \frac{A}{B} - \frac{(1-\mu)}{8S} \text{PySinh} \frac{\pi y}{S} \left(\frac{1}{B} - \frac{1}{A}\right) \quad (9)$$

$$M_{xy} = -\frac{(1-\mu)}{8S} \text{Py} \left(\frac{1}{A} \text{Sin} \frac{\pi(x-v)}{S} + \frac{1}{B} \text{Sin} \frac{\pi(x+v)}{S}\right)$$

These expressions become undefined at the point of application of the load. In order to overcome this problem, the load is considered to be distributed over a circular area of diameter, C, which actually represents a truck wheel load more realistically than does a concentrated load. The expressions for bending moment at midspan, with the load positioned at midspan and $\mu = 0.15$, then become:

$$M_{ox} = 0.21072P \left[\log_{10} \frac{S}{h} - \log_{10} \left(0.4 \frac{c^2}{h^2} + 1 - 0.675\right) + 0.1815\right] \quad (10)$$

$$M_{oy} = M_{ox} - 0.0676P \quad (11)$$

The deck thickness for a conventional slab and beam concrete bridge is generally 6 to 8 in. Footprints of a number of dual tire truck wheels were measured in this study, and the dimensions were found to average about 12 in. by 20 in. Therefore, the deck thickness, h, was assumed to be 7 in., and the diameter, c, of the loaded area was assumed to be 16 in. in Eq. 10 which then becomes:

$$M_{ox} = 0.2107 \left[\log_{10} S + .3810\right]P \quad (12)$$

Westergaard further presents an expression which gives approximately the same results as Eq. 10 by using the "effective width" concept (9). The bending moment at midspan is considered to be that produced at midspan of a beam of some effective width and subjected to a line load across its width at midspan. The maximum bending moment in such a beam is expressed:

$$M_{ox} = \frac{PS}{4b} \tag{13}$$

The effective width is a function of the ratio of span length to slab thickness, but an approximate expression given by Westergaard is:

$$b = 0.58S + 2c \tag{14}$$

The approximate expression for maximum bending moment than becomes:

$$M_{ox} = \frac{PS}{2.32S + 8c} \tag{15}$$

In order to account for the effects of edge fixity, Westergaard considers a rectangular slab with simply supported edges at $x = \pm S/2$ and $y = \pm \ell/2$, and loaded by a single force, P, at the center. The solution for this problem is shown to be:

$$w = \frac{P\ell^2}{2\pi^3 D} \sum_{1,3,5}^{n} \frac{\text{Cos } \omega_n y}{n^3} \left[\left(\text{Tanh } \alpha_n - \frac{\alpha_n}{\text{Cosh}^2 \alpha_n} \right) \text{Cosh } \omega_n x \right.$$

$$\left. -\omega_n x \text{ Tanh } \alpha_n \text{ Sinh } \omega_n x - \text{Sinh } \omega_n x + \omega_n x \text{ Cosh } \omega_n x \right] \tag{16}$$

$$\text{Where: } \alpha_n = \frac{n\pi S}{2\ell}$$

$$\omega_n = \frac{n\pi}{\ell}$$

Rotations of the edges of the slab at x = ± S/2 are elimited by super imposing the following expression for deflection:

$$w_1 = -\frac{P\ell^2}{\pi^3 D}\sum_{1,3,5}^{n}\frac{\text{Cos } \omega_n y}{n^3}\frac{\alpha_n \text{ Tanh } \alpha_n}{\text{Sinh } 2\alpha_n + 2\alpha_n}[\alpha_n \text{ Tanh } \alpha_n \text{ Cosh } \omega_n x - \omega_n x \text{ Sinh } \omega_n x] \quad (17)$$

The following expressions for the bending moments at the center of a r ctangular slab with simply supported edges at y = + 2.5πS, fixed edges at x = ± S/2, and μ = 0.15 are given by Westergaard:

$$M'_{ox} = M_{ox} - 0.0699\ P \quad (18)$$

$$M'_{oy} = M_{ox} - 0.1063\ P \quad (19)$$

In considering the effects of additional loads acting in the proximity of the load considered above, Westergaard develops expressions for the maximum bending moments due to: (1) an additional load, P_2, placed at a distance, a, from the first load, in the positive x-direction, (2) an additional load, P_3, placed at a distance, b, in the positive y-direction, (3) and finally a fourth load, P_4, placed so as to produce a rectangular load pattern when combined with the other three loads. With one axle load on the slab, it is hown by differential calculus that, for $a \leq 0.5903S$, the maximum bending moment is obtained with loads P_1 and P_2 ($P_1 = P_2$) positioned as indicated in Figure 34.

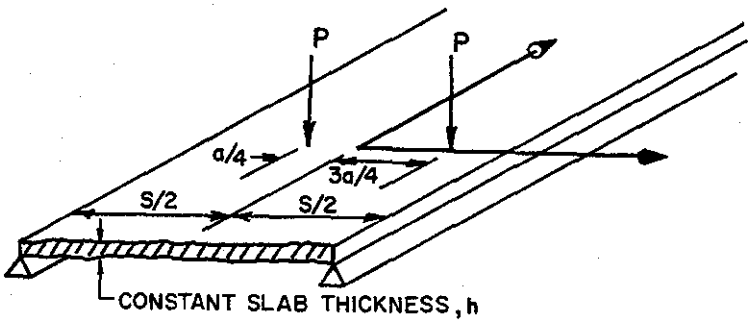

Figure 34. Position of Loads for Maximum Bending Moments.

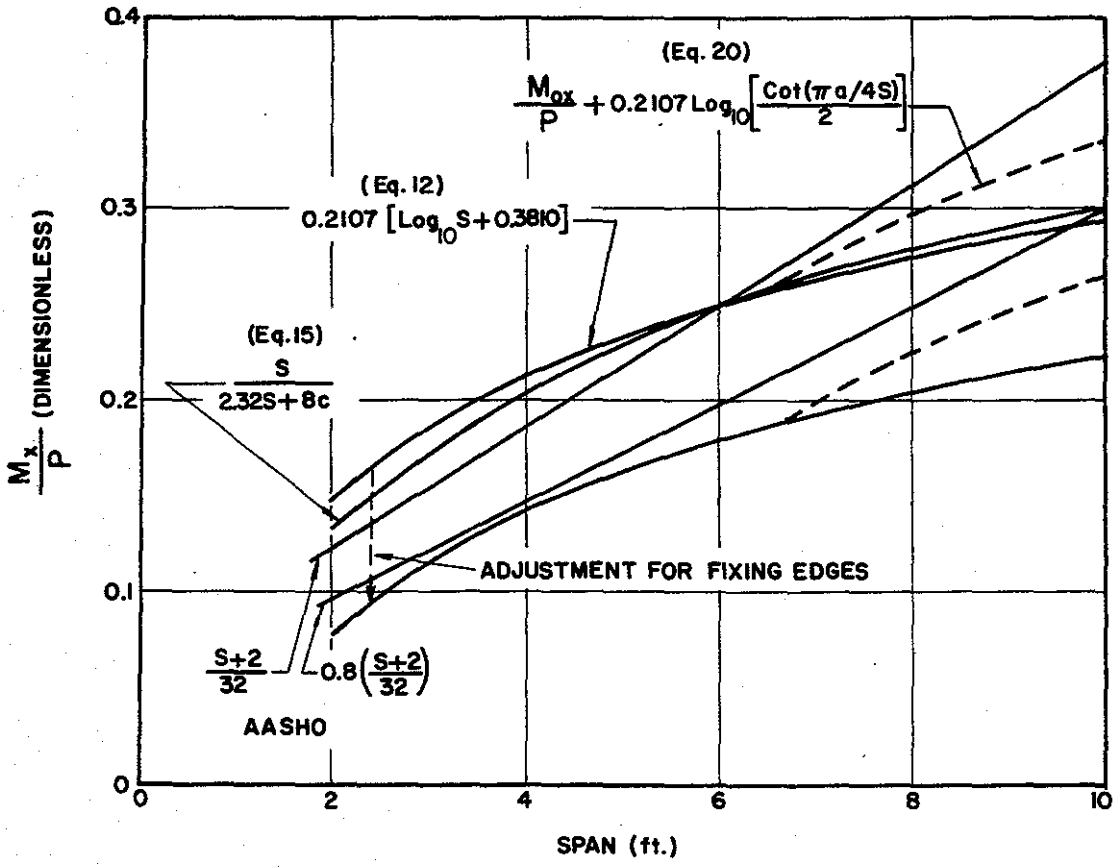

Figure 35. Comparison of Relationships between Applied Load and Maximum Slab Bending Moment in Transverse Direction.

With $\mu = 0.15$, that moment is given by:

$$M_x = M_{ox} + 0.2107\ P \log_{10} \left(\frac{\text{Cot } \frac{\pi a}{4S}}{2}\right) \qquad (20)$$

For $a > 0.5903S$ the maximum bending moment is obtained by placing only one of the loads on the slab.

The minimum transverse spacing of truck wheels is obtained when two trucks are placed side by side. The center-to-center spacing in this case, if AASHO design dimensions are used, is 4 ft. which is represented by "a" in Eq. 20. When a = 4 ft., two wheel loads on a beam and slab span is greater than (4 ÷ 0.5903) approximately 6.8 ft. When considering two axles of the same truck on the slab, two situations occur--the tandem axle arrangement, which is usually considered to be two axles spaced 4 ft. apart, and two adjacent fully loaded axles spaced a minimum of 14 ft. apart. The tandem axles are considered by AASHO to collectively carry the same load as a single axle and, therefore, produce a less critical situation than does the single axle. Adjacent full loaded axles on a truck and wheel loads from trucks in adjacent traffic lanes can possibly combine to produce the largest possible bending moments in the longer span slabs. Since it is not the purpose of this discussion to give a detailed treatment of the numerous possibilities that exist in loading, the additional situation will not be analyzed.

Figure 35 presents and compares expressions from Westergaard and the current AASHO Code for maximum bending moments in slabs. The curve

representing Eq. 12 expresses the maximum moment coefficient, M_{ox}/P, as a function of span length, for a simply supported slab subjected to a single wheel load. This equation, as discussed earlier, was developed from Eq. 10 assuming h = 7 in. and c = 16 in. Changes in the position of this curve would occur if other values of c and h were assumed. The curve parallel to and below this curve gives the maximum moment coefficient for the same conditions except that the edges of the slab are fixed against rotation. The maximum moment coefficient obtained using the effective width concept is given by the curve for Eq. 15. This curve compares reasonably well with the more complicated one for Eq. 12.

As the span of the slab increases, a point is reached where the maximum bending moment is created by placing two wheel loads on the span instead of one. For spans where it is geometrically possible to place two trucks side, this point is reached at a span length of about 6.8 ft. Eq. 20 is applicable to spans between 6.8 ft. and 10 ft. and is also included in Figure 35. The two linear relationships expressed by (S + 2)/32 and by 0.8 of that amount are the current AASHO provisions for maximum positive and negative transverse bending moments. The expression containing the factor 0.8 is to be applied in the case of slabs continous over three or more supports.

3.2 Folded Plate Analysis for Composite Slab and Beam Bridge

The typical simple span, composite slab and beam bridge shown in Figure 36 is analyzed by breaking the structure into two types of

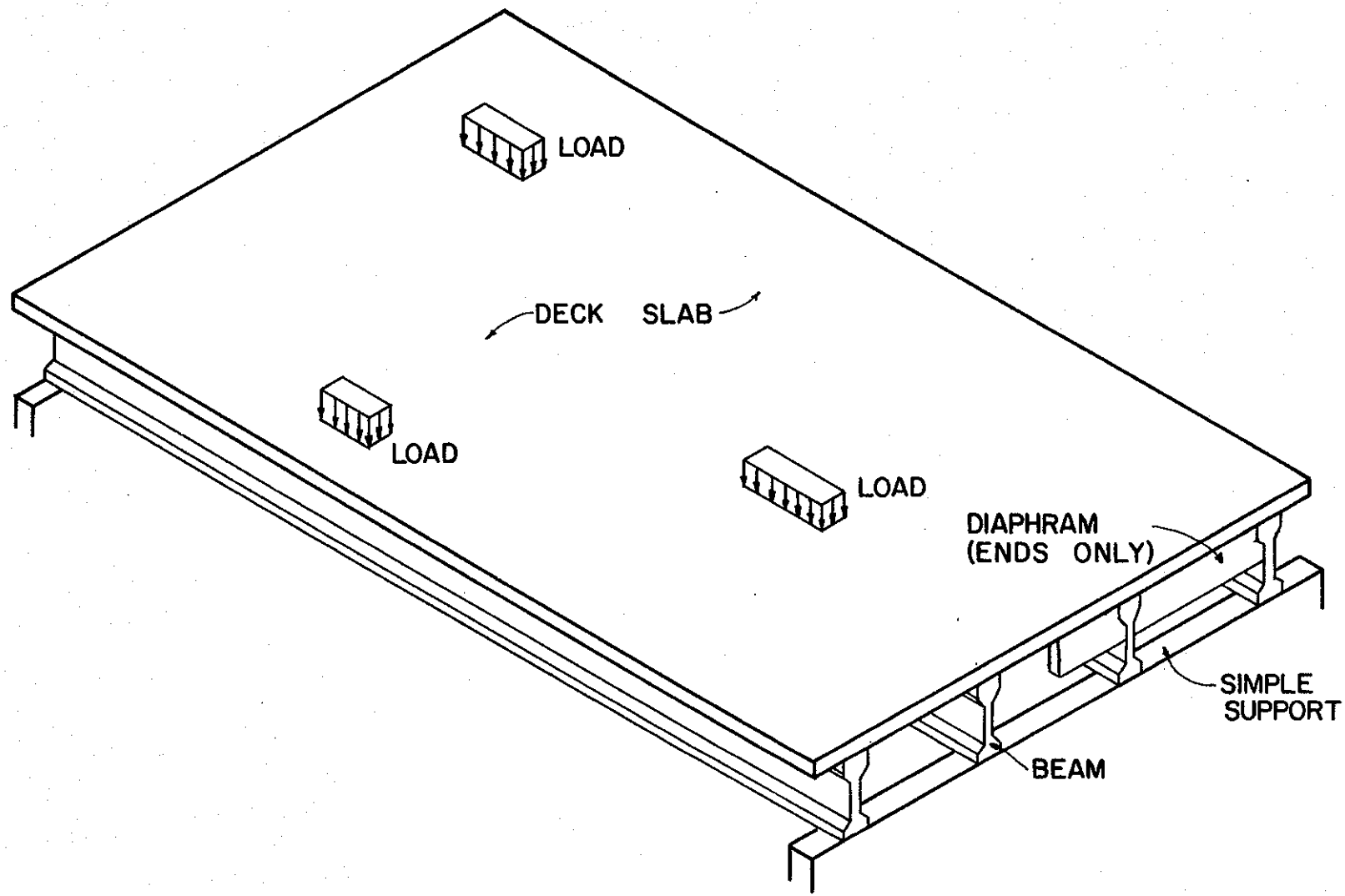

Figure 36. Typical Composite Slab and Beam Bridge.

elements; plates and beams. A plate element consists of the portion of deck slab contained between two lines of beams as shown in Figure 37. The width of the plate element is the center-to-center lateral spacing of the beams, its length is the span of the bridge and its thickness is equal to the combined thicknesses of the prestressed panel and cast-in-place deck. It is supported by, and rigidly attached to, beams along its longitudinal edges and is supported by diaphrams with negligible torsional stiffness at each end. No intermediate diaphrams are present in the bridge. The plate is assumed to be homogeneous and linearly elastic. A beam element consists of a single beam whose length is the span of the bridge. Its ends are restrained against twisting by the end diaphrams. A beam element is assumed to be homogeneous and linearly elastic.

The predominant feature of this method of analysis is the use of Fourier series expansions to represent the loads applied to the bridge and to represent the force-displacement relationships for each plate and beam element. The bridge is analyzed for each term in the load series expansion, and the results from each term are superimposed to obtain the total response of the bridge to loads. As an example of a Fourier series representation of a load on a plate, consider the line load of magnitude Q over a length α shown in Figure 38. This load may be represented by the series

$$a(x) = \sum_{m=1}^{M} q_m \sin\frac{m\pi x}{a} \qquad (21)$$

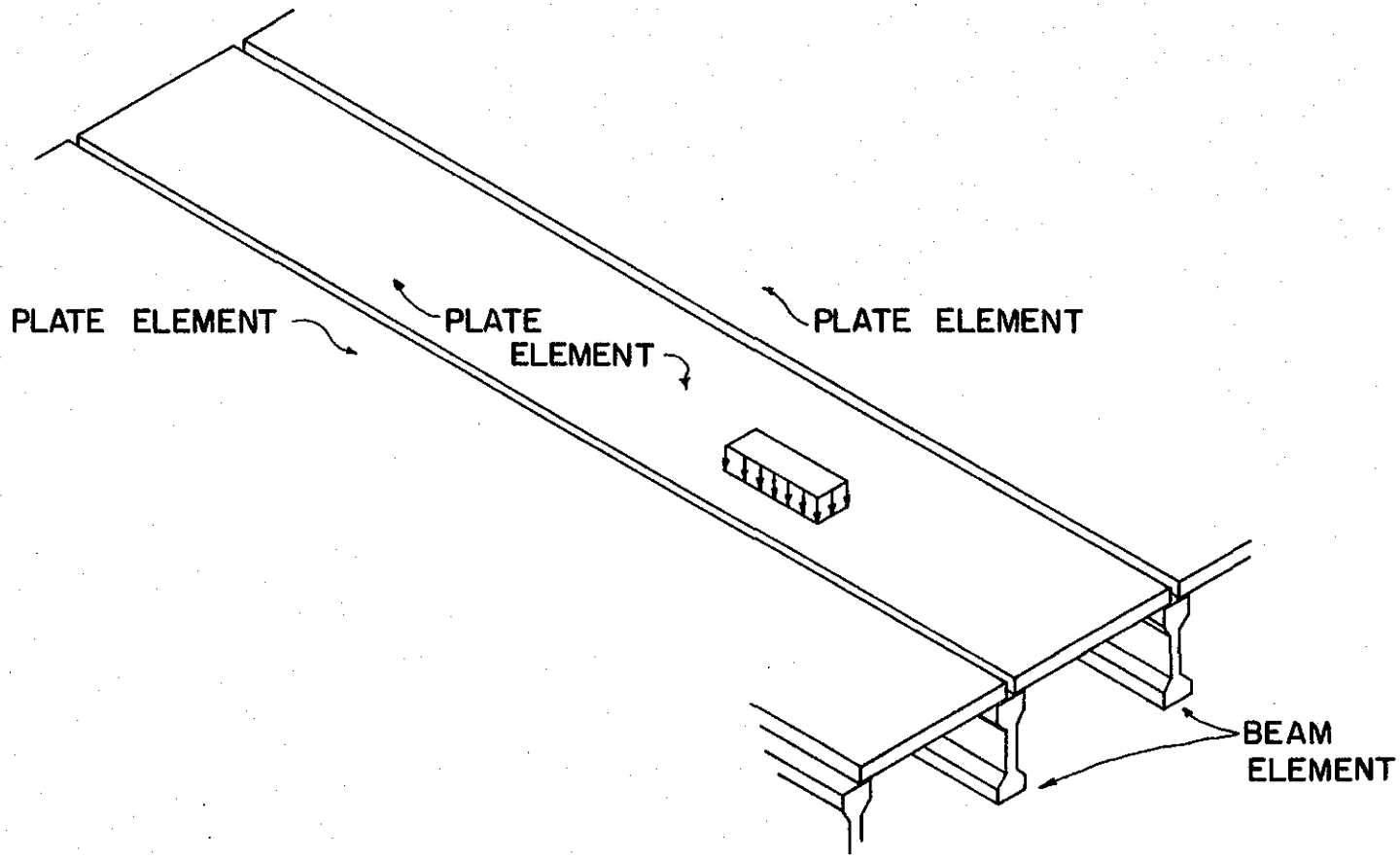

Figure 37. Beam and Plate Elements for Analysis.

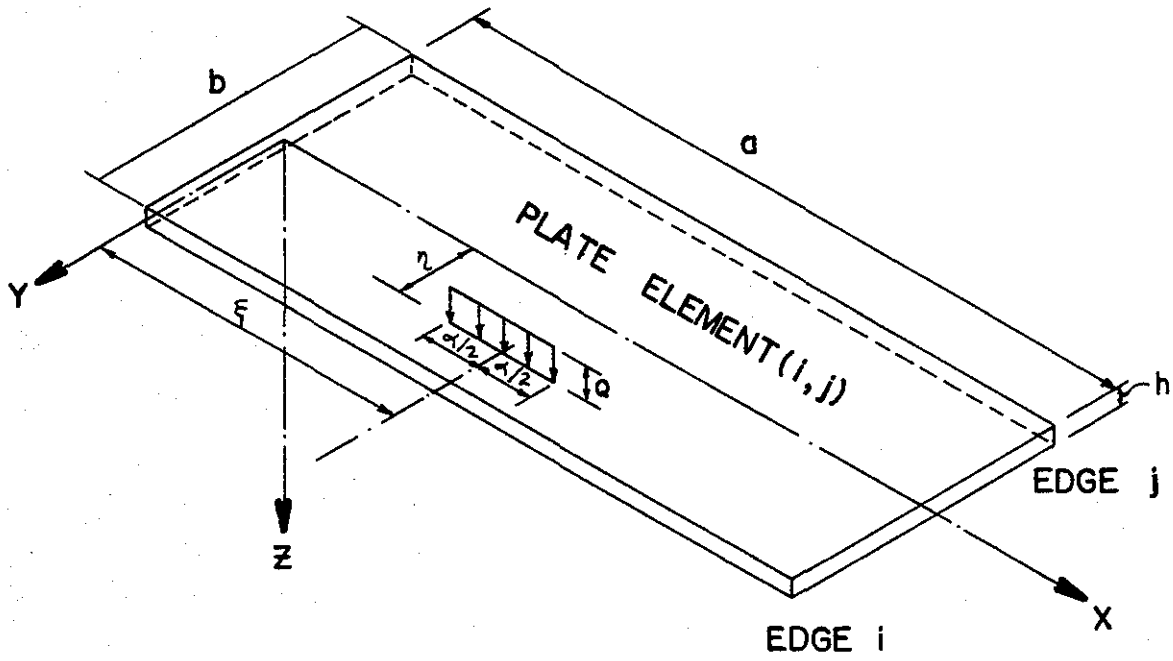

Figure 38. Line Load on a Slab.

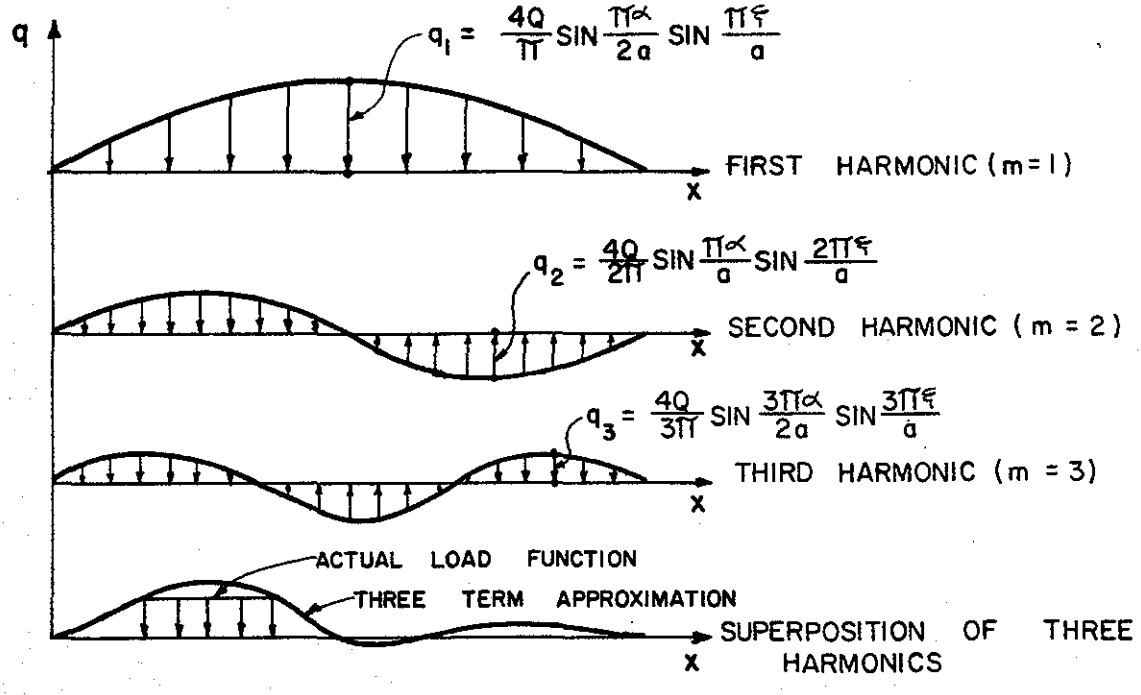

Figure 39. Fourier Series Representation of Line Load.

where the amplitude q_m of the m^{th} harmonic is given by

$$q_m = \frac{4Q}{\pi m} \sin \frac{m\pi\alpha}{2a} \sin \frac{m\pi\xi}{a} \qquad (22)$$

The contribution of the first three terms (harmonics) of this series to the representation of the actual load are shown in Figure 37, together with their superimposed result. By using a sufficient number of terms (the index M in Eq. 21), it is possible to obtain a representation to any desired accuracy. Relationships between edge-forces and edge-displacements can be derived for a plate element using series expansions similar to those used for loads. These relationships reduce the analysis of a plate to the consideration of forces and displacements along each of its longitudinal edges. The series expansion for each component of edge-force or edge-displacement will contain an amplitude (analogous to q_m in Eq. 21) multiplied by a sine or cosine term. Similarly, relationships between forces applied to a beam element and the resulting displacements that occur in the beam at points where it is bonded to the plates it supports can be written in series form. Equations for the equilibrium of forces at the juncture of plates and beam can then be stated in terms of edge displacement series. Upon canceling common sine or cosine terms from these series, a set of simultaneous linear equations in the unknown displacement amplitudes is obtained. The solution of the system of equations provides values for edge displacement amplitudes which can be used to compute moments, stresses, strains, etc. at any point in a beam or plate element.

3.2.1 Edge-force/edge-displacement Relationships for a Plate Element

Each longitudinal edge of a plate element undergoes four types of displacements when the bridge is subjected to loads; i) a downward movement, ii) a rotation about the longitudinal axis of the plate, iii) a lateral translation, and iv) a longitudinal translation. For a plate element (i, j) with longitudinal edges numbered i and j, the displacements for edge i are denoted by i) $W_{ijm}\sin\frac{m\pi x}{a}$, ii) $\phi_{ijm}\sin\frac{m\pi x}{a}$, iii) $V_{ijm}\sin\frac{m\pi x}{a}$, and iv) $U_{ijm}\cos\frac{m\pi x}{a}$, where the first term in each expression is the amplitude of the sine or cosine series, and the subscripts denote the $i^{\underline{th}}$ edge of plated (i, j) for the $m^{\underline{th}}$ harmonic. Figures 40 through 43 illustrate these types of displacements for edge i. Similar displacements along edge j of this plate are denoted by $W_{jim}\sin\frac{m\pi x}{a}$, $\phi_{jim}\sin\frac{m\pi x}{a}$, $V_{jim}\sin\frac{m\pi x}{a}$ and $U_{jim}\cos\frac{m\pi x}{a}$. These edge displacements give rise to forces along each longitudinal edge of the plate, and for edge i are denoted by $R_{ijm}\sin\frac{m\pi x}{a}$, $M_{ijm}\sin\frac{m\pi x}{a}$, $N_{ijm}\sin\frac{m\pi x}{a}$ and $S_{ijm}\cos\frac{m\pi x}{a}$, as shown in Figures 44 and 45. The resulting forces along edge j are denoted in a similar manner, with the order of subscripts i and j reversed.

If plate (i, j) is subjected to a lateral load, which can be approximated by the block loading shown in Figure 46, and its longitudinal edges are fixed against displacement, edge forces $R_{fijm}\sin\frac{m\pi x}{a}$, $M_{fijm}\sin\frac{m\pi x}{a}$, $R_{fijm}\sin\frac{m\pi x}{a}$ and $M_{fijm}\sin\frac{m\pi x}{a}$ result. The expressions for these fixed edge forces, in terms of the load parameters P, α, β,η,ξ, and plate dimensions a, b, h are given in Appendix A. The final forces on each edge of plate element (i, j) will be the sum of the fixed-edge

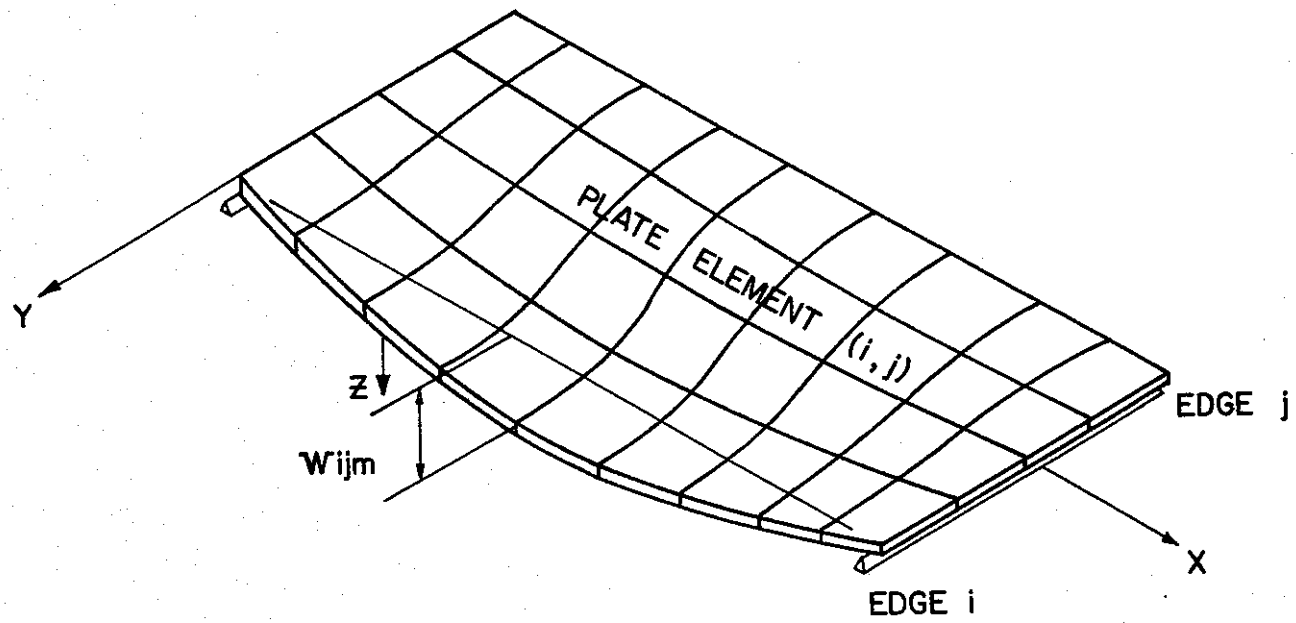

Figure 40. Downward Displacement of Edge i.

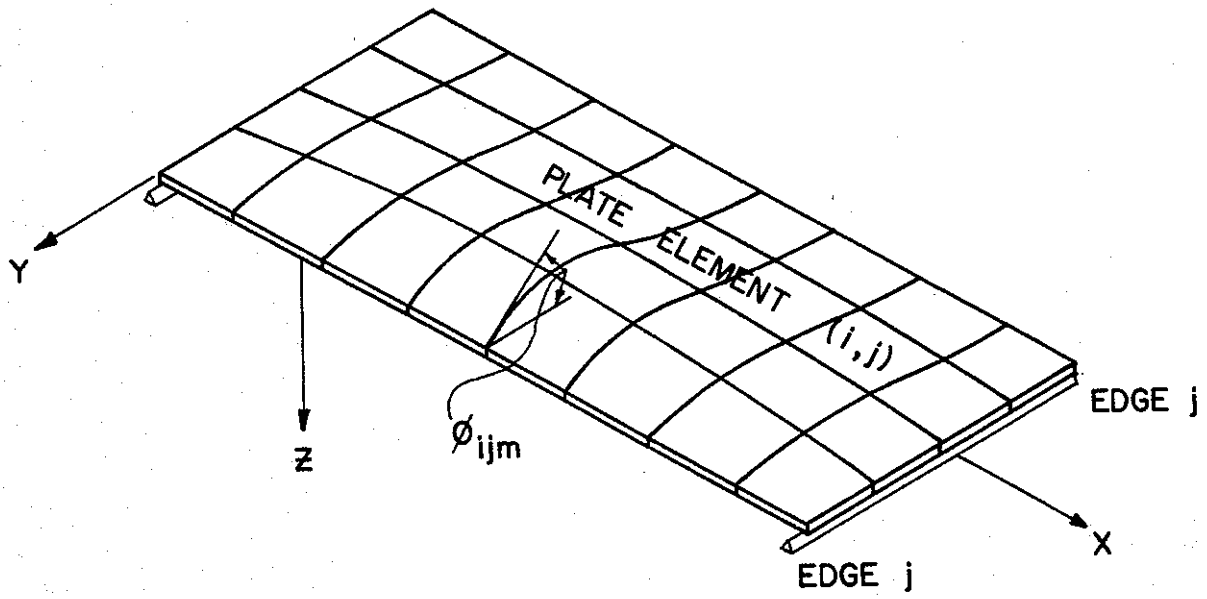

Figure 41. Rotation of Edge i.

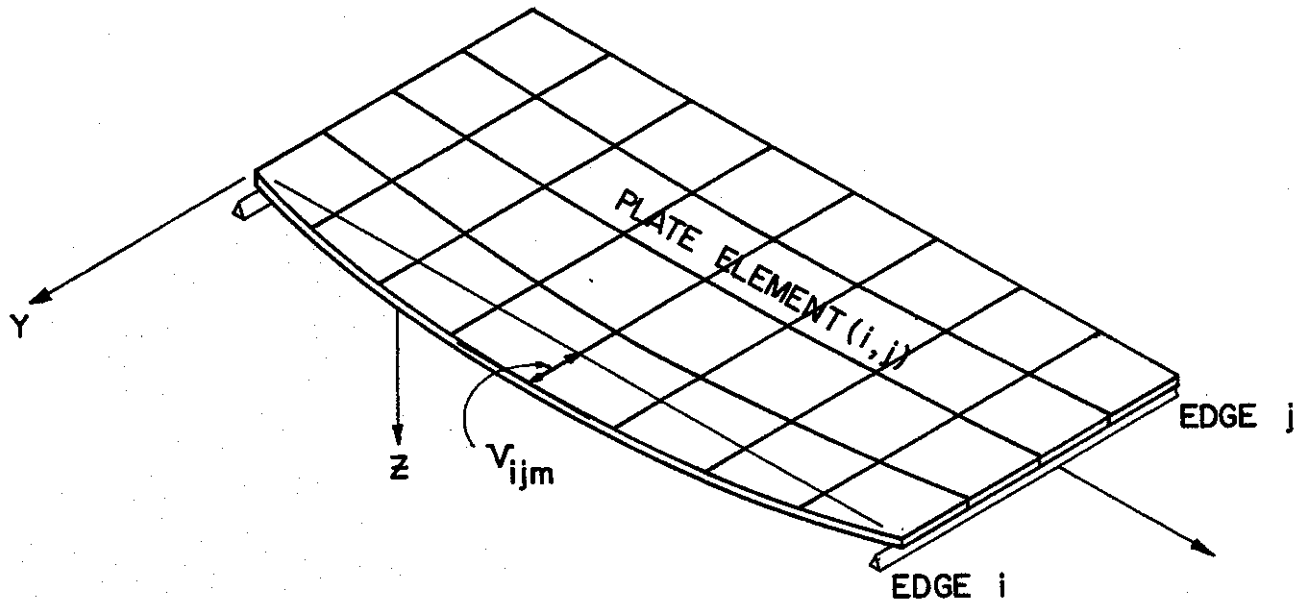

Figure 42. Lateral Translation of Edge i.

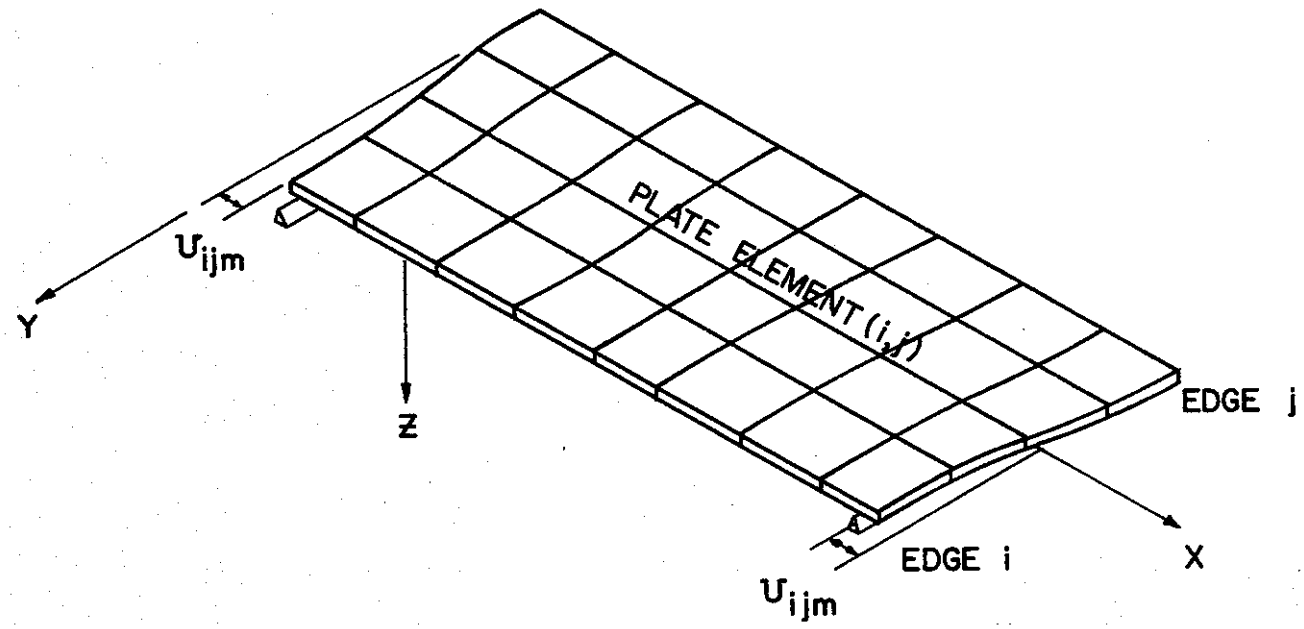

Figure 43. Longitudinal Translation of Edge i.

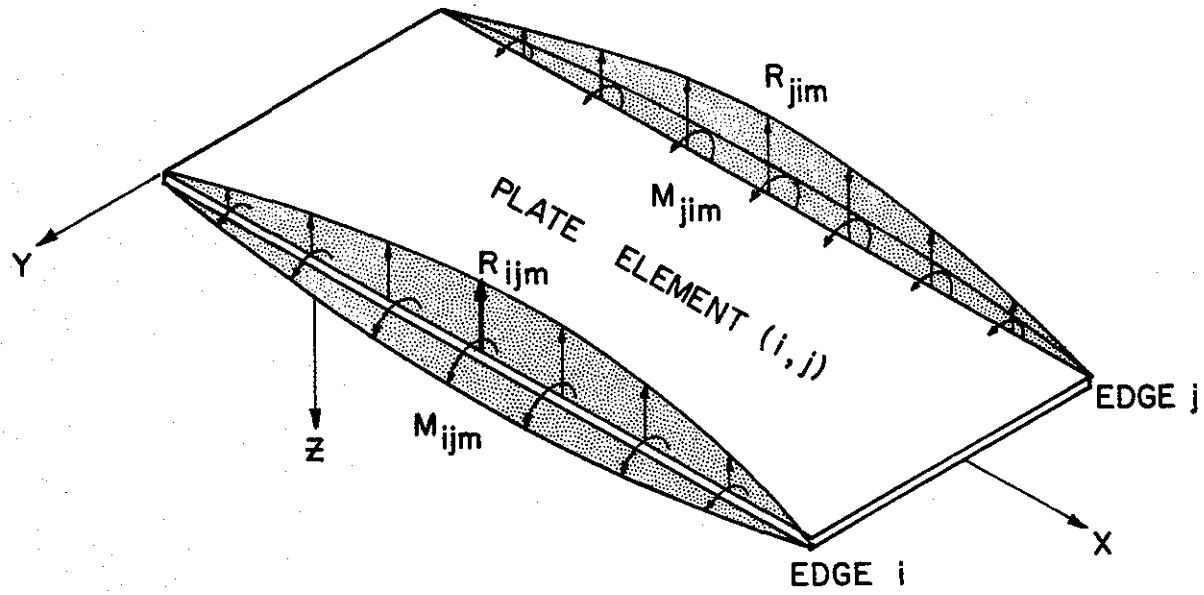

Figure 44. Edge Forces Resulting from Downward Displacement and Rotation of Edges i and j.

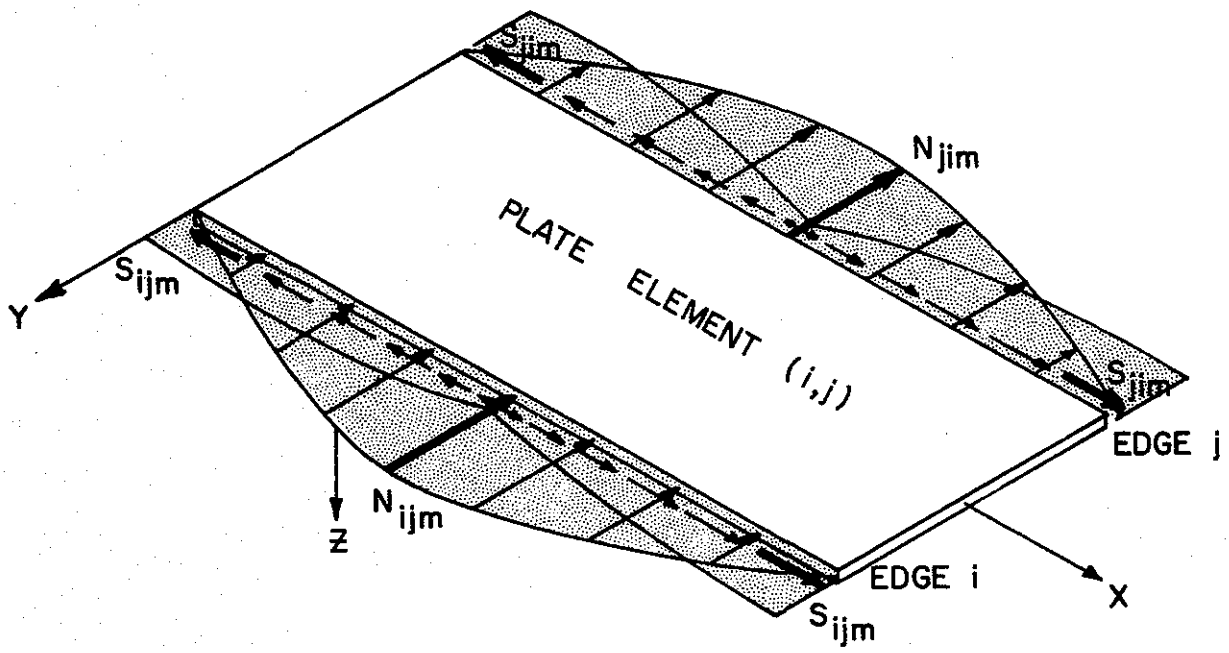

Figure 45. Edge Forces Resulting from Lateral and Longitudinal Translation of Edges i and j.

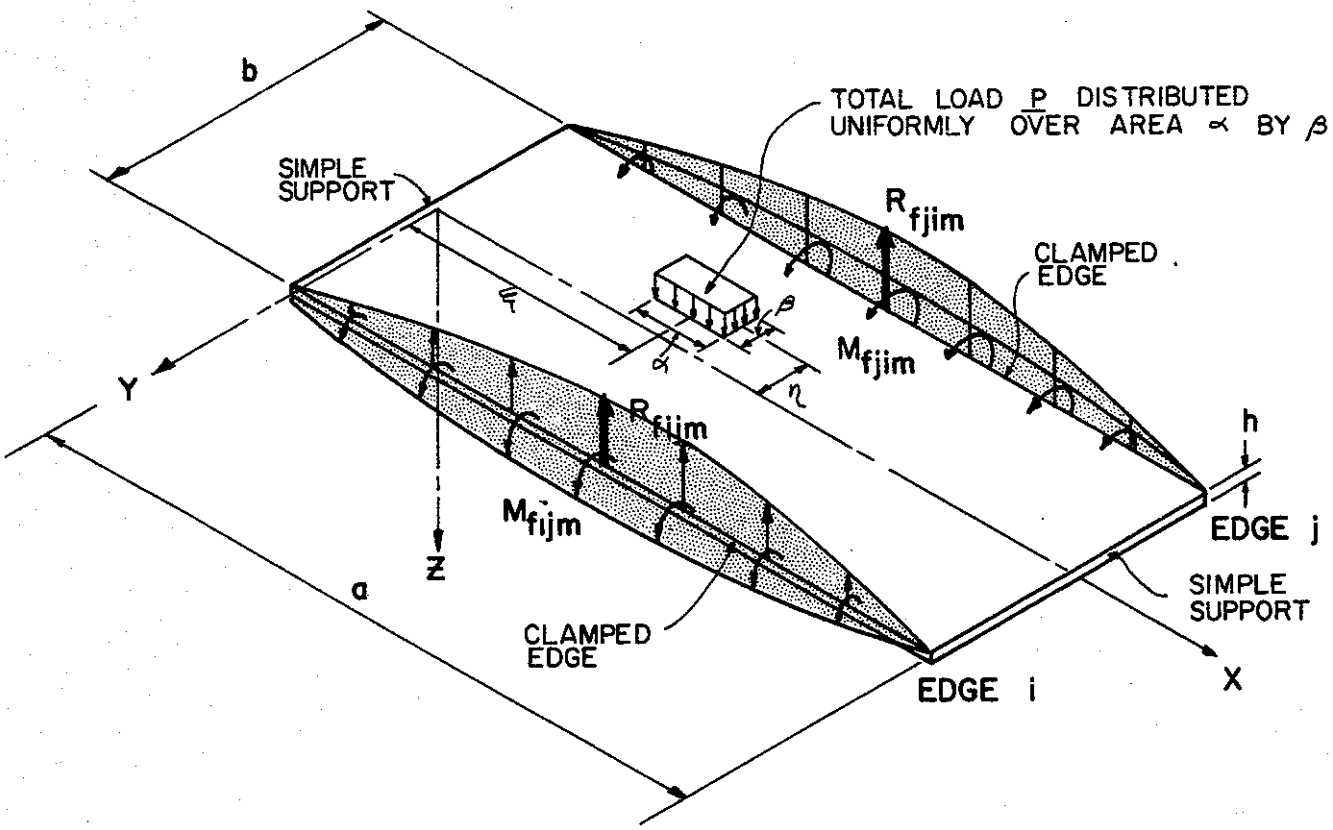

Figure 46. Fixed Edge Forces for Laterally Loaded Plate.

forces and edge-displacement induced forces. For edge i, the final forces will be given by

$$M_{ijm}\sin\frac{m\pi x}{a} = \{M_{fijm} + C_{1ijm}\phi_{ijm} + C_{2ijm}\phi_{jim} - C_{3ijm}W_{ijm} + C_{4ijm}W_{jim}\}\sin\frac{m\pi x}{a}$$

$$R_{ijm}\sin\frac{m\pi x}{a} = \{R_{fijm} + C_{5ijm}\phi_{ijm} + C_{6ijm}\phi_{jim} - C_{7ijm}W_{ijm} + C_{8ijm}W_{jim}\}\sin\frac{m\pi x}{a}$$

$$N_{ijm}\sin\frac{m\pi x}{a} = \{N_{fijm} - C_{9ijm}V_{ijm} + C_{10ijm}V_{jim} - C_{11ijm}U_{ijm} + C_{12ijm}U_{jim}\}\sin\frac{m\pi x}{a} \qquad (23)$$

$$S_{ijm}\cos\frac{m\pi x}{a} = \{S_{fijm} - C_{13ijm}V_{ijm} - C_{14ijm}V_{jim} - C_{15ijm}U_{ijm} + C_{16ijm}U_{jim}\}\cos\frac{m\pi x}{a}$$

Canceling sine and cosine terms from each side of the equations, and using a more compact matrix notation, Eqs, 23 become,

$$\begin{bmatrix} M \\ R \\ N \\ S \end{bmatrix} = \begin{bmatrix} M_f \\ R_f \\ 0 \\ 0 \end{bmatrix}_{ijm} + \begin{bmatrix} C_1 & C_2 & -C_3 & C_4 & 0 & 0 & 0 & 0 \\ C_5 & C_6 & -C_7 & C_8 & 0 & 0 & 0 & 0 \\ 0 & 0 & 0 & 0 & -C_9 & C_{10} & -C_{11} & C_{12} \\ 0 & 0 & 0 & 0 & -C_{13} & -C_{14} & -C_{15} & C_{16} \end{bmatrix}_{ijm} \begin{bmatrix} \phi_{ij} \\ \phi_{ji} \\ W_{ij} \\ W_{ji} \\ V_{ij} \\ V_{ji} \\ U_{ij} \\ U_{ji} \end{bmatrix}_m \tag{24}$$

For edge j, the final forces for the $m^{\underline{th}}$ harmonic are

$$\begin{bmatrix} M \\ R \\ N \\ S \end{bmatrix} = \begin{bmatrix} M_f \\ R_f \\ 0 \\ 0 \end{bmatrix}_{jim} \begin{bmatrix} C_2 & C_1 & -C_4 & C_3 & 0 & 0 & 0 & 0 \\ -C_6 & -C_5 & C_8 & -C_7 & 0 & 0 & 0 & 0 \\ 0 & 0 & 0 & 0 & C_{10} & -C_9 & -C_{12} & C_{11} \\ 0 & 0 & 0 & 0 & C_{14} & C_{13} & C_{16} & -C_{15} \end{bmatrix}_{jim} \begin{bmatrix} \phi_{ij} \\ \phi_{ji} \\ W_{ij} \\ W_{ji} \\ V_{ij} \\ V_{ji} \\ U_{ij} \\ U_{ji} \end{bmatrix}_m$$

The constants C_{1ijm} through C_{16ijm} are dependent on the dimensions and material properties of the plate. Expressions for them are given in Appendix A.

3.2.2 Force/displacement Relationships for a Beam Element

The beam elements are assumed to be rigidly attached to the bottom

face of the plates they support, and must therefore undergo displacements which are compatible with those of the edges of the plate elements. The edge-displacements of the plate elements are for points on the longitudinal edge of the plate, at mid-depth. Thus, to insure compatibility between plate and beam displacements, the force/displacement relationships for the beam element are referred to a reference point at mid-depth of the plates, as shown in Figure 47(a). The beam element is assumed to undergo the same four components of displacement as the edge of the plate. These are illustrated in Figure 47(b) through 47(e) for beam element i, and consist of i) a downward displacement $W_{im}\sin\frac{m\pi x}{a}$, ii) a rotation $\phi_{im}\sin\frac{m\pi x}{a}$, iii) a lateral movement $V_{im}\sin\frac{m\pi x}{a}$, and iv) a longitudinal translation $U_{im}\text{ocs}\frac{m\pi x}{a}$. These displacement components result in forces at the reference point of $R_{im}\sin\frac{m\pi x}{a}$, $M_{im}\sin\frac{m\pi x}{a}$, $N_{im}\sin\frac{m\pi x}{a}$ and $S_{im}\sin\frac{m\pi x}{a}$, as shown in Figures 48 and 49. The relationships between the force and displacement components are given by

$$\begin{bmatrix} M \\ R \\ N \\ S \end{bmatrix}_{im} \begin{bmatrix} B_1 & 0 & B_2 & 0 \\ 0 & B_3 & 0 & B_4 \\ B_5 & 0 & B_6 & 0 \\ 0 & 0 & B_7 & B_8 \end{bmatrix}_{im} \begin{bmatrix} \phi \\ W \\ V \\ U \end{bmatrix}_{im} \tag{26}$$

where the constants B_{1im} through B_{8im} are listed in Appendix A.

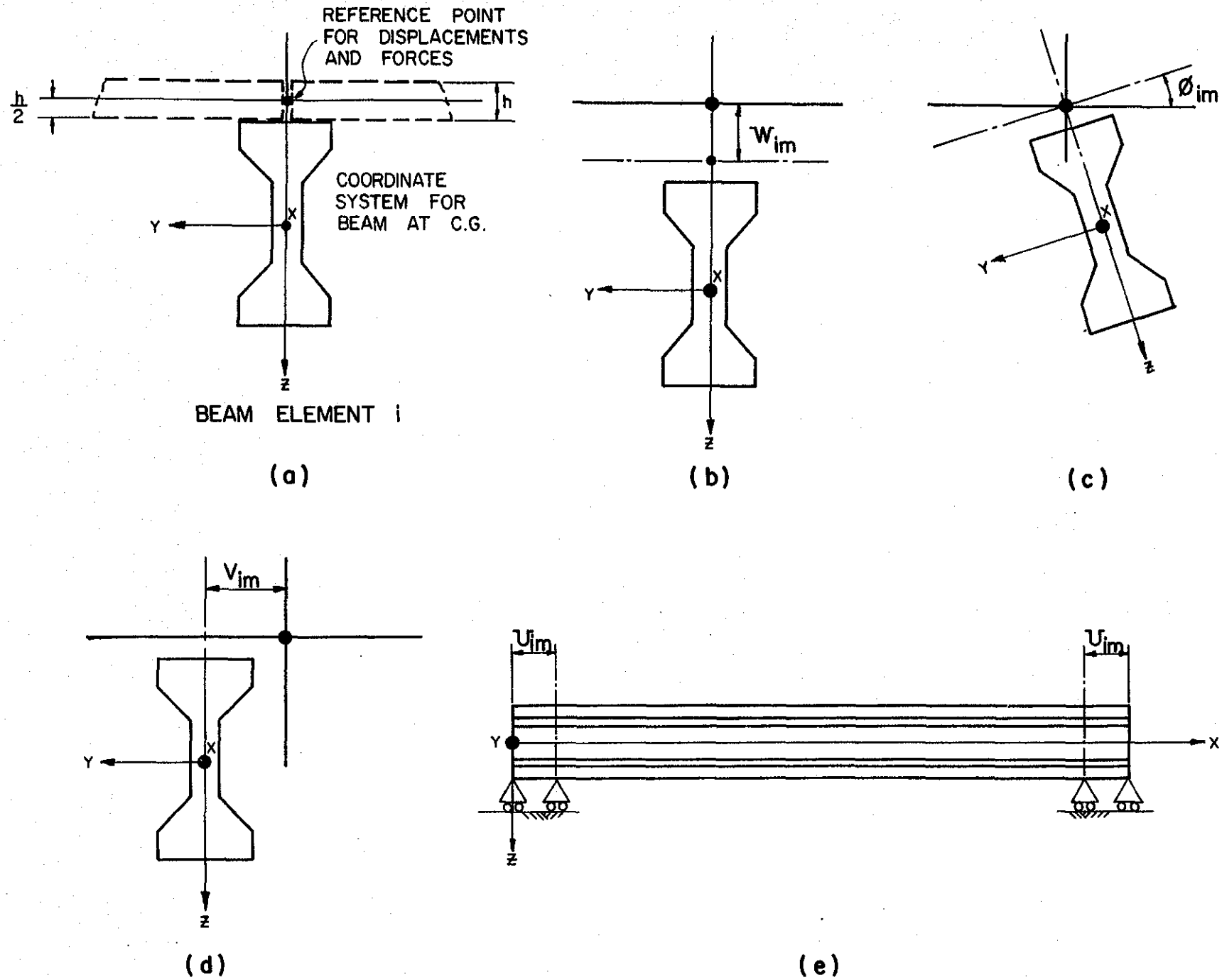

Figure 47. Displacements for Beam Element.

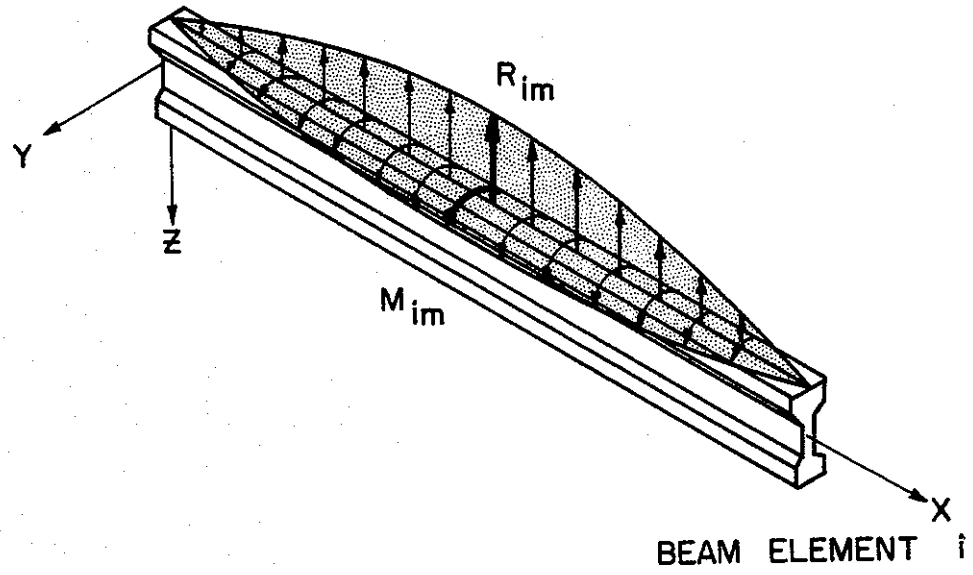

Figure 48. Forces from Downward Displacement and Rotation of Beam Element i.

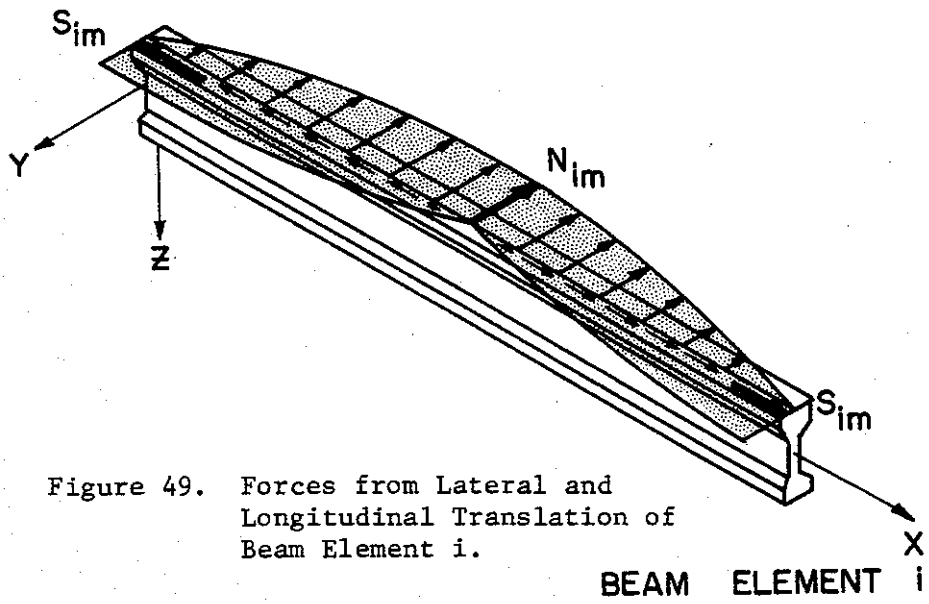

Figure 49. Forces from Lateral and Longitudinal Translation of Beam Element i.

3.2.3 Joint-force Equilibrium Equations

For the bridge structure to be in equilibrium under a set of loads, the summation of forces at the juncture of a beam element and the plate elements it supports must be zero, for all beam-plate joints in the bridge. The forces acting on a typical interior joint, between plates (i, j), (j,k) and beam j are shown in Figure 50. For the m^{th} harmonic in the load series expansion, a summation of forces along the three coordinate axes and a summation of movements, at the reference point yields the equations;

$$\begin{aligned}
\Sigma F_x &= 0 = \{S_{jim} + S_{jkm} + S_{jm}\} \cos\frac{m\pi x}{a} \\
\Sigma F_y &= 0 = \{N_{jim} + N_{jkm} + N_{jm}\} \sin\frac{m\pi x}{a} \\
\Sigma F_z &= 0 = \{R_{jim} + R_{jkm} + R_{jm}\} \sin\frac{m\pi x}{a} \\
\Sigma M_x &= 0 = \{M_{jim} + M_{jkm} + M_{jm}\} \sin\frac{m\pi x}{a}
\end{aligned} \tag{27}$$

A cancellation of the sine or cosine terms in the product yields a linear set of equations in the force amplitudes. Letting the amplitudes of the four components of displacement at joints i, j and k be denoted by $(\overline{\phi}_{im}, \overline{W}_{im}, \overline{V}_{im}, \overline{U}_{im})$, $(\overline{\phi}_{jm}, \overline{W}_{jm}, \overline{V}_{jm}, \overline{U}_{jm})$ and $(\overline{\phi}_{km}, \overline{W}_{km}, \overline{V}_{km}, \overline{U}_{km})$ and noting that compatibility of displacements requires

$$\begin{bmatrix} \phi \\ W \\ V \\ U \end{bmatrix}_{ijm} = \begin{bmatrix} \overline{\phi} \\ \overline{W} \\ \overline{V} \\ \overline{U} \end{bmatrix}_{im} \qquad \begin{bmatrix} \phi \\ W \\ V \\ U \end{bmatrix}_{kjm} = \begin{bmatrix} \overline{\phi} \\ \overline{W} \\ \overline{V} \\ \overline{U} \end{bmatrix}_{km} \tag{28}$$

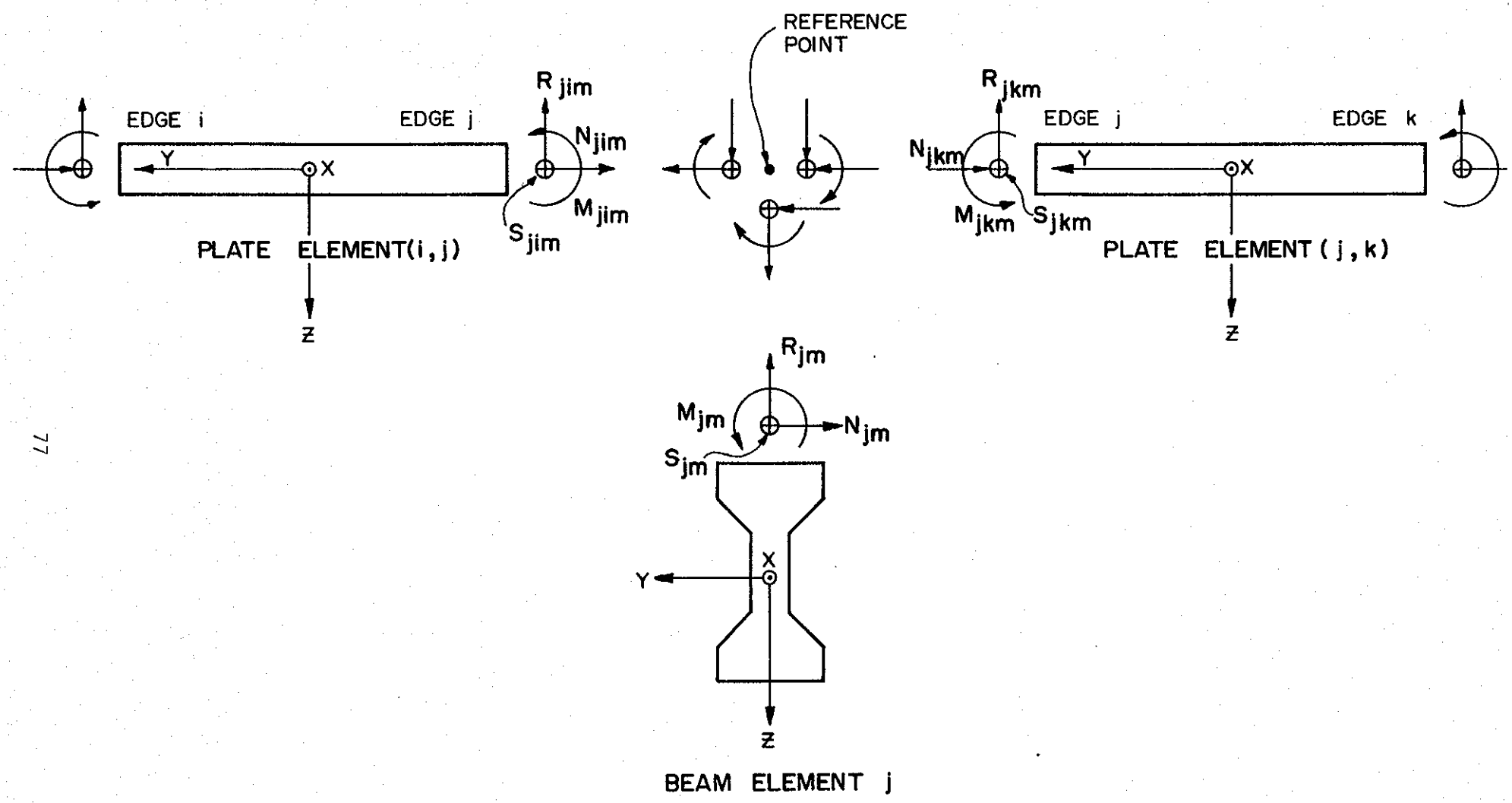

Figure 50. Joint Forces at Juncture of Beam and Plate Elements.

$$\begin{bmatrix} \phi \\ W \\ V \\ U \end{bmatrix}_{jim} = \begin{bmatrix} \phi \\ W \\ V \\ U \end{bmatrix}_{jm} = \begin{bmatrix} \phi \\ W \\ V \\ U \end{bmatrix}_{jkm} = \begin{bmatrix} \overline{\phi} \\ \overline{W} \\ \overline{V} \\ \overline{U} \end{bmatrix}_{jm} \tag{29}$$

leads to a set of simultaneous linear equations in the joint displacement components. Substituting Eqs. 24, 25, and 26 into 27, gives the following four simultaneous equations in joint displacements:

$$\begin{aligned}
-M_{fjim} - M_{fjkm} &= C_{2ijm}\,\overline{\phi}_{im} - C_{4ijm}\,\overline{W}_{im} + (C_{1ijm} + C_{1jkm} \\
&\quad + B_{1jm})\,\overline{\phi}_{jm} + (C_{3ijm} - C_{3jkm} + B_{2jm})\,\overline{W}_{jm} \\
&\quad + C_{2jkm}\,\overline{\phi}_{km} + C_{4jkm}\,\overline{W}_{km} \\
-R_{fjim} - R_{fjkm} &= -C_{6ijm}\,\overline{\phi}_{im} - C_{8ijm}\,\overline{W}_{im} + (-C_{5ijm} + C_{5jkm}) \\
&\quad \overline{\phi}_{jm} + (-C_{7ijm} - C_{7jkm} + B_{3jm})\,\overline{W}_{jm} + B_{4jm}\,\overline{U}_{jm} \\
&\quad + C_{6jkm}\,\overline{\phi}_{km} + C_{8jkm}\,\overline{W}_{km} \\
0 &= C_{10ijm}\,\overline{V}_{im} - C_{12ijm}\,\overline{U}_{im} + B_{5jm}\,\overline{\phi}_{jm} + (B_{6jm} - C_{9ijm})\,\overline{V}_{jm} \\
&\quad - C_{11jkm}\,\overline{U}_{jm} + C_{10jkm}\,\overline{V}_{km} + C_{12jkm}\,\overline{U}_{km} \\
0 &= -C_{13ijm}\,\overline{V}_{im} - C_{15ijm}\,\overline{U}_{im} + (C_{14jkm} - C_{14ijm} + B_{7jm})\,\overline{V}_{jm} \\
&\quad + (C_{16jkm} + C_{16ijm} + B_{8jm})\,\overline{U}_{jm} + C_{13jkm}\,\overline{V}_{km} \\
&\quad - C_{15jkm}\,\overline{U}_{km}
\end{aligned} \tag{30}$$

In a similar manner, four additional equations can be determined for each

plate-beam joint in the bridge. The resulting system of equations relates the amplitudes of displacement components at each joint in the bridge to the amplitudes of the series expansions for the loads on the bridge, for a particular harmonic in the series expansion. The solution of these equations determines values for the displacement amplitudes, which can then be used to compute moments, stresses or strains at any point in a plate or beam element. The results of an analysis for each harmonic used in the load series expansion can then be superimposed to obtain the total moments, stresses and strains existing in the loaded structure.

3.3 Comparison With Examples From the Literature

The method of analysis described in the preceding section was programmed for digital computer, and the program was used to analyze several plate and beam structures described in the literature to test the validity of the method.

The first example considered, taken from Reference (11), was the rectangular plate shown in Figure 51 (a). The plate was simply supported on all four edges and carried a uniformly distributed load of 0.625 lbs,/in^2 over a 40 in. by 40 in. area at the center of the plate. The plate is 6.0 in. thick, with a modulus of elasticity of 10^6 psi and Poisson's ratio of 0.3.

The structure shown in Figure 51 (c), with supporting beams along the two edges of the plate parallel to the X-axis, was used

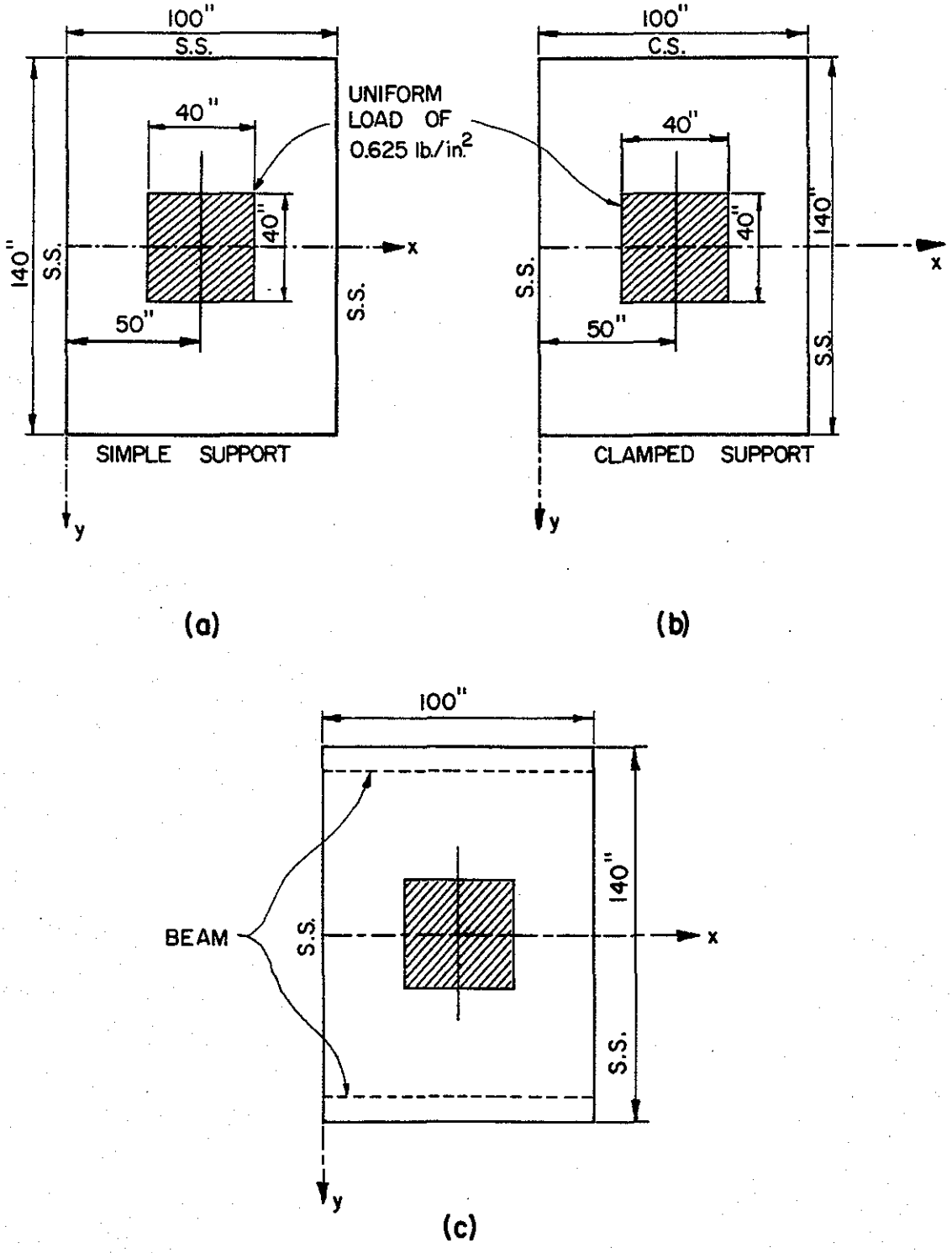

Figure 51. Example Problem No. 1.

to simulate the plate in Figure 51(a). The simple support conditions along the two edges parallel to the X-axis were obtained for the structure in Figure 51(c) by setting the torsional resistance of the beams to zero and assigning a large value (10^8) to their moments of inertia. The bending moments in the x and y directions at the center of the plate were computed by the program, and are compared with those from Reference (11) in Table 4.

The second example tested was identical to the first, except that the edges of the plate parallel to the X-axis were clamped (see Fig. 51(b)). The fixed edge condition was simulated with the computer model by setting both the torsional stiffness and moment of inertia of the beams equal to a large number. A comparison of bending moments and downward displacement at the center of the plate are compared with those from Reference (11) in Table 5.

As a final check, the methods of analysis developed for this study was used to analyze a 100 ft. span composite slab and girder bridge. This example was considered in Reference (12) using the finite element technique. The bridge consisted for four steel plate girders, with 14.0 in. by 1.75 in. flanges and a 71.6 in. by 0.375 in. web, spaced laterally at 100 in. centers. The slab was 7.5 in. thick and overhung the out side girders by 50 in. Reference (12) did not give material properties, so modulus of elasticity values of 29 million and 3.2 million were assumed for the beams and slab, respectively. Poisson's ratio for the slab was taken as 0.166 and the torsional stiffness was

TABLE 4

COMPARISON OF BENDING MOMENTS FOR EXAMPLE NO. 1

	M_x (in-lb/in)	M_y (in-lb/in)
Ref. (11)	168.0	138.0
Folded Plate Analysis	167.8	138.4

TABLE 5

COMPARISON OF BENDING MOMENTS AND DEFLECTION FOR EXAMPLE NO. 2

	M_x (in-lb/in)	M_y (in-lb/in)	w (in)
Ref. (11)	36.7	32.0	.00166
Folded Plate Analysis	37.2	32.0	.00168

TABLE 6

COMPARISON OF TRANSVERSE BENDING MOMENTS IN THE DECK SLAB ADJACENT TO BEAMS FOR EXAMPLE NO. 2

Load Position	Location	Solution	Transverse Slab Moment M_y at Beam:			
			A	B	C	D
Line Load on Outside Beam A	1/4 span	Ref. (12)	1.46	-11.86	-6.49	-0.37
		Folded Plate Analysis	1.19	-11.06	-5.55	-0.26
	1/2 span	Ref. (12)	2.06	-16.76	-9.14	-0.52
		Folded Plate Analysis	1.77	-15.64	-7.91	-0.37
Line Load on Inside Beam B	1/4 span	Ref. (12)	-0.43	19.06	-0.20	-0.60
		Folded Plate Analysis	-0.43	17.86	-0.89	-0.50
	1/2 span	Ref. (12)	-0.61	26.92	-0.30	-0.85
		Folded Plate Analysis	-0.61	25.26	-1.25	-0.71

assumed to be zero. The bridge was analyzed for two load conditions a line load $\sin \frac{\pi x}{L}$ applied over an outside beam and over an inside beam. Table 6 lists a comparison of transverse bending moments adjacent to each beam at quarter and mid-span for each load condition.

IV. PRESENTATION AND ANALYSIS OF RESULTS

The loading and instrumentation systems used for the testing of the full-scale bridge model and the slab segment model were devised to monitor changes in the static response of the structures after the application of cyclic loads. The capacity of the loading system was chosen so that loads large enough to cause failure in the deck slab could be applied. The sequence of cyclic load-static response load tests and the static load to failure tests was described in Section 2.7. This section presents a summary of the results of those tests and an evaluation of the overall performance of the structures.

The primary means used to determine the state of composite action between beams, panels and cast-in-place deck was by comparison of static load response, as reflected by strain and deflection measurements, before and after cyclic loading, and by comparison of the response to that predicted for a fully composite structure, as determined from the folded plate analysis method developed in Chapter 3. It should be noted that this mathematical model does not identically duplicate the physical prototype because of the discontinuity in the deck at butt joints between panels. Thus, in the area immediately adjacent to a joint, the actual stress distribution should differ somewhat from that predicted by mathematical model.

The stresses, strains and displacements from the folded plate analysis which are used for comparison with measured quantities were

obtained by imputing the actual loads, the dimensions and material properties of the bridge model to the computer program and specifying that stresses, strains and displacements be computed at those points on the structure where instrumentation was located.

4.1 Repetitive Load Tests of Full-Scale Bridge Model

Plots of beam deflections for static load applied at positions 1 through 3 (see Fig. 33) before cyclic loading and after 2 million cycles of load are presented in Figures 52 through 54. Close comparisons of deflections before and after cyclic loading indicate that no loss of stiffness was caused by the loading. This statement is further supported by the fact that no slippage between the beams and the slab was indicated by the relative displacement dial gages. Had composite action between the beams and the slab not existed, the deflections would have increased above those for composite action. The increase in deflections would be proportional to the ratio of the moments of inertia for the composite and noncomposite sections--other influences such as loss of torsional stiffness being ignored. This ratio for the test structure was about 2.4.

Experimentally measured strains at the upper and lower surface of the slab at locations in the proximity of the simulated wheel pads are presented in Tables 7 through 9. The generally close agreement between values obtained from the static load response tests made before and after cyclic loading indicate that no distress was caused by the cyclic loading. In some isolated instances, such as gages 26,

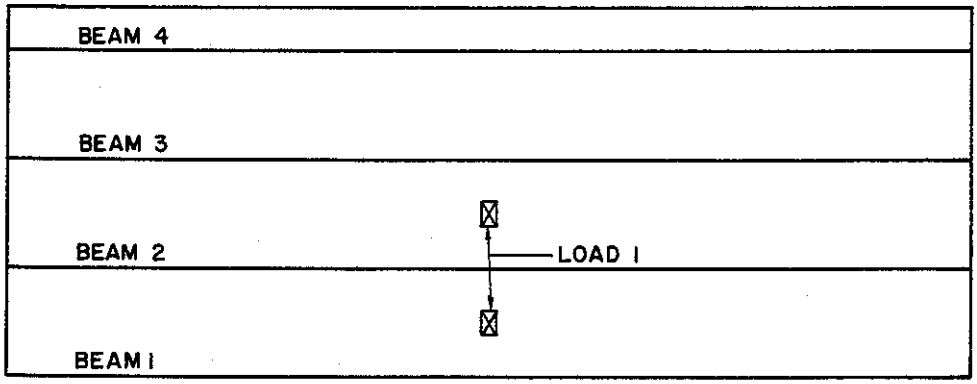

PLAN VIEW OF LOAD POSITION

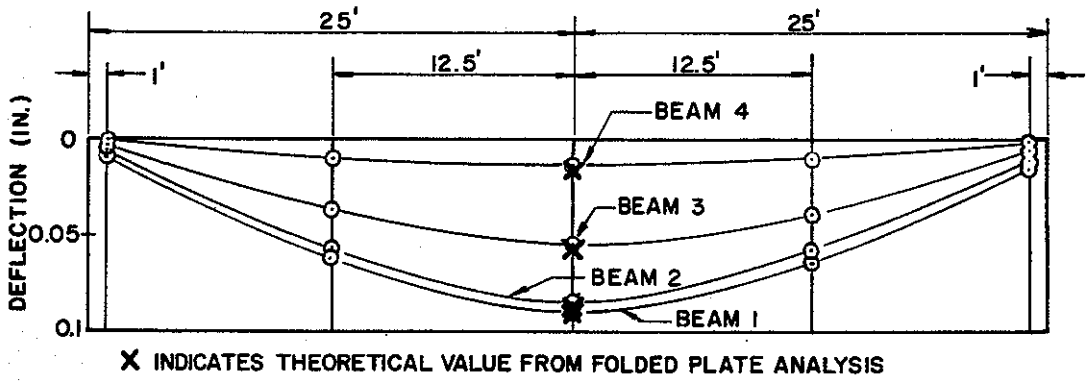

X INDICATES THEORETICAL VALUE FROM FOLDED PLATE ANALYSIS

a.)BEFORE CYCLIC LOADING IN POSITION 1

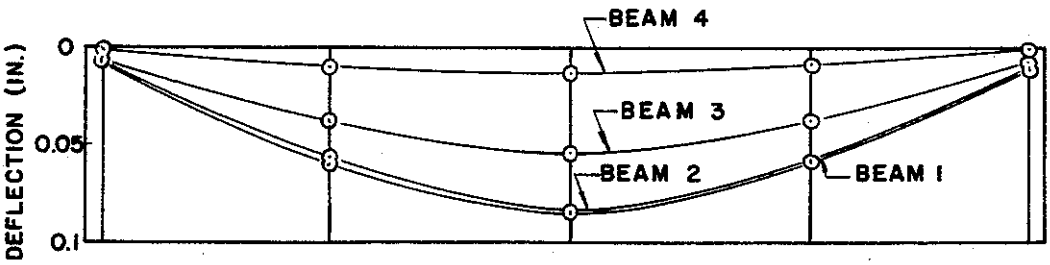

b.) AFTER 2×10^6 CYCLES IN POSITION 1

Figure 52. Theoretical and Experimental Beam Deflections for Load 1.

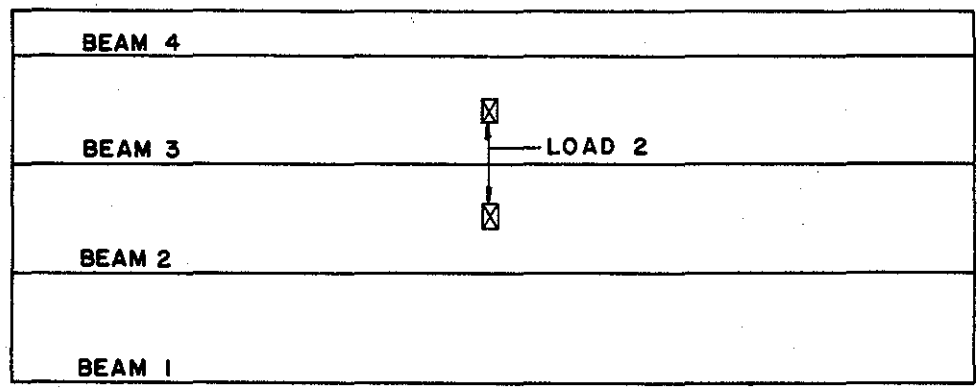

PLAN VIEW OF LOAD POSITION

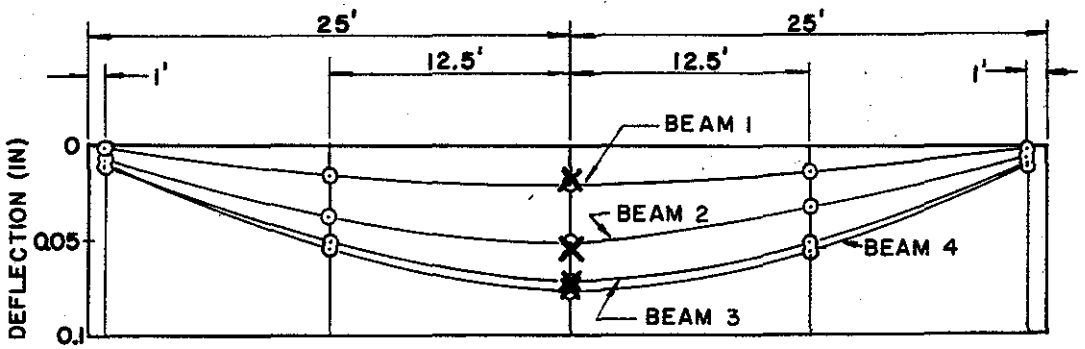

X INDICATES THEORETICAL VALUE FROM FOLDED PLATE ANALYSIS

a.) BEFORE CYCLIC LOADING IN POSITION 2

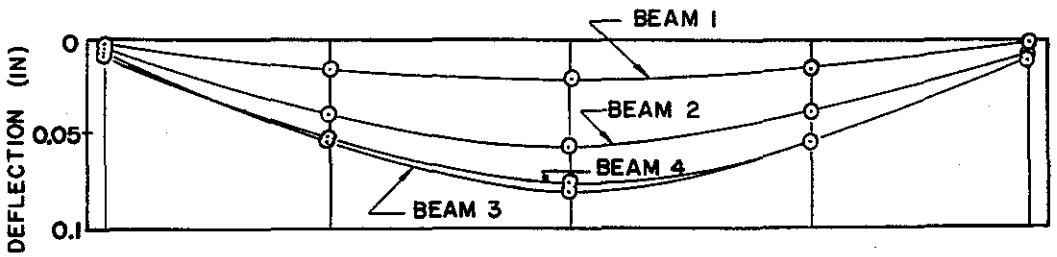

b.) AFTER 2×10^6 CYCLES IN POSITION 2

Figure 53. Theoretical and Experimental Beam Deflections for Load 2.

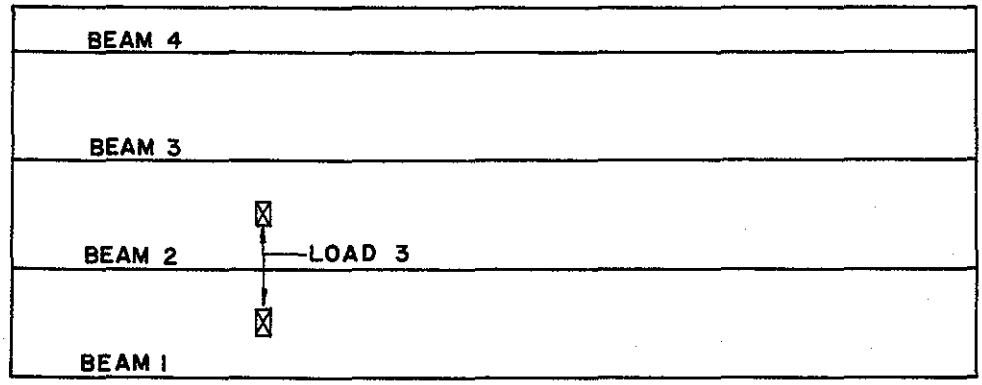

PLAN VIEW OF LOAD POSITION

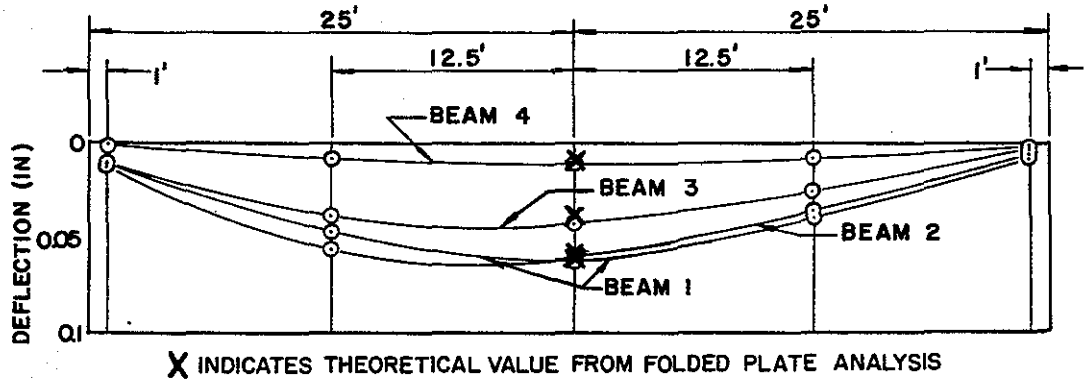

X INDICATES THEORETICAL VALUE FROM FOLDED PLATE ANALYSIS

a.)BEFORE CYCLIC LOADING IN POSITION 3

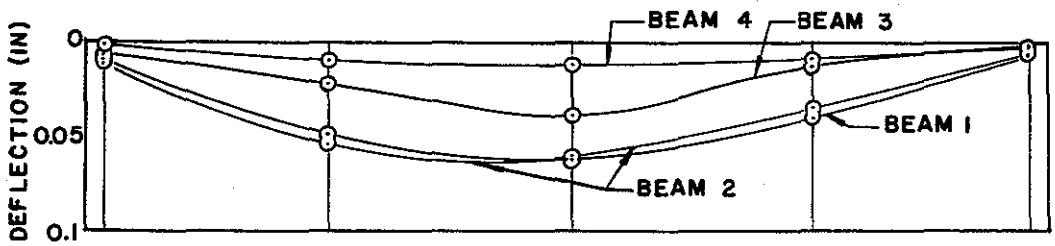

b.) AFTER 2×10^6 CYCLES IN POSITION 3

Figure 54. Theoretical and Experimental Beam Deflections for Load 3.

TABLE 7. EXPERIMENTAL AND THEORETICAL STRAINS FOR LOAD POSITION 1

Axle Load of 48 kips

	Strain Gage Identification	Experimental Strain micro. in. per in.		Theoretical Strain from Folded Plate Analysis micro. in. per in.
		Before Cyclic Loading	After Cyclic Loading	
Longitudinal Gages	25[a]	-11	-15	-27
	26	-26	-17	-28
	27	-14	-13	-22
	28	-20	-14	-34
	29	-56	-56	-56
	30	+ 1	- 2	- 2
	31	-16	-14	-22
	32	-19	-15	-34
	33	-15	-14	-27
	34	-16	-13	-28
Transverse Gages	35	-18	-23	-24
	36	+14	+26	+31
	37	-39	-27	-29
	38	+20	+33	+37
	39	-74	-76	-65
	40	+61	+74	+71
	41	-28	-24	-29
	42	+25	+36	+37
	43	-39	-38	-24
	44	+18	+24	+31

[a]Odd numbered gages were on top surface and even numbered gages were directly below on bottom surface of slab.

TABLE 8. EXPERIMENTAL AND THEORETICAL STRAINS FOR LOAD POSITION 2

Axle Load of 48 kips

	Strain Gage Identification	Experimental Strain micro. in. per in.		Theoretical Strain from Folded Plate Analysis micro. in. per in.
		Before Cyclic Loading	After Cyclic Loading	
Longitudinal Gages	45[a]	- 9	- 5	-18
	46	-15	-14	-21
	47	- 3	- 4	-13
	48	-17	-14	-27
	49	-32	-32	-46
	50	+ 7	+ 1	+ 5
	51	- 7	- 7	-13
	52	-23	-19	-27
	53	-23	-24	-18
	54	-23	-19	-21
Transverse Gages	55	-21	-21	-23
	56	+22	+24	+30
	57	-31	-27	-28
	58	+47	+34	+35
	59	-77	-62	-63
	60	+75	+76	+69
	61	-32	-29	-28
	62	+31	+36	+35
	63	-11	-12	-23
	64	+25	---[b]	+30

[a]Odd numbered gages were on top surface and even numbered gages were directly below on bottom surface of slab.

[b]No data.

TABLE 9. EXPERIMENTAL AND THEORETICAL STRAINS FOR LOAD POSITION 3

Axle Load of 48 kips

	Strain Gage Identification	Experimental Strain micro. in. per in.		Theoretical Strain from Folded Plate Analysis micro. in. per in.
		Before Cyclic Loading	After Cyclic Loading	
Longitudinal Gages	65[a]	- 4	-10	-17
	66	- 8	-14	-11
	67	- 6	-11	-17
	68	-10	-18	-13
	69	-12	-18	-34
	70	-13	-21	- 5
	71	-13	-18	-36
	72	- 3	-20	- 8
	73	-16	-25	-20
	74	+ 3	+ 3	-24
Transverse Gages	75	- 7	-14	-11
	76	+13	+ 9	+16
	77	-12	-20	-14
	78	+17	+13	+19
	79	-52	-59	-54
	80	+53	+51	+48
	81	-50	-58	-54
	82	+66	+56	+58
	83	-54	-57	-40
	84	+50	+40	+45

[a]Odd numbered gages were on top surface and even numbered gages were directly below on bottom surface of slab.

36, 37, 38, 42, 58, 68, 72, and 75 (Fig. 18), the agreement is not close, but no consistent pattern that would indicate distress could be extracted from the data. Gage 25, which is directly above 26, showed a slight increase in longitudinal strain and gage 26 showed a decrease. Gages 37 and 38 showed a decrease in transverse strain on the top and an increase on the bottom. Changes in the measured strains that would be expected as a result of bond failure would be related to changes in the section modulus of the slab. The total section modulus of the slab in the case of no bond at the panel to cast-in-place interface is only half that of the section modulus of the composite slab. Therefore, total failure of the bond at this interface, over a widespread area, would be indicated by an increase of about 100 percent in the slab strains caused by local bending. The strains can be grouped on the basis of gage location, into two groups--those adjacent to a panel butt joint and those that are not. Excellent agreement between theoretical (folded plate analysis) and experimental strains was obtained for gage positions not adjacent to a panel joint. (Compare, for example, the measured and theoretical strain values for gages 29, 30, 39, and 40 in Table 7; 49, 50, 59, and 60 in Table 8; and 69, 70, 79, and 80 in Table 9.) Transverse gages adjacent to a panel butt joint show less satisfactory agreement, but no apparent trends are indicated. (Compare the measured and theoretical values for gages 35, 36, 37, 38, 41, 42, 43, and 44 in Table 7; gages 55, 56, 57, 58, 61, 62, 63, and 64 in Table 8; and

gages 75, 76, 77, 78, 81, 82, 83, and 84 in Table 9.) Longitudinal gages adjacent to butt joints showed the poorest agreement among all gages, with theoretical values being consistently higher than measured ones. (Compare the measured and theoretical values for gages 25, 26, 27, 28, 31, 32, 33, and 34 in Table 7; gages 45, 46, 47, 48, 51, 52, 53, and 54 in Table 8; and gages 65, 66, 67, 68, 71, 72, 73, and 74 in Table 9.) Discrepancies in these readings were expected, since the folded plate analysis does not account for the discontinuity at panel butt joints.

Stresses were computed from the measured slab strains using the plane stress relationships:

$$\sigma_L = \frac{E}{1 - \mu^2} (\varepsilon_L + \mu\varepsilon_T)$$

$$\sigma_T = \frac{E}{1 - \mu^2} (\varepsilon_T + \mu\varepsilon_L) \qquad (31)$$

where

σ_L = stress in the longitudinal direction of bridge

σ_T = stress in the transverse direction of bridge

ε_L = strain in the longitudinal direction

ε_T = strain in the transverse direction

E = 5.23×10^6psi. for cast-in-place concrete
5.65×10^6psi. for prestressed panel concrete

μ = 0.15

Strains from adjacent longitudinal and transverse gages were assumed

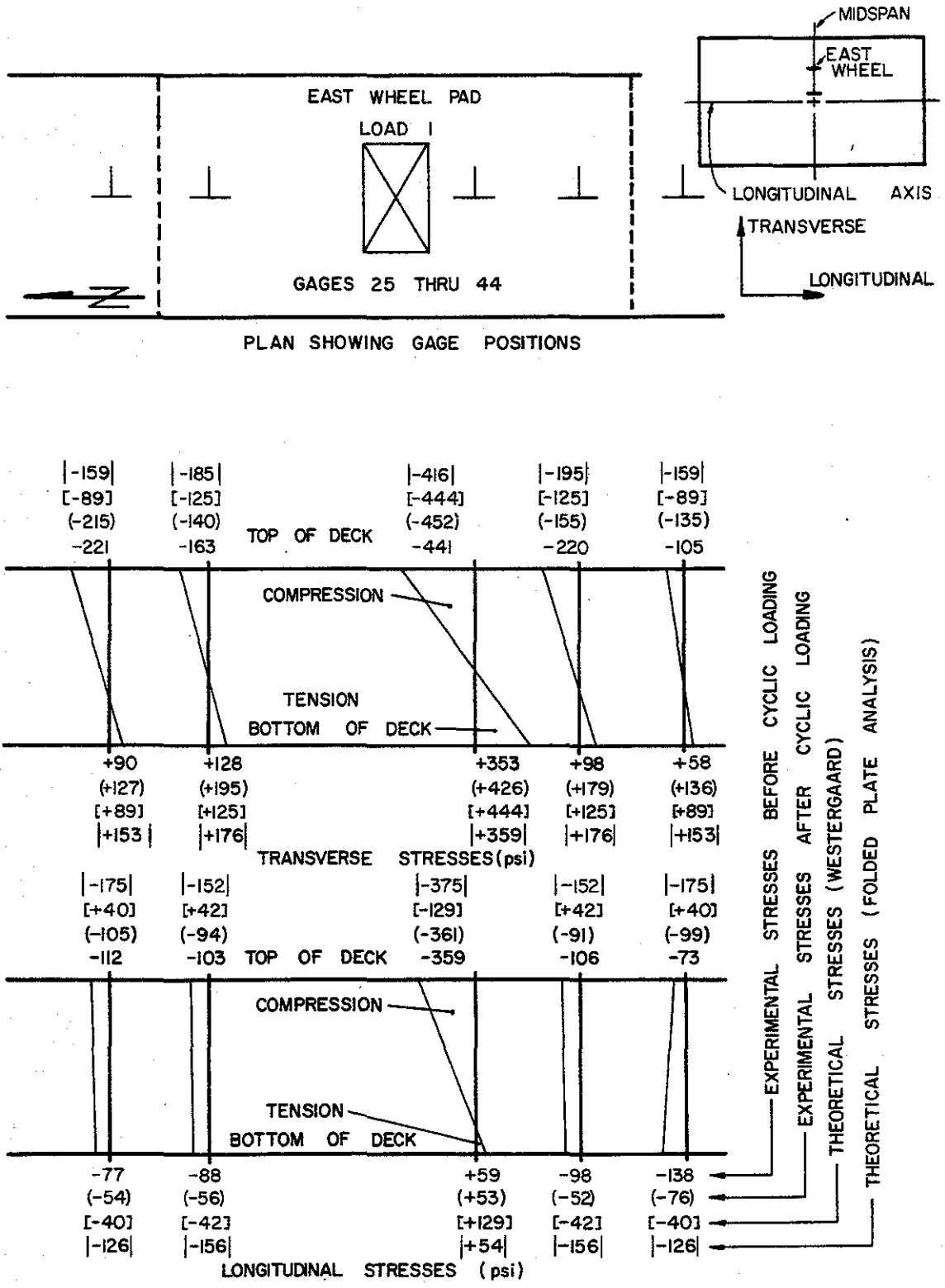

Figure 55. Stresses Computed from Experimental Strains near East Wheel Pad of Load 1.

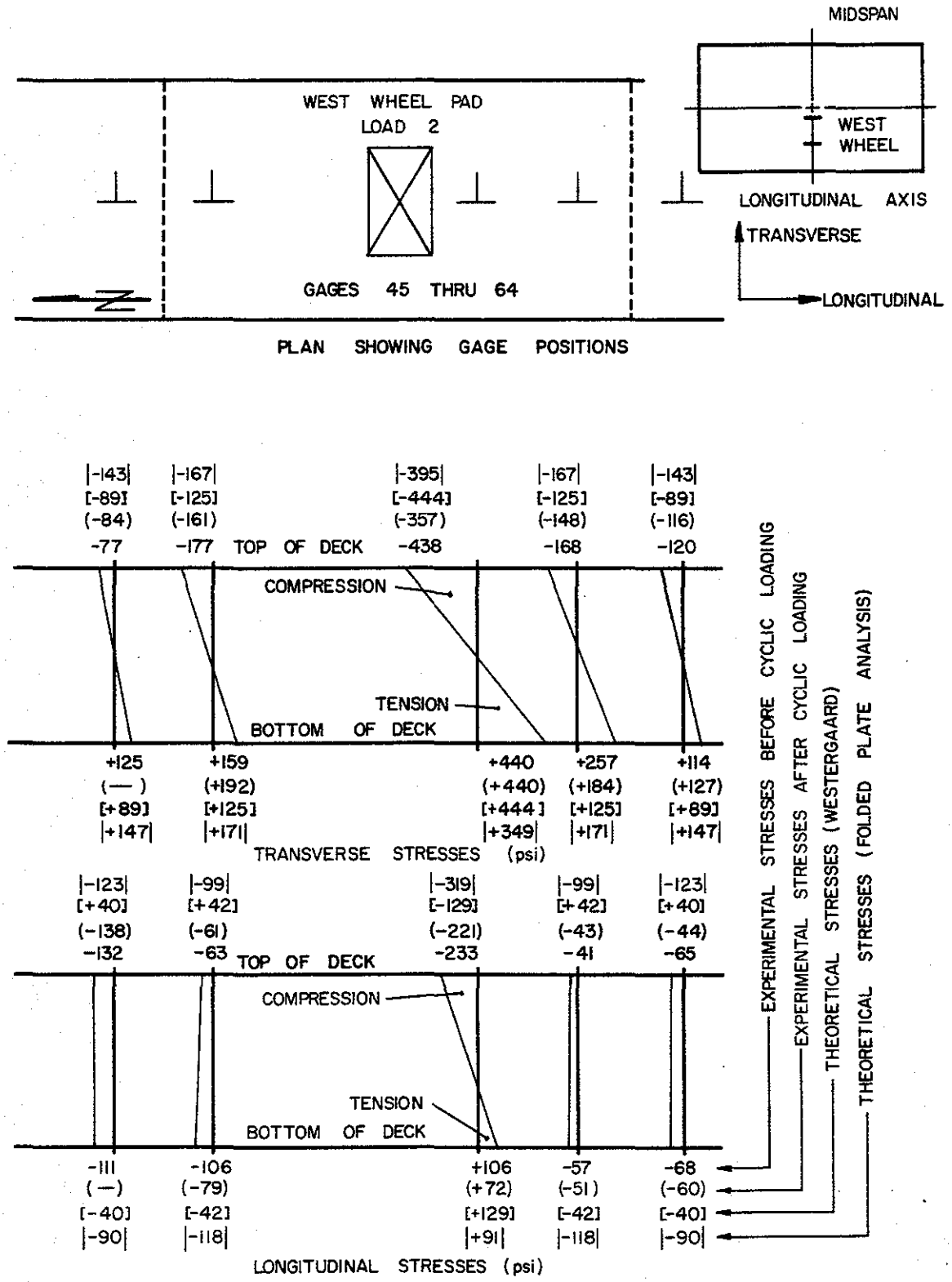

Figure 56. Stresses Computed from Experimental Strains near West Wheel Pad of Load 2.

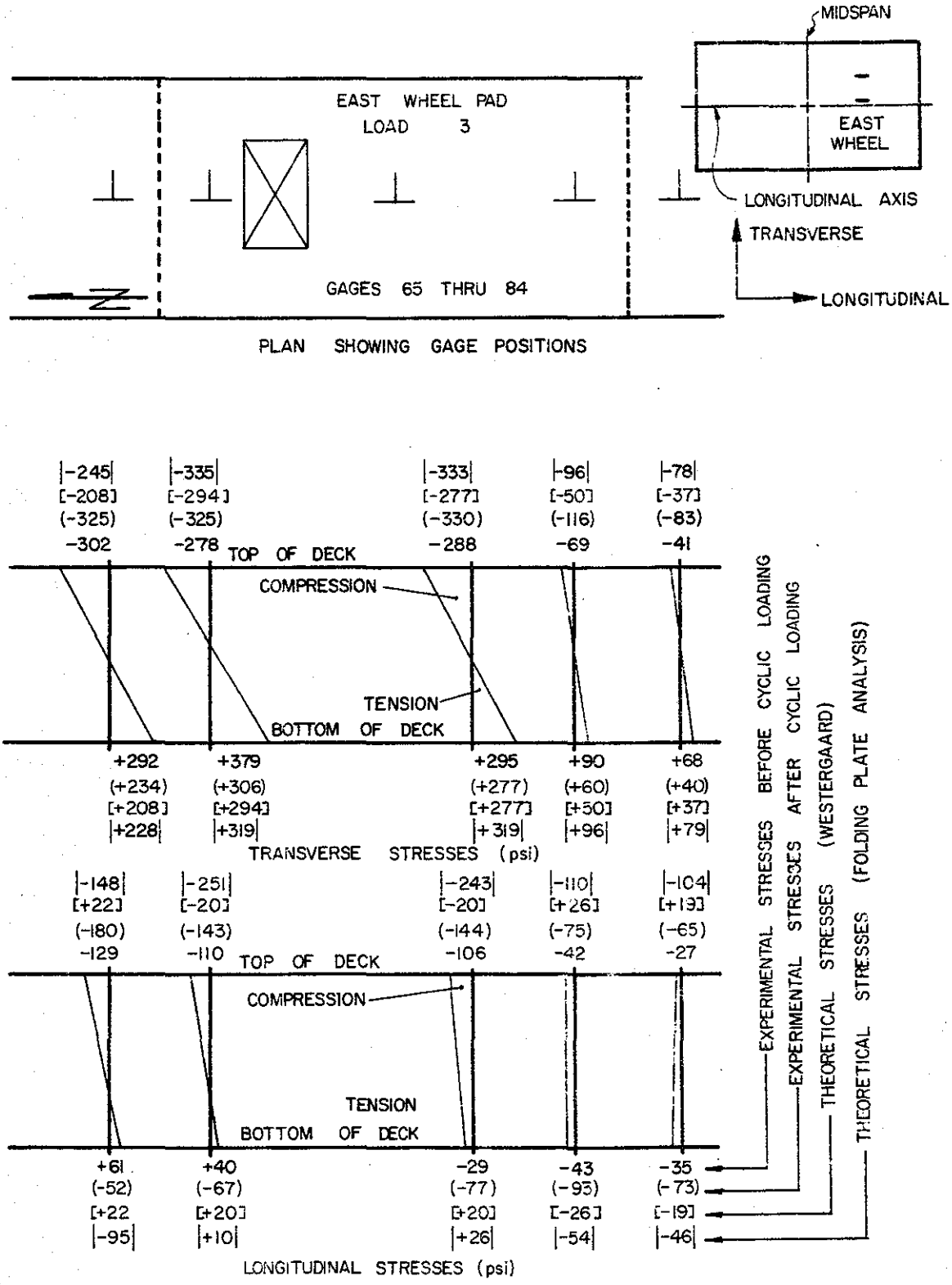

Figure 57. Stresses Computed from Experimental Strains near East Wheel Pad of Load 3.

to be at the same point for purposes of these calculations, although the midpoints of the strain gages were separated by approximately 2 in. as shown in Figure 19. The results of these calculations are presented in Figures 55 through 57. Also shown there, for comparison, are two sets of theoretical stresses. One set of theoretical values was obtained from the folded plate analysis, and the other set from the slab bending moment equations developed in Section 3.1.

Transverse stresses were calculated from the second of Eqs. (9), with an adjustment for the effect of continuity of the slab with the beams. The magnitudes of the adjustments were taken to be 50 percent of that obtained from Westergaard's solution for the effect of fixity; this choice being based on the following recommendation by Jensen:

> It may be observed from . . . that the correction to M_{ox} due to continuity of the slab is 42 percent of the correction due to fixing the slab. Similarly it may be observed that the correction due to continuity is 49 percent of the correction to M_{oy} due to fixing the slab. It is apparent, therefore, that the continuos slab is not in this instance, one having a definite "percentage of fixity", but may, nevertheless, be treated as "50 percent fixed" with a satisfactory degree of approximation. (13)

The concrete and steel areas were all transformed, on the basis of their relative moduli of elasticity, to an equivalent area of cast-in-place concrete. This transformation had negligible effect on the location of the neutral axis, but did increase the moment of inertia above that for the section without transformed areas.

The longitudinal stresses were computed using the first of

Eqs. (9). These computed stresses are due solely to local bending of the slab and do not include those stresses resulting from bending of the entire structure as a composite unit. More meaningful comparison between measured and theoretical values can be obtained by dividing longitudinal stresses into two components--one resulting from local bending of the slab only. The distribution of stresses into these two components was accomplished in the following manner. The values of the component of bending stresses attributable to bending of the composite structure, at the top and bottom surface of the slab, were assumed to be proportional to the distances of these two surfaces from the neutral surface of the composite unit (Fig. 58). The components of stress resulting from local bending of the slab were arbitrarily assigned equal values, of opposite sign, at the top and bottom surface of the slab. This allowed a unique solution for the distribution of the total stresses into the two components. Stresses computed from strain measurements made both before and after cyclic loading in each case were used for these computations. Values of stress obtained in this manner are presented in Figures 59 through 61.

Futher comparisons between experimental stresses and those predicted by theory as a function of longitudinal distance from the wheel pad are made in Figures 62 and 63. Adjustments to Eqs. 9 and 12 for 50 percent edge fixity, as discribed above, were made in arriving at the theoretical curves. Experimental data points for these plots were taken from Figures 55 through 57 and 59 through 61.

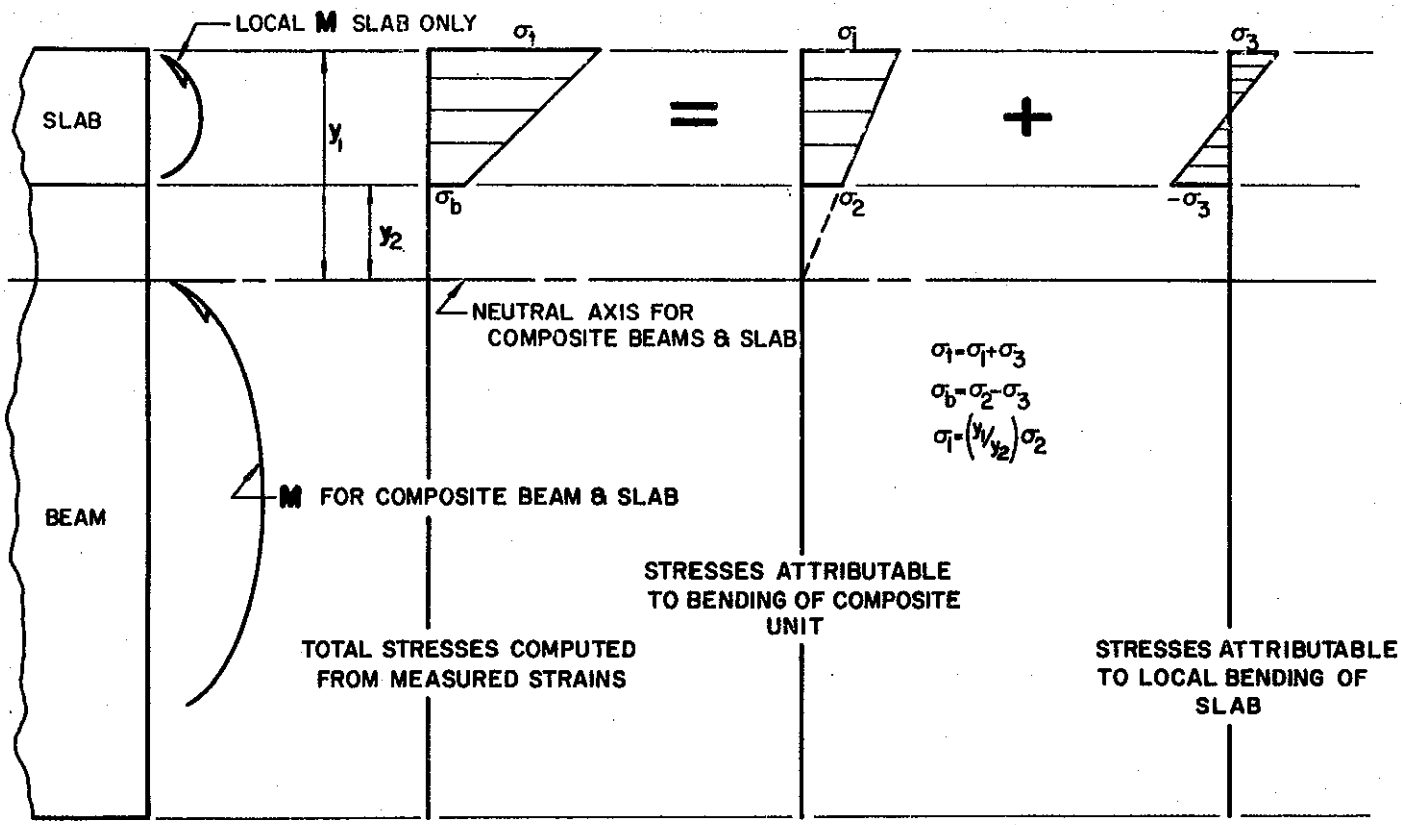

Figure 58. Division of Longitudinal Slab Stresses into Components.

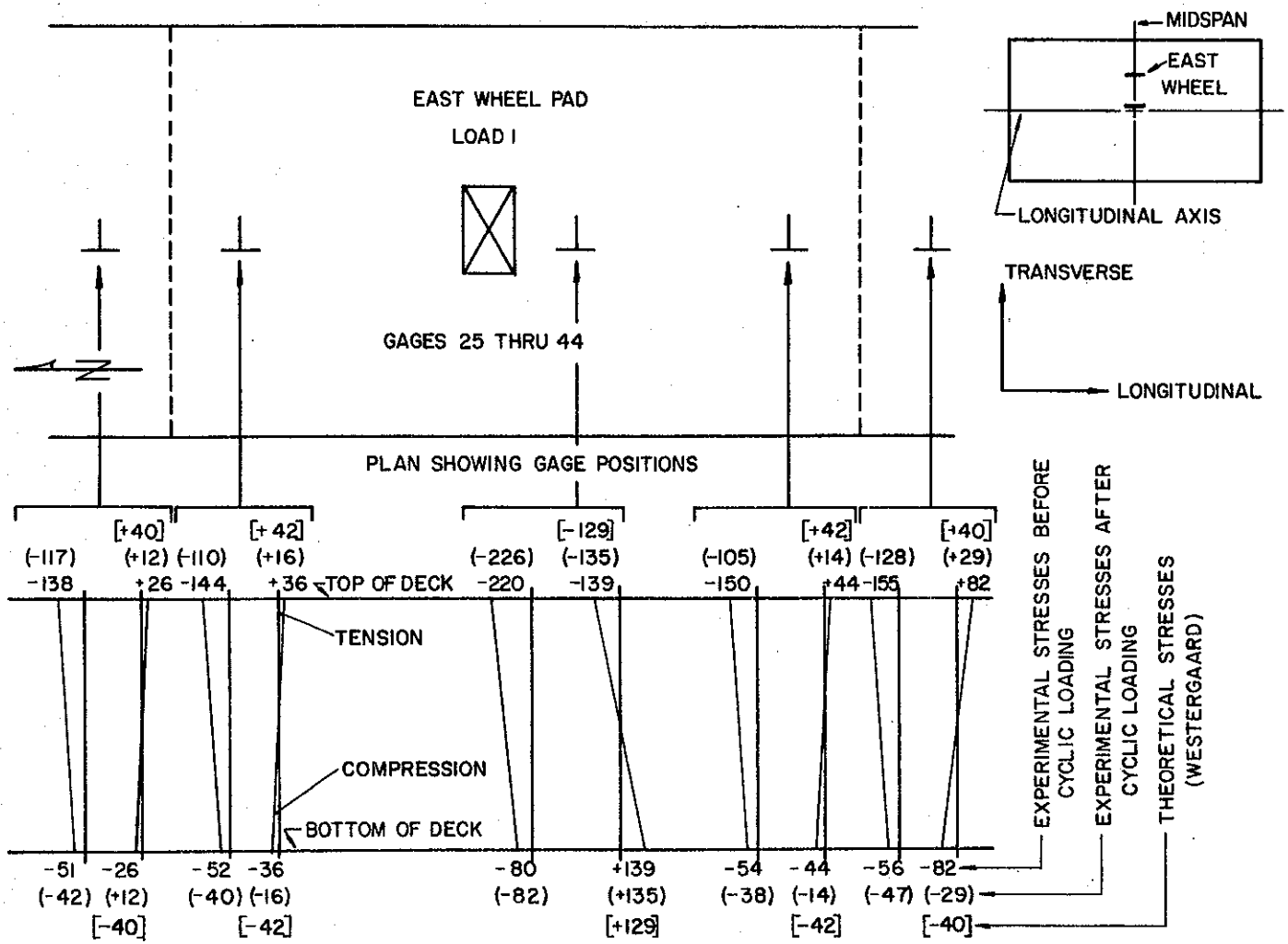

Figure 59. In-plane and Bending Stress Components Computed from Experimental Strains near East Wheel Pad of Load 1.

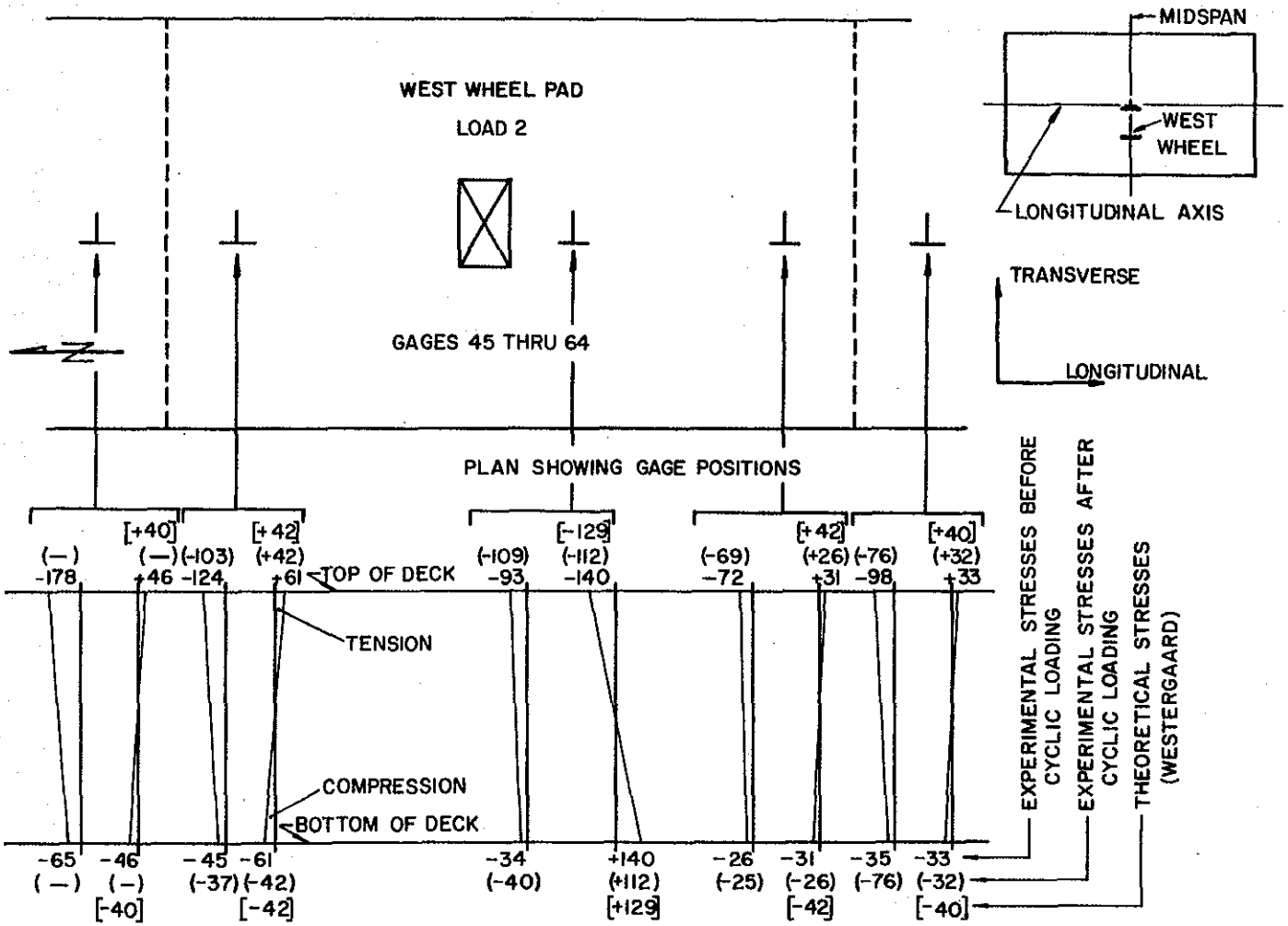

Figure 60. In-plane and Bending Stress Components Computed from Experimental Strains near East Wheel Pad of Load 2.

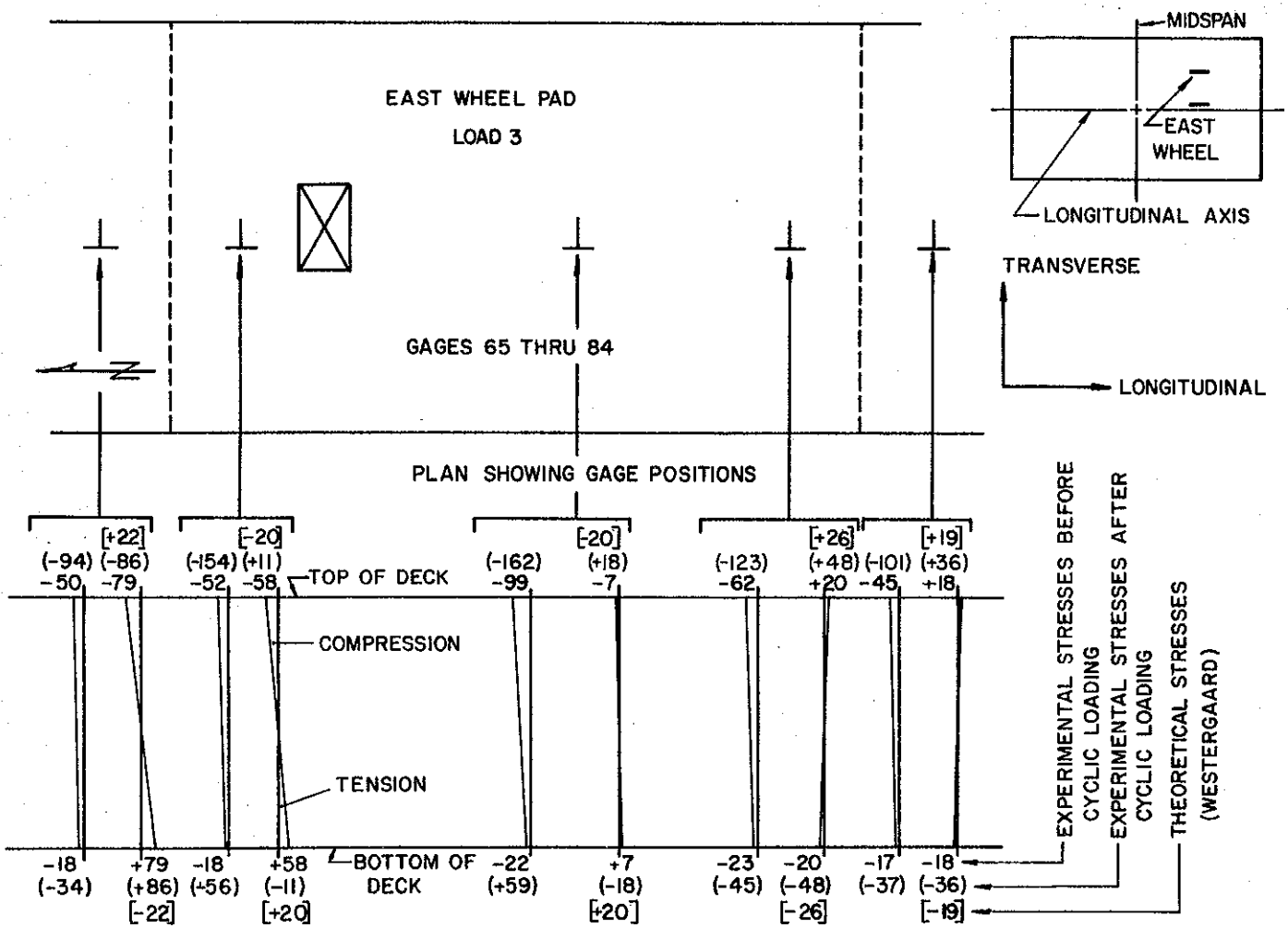

Figure 61. In-plane and Bending Stress Components Computed from Experimental Strains near East Wheel Pad of Load 3.

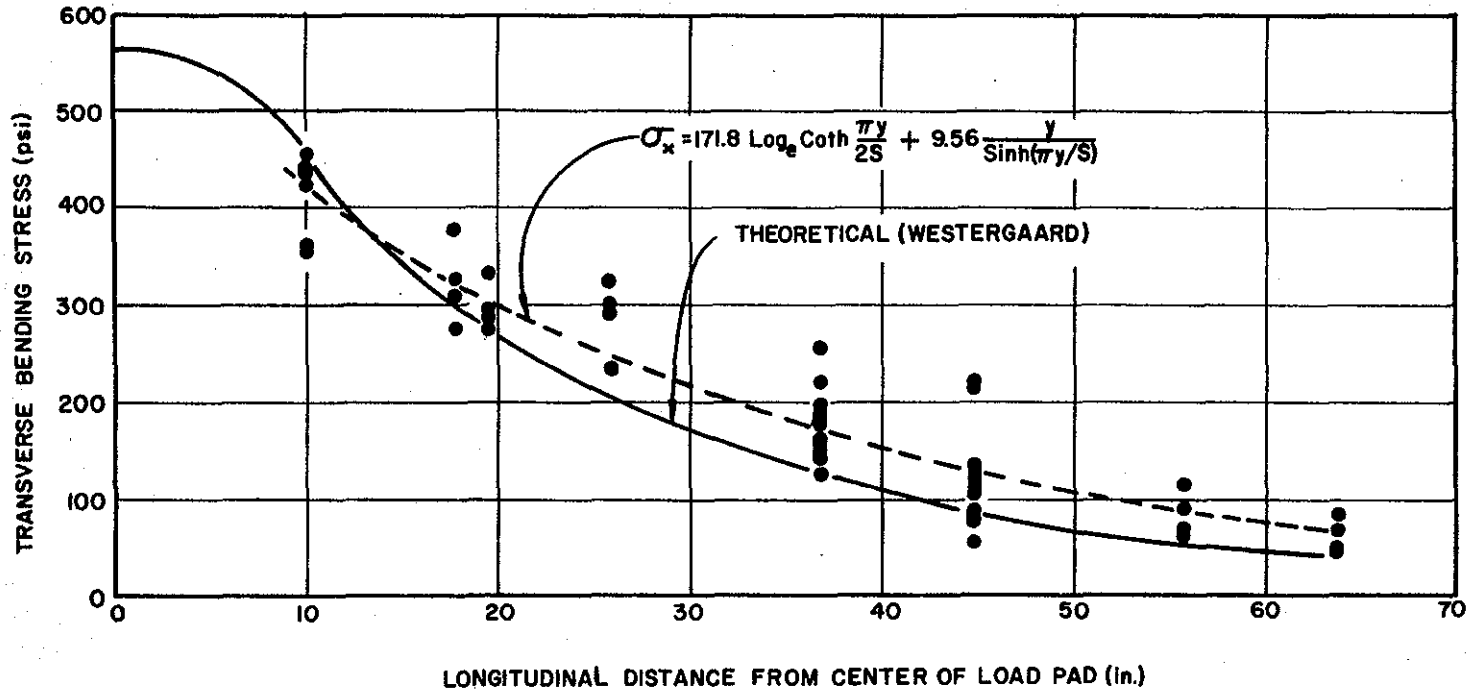

Figure 62. Comparison of Theoretical and Experimental Bending Stresses in Slab in Transverse Direction.

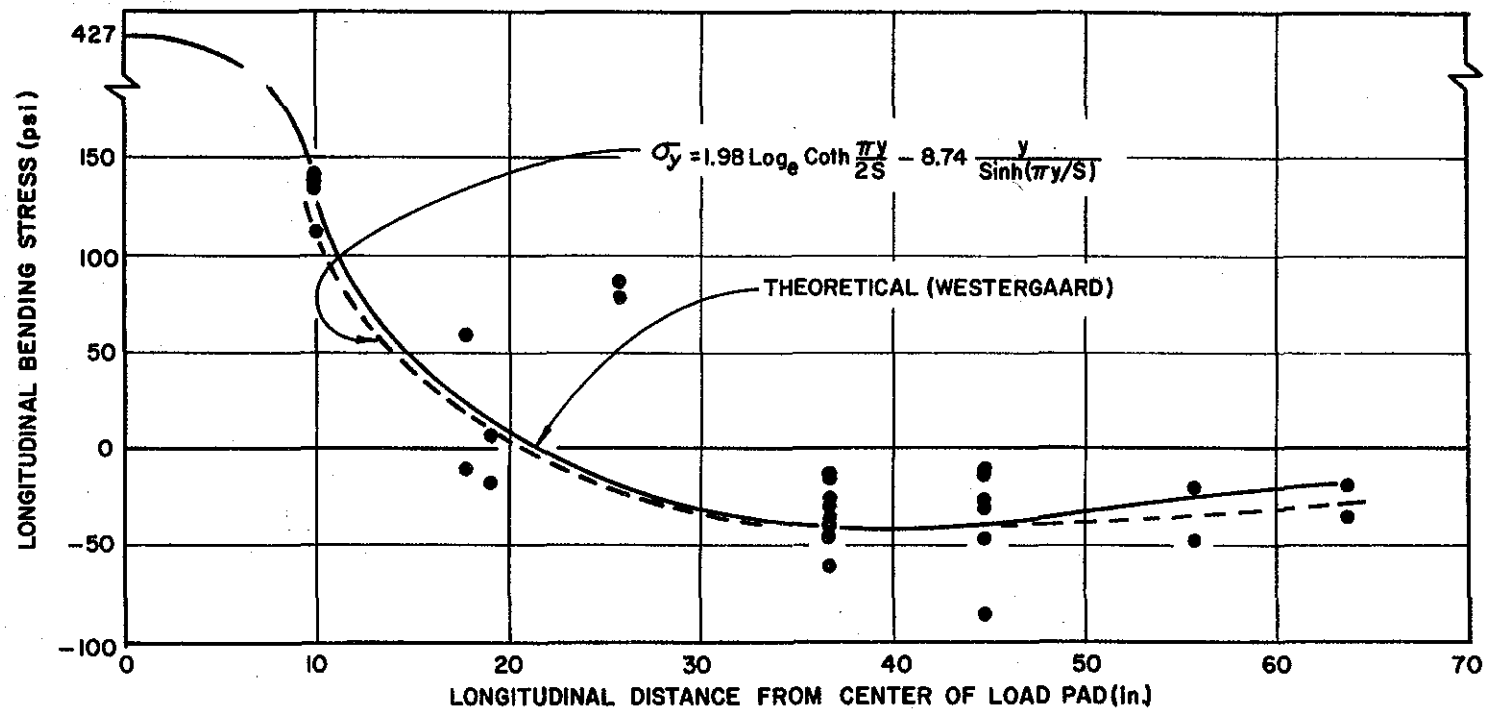

Figure 63. Comparison of Theoretical and Experimental Bending Stresses in Slab in Longitudinal Direction.

These stresses on both the top and bottom surface of the slab were assigned the same sign as the bending moment at that point--compression on the top surface being positive moment. Curves were fitted to the experimental data by the method of least squares to facilitate comparisons between experimental and theoretical values. The function chosen to fit the experimental values was based on the form of the theoretical expressions for bending moments and was:

$$\sigma = C_1 \log_e \operatorname{Coth} \frac{\pi y}{2s} + C_2 \frac{y}{\sinh \frac{\pi y}{s}} \qquad (32)$$

where C_1 and C_2 were constants determined from the least squares fit. Equation (32) is shown in dashed lines in Figures 62 and 63. The maximum difference between the theoretical curve and the least square fit to the data for transverse bending is about 45 psi and is less than 15 psi for longitudinal bending.

Strain readings made before and after application of load 4, a cyclic, alternating wheel load, are given in Table 10 and are compared with theoretical values in Table 11. It is observed that the average ratio of strain readings after cyclic loading to readings before cyclic loading is 1.00 for data obtained with load on the north ram and 0.97 with load on the south ram. Closer observations of the individual gage readings do not indicate any consistent trends in the data for load on the north ram, but do indicate a possible trend in the data for load on the south ram. The after-to-before ratios are consistently low for the top gages and high for the bottom gages. However, the largest difference in strains is

TABLE 10

EXPERIMENTAL STRAINS FOR LOAD 4

Values are in micro in. per in.

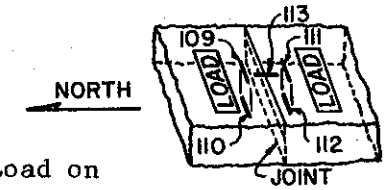

Gage	20.8 kip Load on North Ram			20.8 kip Load on South Ram		
	Before Cyclic Loading	After 2,000,000 Cycles	After / Before	Before Cyclic Loading	After 2,000,000 Cycles	After / Before
109	-94	-97	1.03	-71	-60	0.84
110	+74	+74	1.00	+56	+63	1.13
111	-76	-70	0.92	-100	-78	0.78
112	+62	+63	1.02	+81	+92	1.14
113	-88	-92	1.05	-99	-95	0.96
			Avg. = 1.00			Avg. = 0.97

TABLE 11

EXPERIMENTAL AND THEORETICAL STRAINS FOR LOAD POSITION 4

Strain Gage Identification	Experimental Strain micro in. per in.		Theoretical Strain from Folded Plate Analysis micro. in. per in.
	Before Cyclic Loading	After Cyclic Loading	
	Wheel Load of 20.8 kips on North Ram		
109	-94	-97	-64
110	+74	+74	+67
111	-76	-70	-54
112	+62	+63	+56
113	-88	-92	-31
	Wheel Load of 20.8 kips on South Ram		
109	-71	-60	-53
110	+56	+63	+55
111	-100	-78	-63
112	+81	+92	+66
113	-99	-95	-30

only 22 micro in. per in., and this is not considered to be conclusive evidence of distress. No distress was observed visually. Static failure load test 5 was conducted at this same position, and the ultimate load obtained in this test as compared to other failure tests did not indicate that this area of the slab had been weakened.

Prior to application of load 3, minute cracks were discovered above some transverse joints between panels. The widths of these cracks were measured with a microscope and were found to be 0.002 in. and less. These cracks were not found upon inspection after conclusion of load 2. Some cracks were in the vicinity of a panel joint near the north end of the bridge, far removed from the loads, and it is believed that they were caused by shrinkage or thermal strains, or both, and not due to load. A pattern of these cracks is presented in Figure 64. A limited number of core samples taken after completion of the testing program indicated that some of the cracks extended as deep as 2 in. below the surface, lacking at least 1 1/2 in. of penetrating through the cast-in-place slab.

4.2 Repetitive Load Tests of Slab Segment Model

Table 12 lists the experimentally measured strains on the top surface of the cast-in-place deck and the underside of the prestressed panels. The strains were recorded under static loads and applied before and after the application of an alternating wheel load on either side of the panel joint. If all gages are included in a comparison of strains before and after cyclic loading, ratios of 1.29 and 1.39 are obtained for loads on the north and the south ram

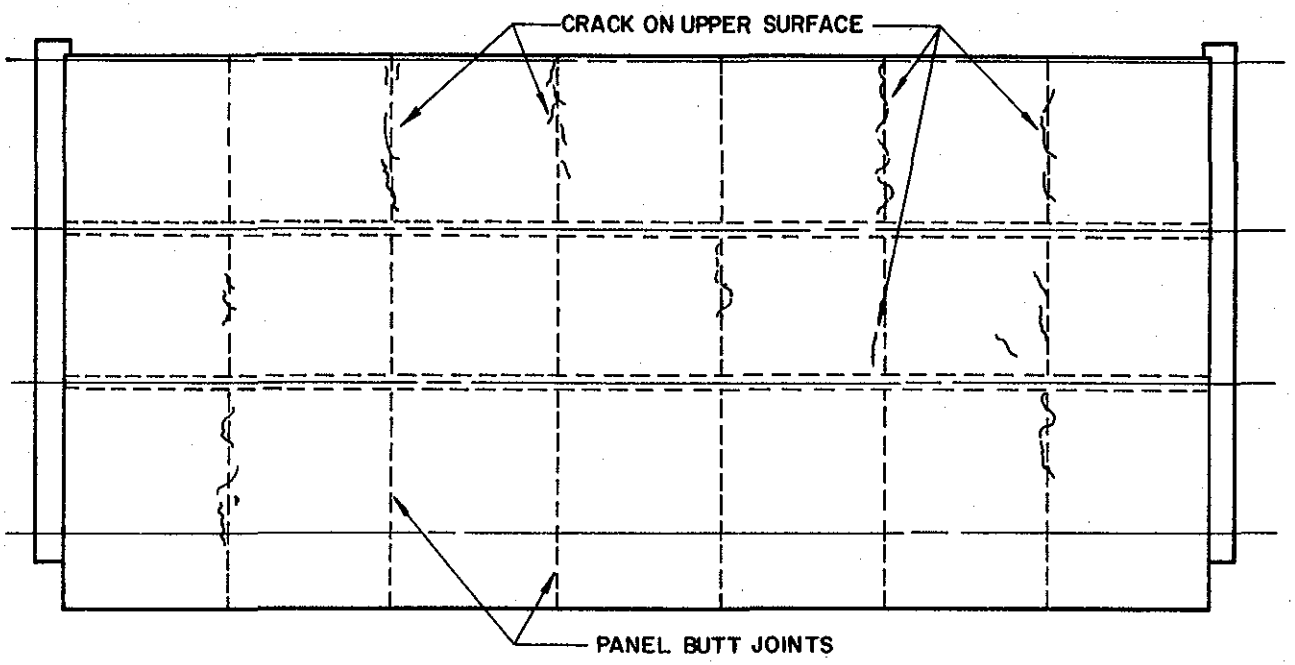

Figure 64. Map of Cracking Pattern.

TABLE 12

EXPERIMENTAL STRAINS FOR LOAD 4A

Values are in micro in. per in.

Gage	20.8 kip Load on North Ram			20.8 kip Load on South Ram		
	Before Cyclic Loading	After 2,000,000 Cycles	After / Before	Before Cyclic Loading	After 2,000,000 Cycles	After / Before
115	-70	-69	.99	-52	-56	1.08
116	+56	+34	.60	+38	+42	1.05
117	-53	-55	1.04	-75	-79	1.05
118	+40	+43	1.01	+64	+66	1.03
119	-18	-18	1.00	-16	-16	1.00
121	+36	+83	2.31	+38	+90	2.37
123	+42	+88	2.10	+40	+87	2.18
			Avg. = 1.29			Avg. = 1.39

respectively. The significant discrepancies from 1.00 are attributable to the two gages adjacent to the slab edges (gages 121 and 123, Fig. 25). If these two gages are removed from the data, the average ratios of strain before cyclic loading to strain after loading drops to .93 and 1.04. No specific cause could be found for the large strain increases recorded by these two gages. The fact that the strains after cycling were approximately twice the values measured before cycling suggests a localized bond failure between prestressed panels and cast-in-place deck. This possibility is questionable, however, since the other strain gages, which were also in high stress areas gave essentially constant readings.

Some transverse cracking in the cast-in-place portion of the deck over the panel joint was observed prior to loading of the slab segment model. They appeared approximately six weeks after the cast-in-place deck was poured, and were unquestionably the result of shrinkage effects. The cracks were of the same general size and extent as those which occurred in the bridge model (Fig. 64).

4.3 Static Load to Failure of Full-Scale Bridge Model

The static failure loads were applied in 10 kip increments, and strain and deflection gage readings were made after each load increment. Cracking in the concrete in each test was first detected on the upper surface of the slab. These cracks occurred in the negative moment regions, on either side of the load, above the inside faces of the adjacent beams. The cracking load varied from 80 to 120 kips

for the four tests. Cracking was observed on the lower surface of the slab, under the load pad, at a load 20 to 30 kips higher than the load causing the first top surface crack. With additional loading, the cracks on both surfaces grew until the load reached 220 to 240 kips. At this load, the rate of progression of the cracks slowed considerably, almost ceasing to extend but opening wider with additional load. The upper surface cracks generally extended parallel to the beams, and eventually, began turning away from the beam into the span of the slab being loaded. The lower surface cracks crossed to form an "X" under the load and extended until they reached the beams. A third crack, much shorter in length, passed through the center of the "X" and extended parallel to the beams. Additional load increments were applied until a punching shear type failure occurred in each case. A typical pattern of the flexural cracking is shown in Figure 65.

The untimate failure surface formed a truncated pyramid, typical of a punching failure in a slab. In tests 5, 6, and 8 the surface showed no apparent influence of the panel butt joint. However, in tests 7 one segment of the surface intersected a panel joint and did not develop in the adjacent panel. Vertical sections through failure surfaces for tests 5 and 7 are given in Figures 66 and 67 respectively.

It is interesting to compare the effective width for this slab with the extent of cracking in the longitudinal direction. The computed effective width was 5 1/2 ft. as compared to the 6 to 7 ft. longitudinal extent of the experimental upper surface cracking. The

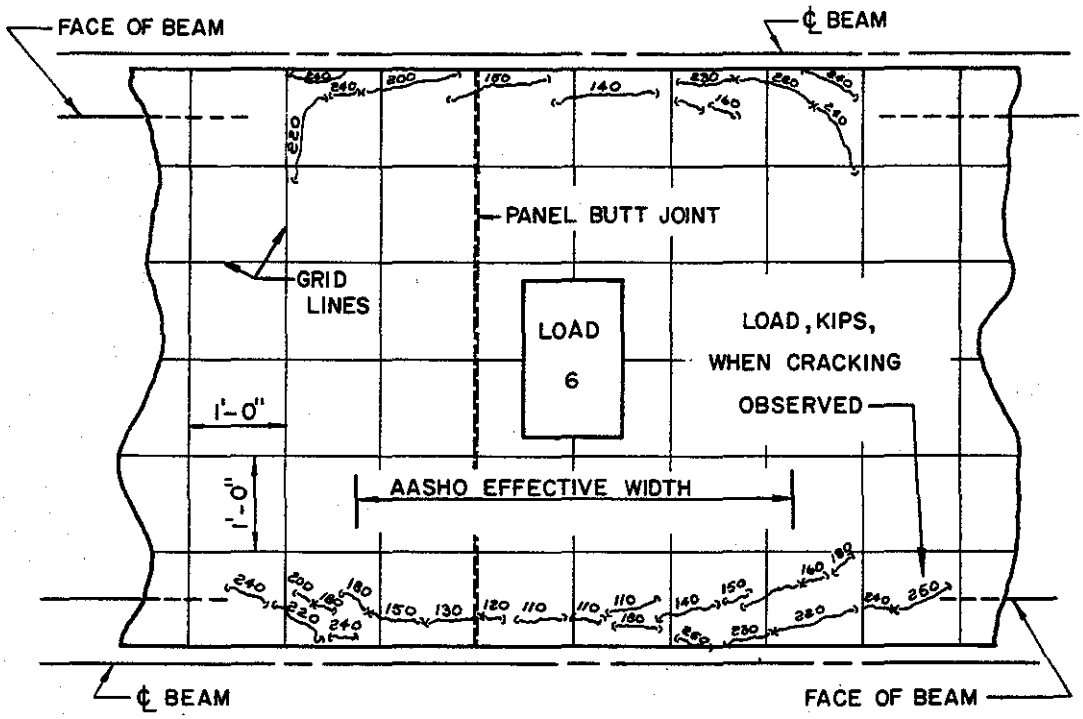

TOP SURFACE

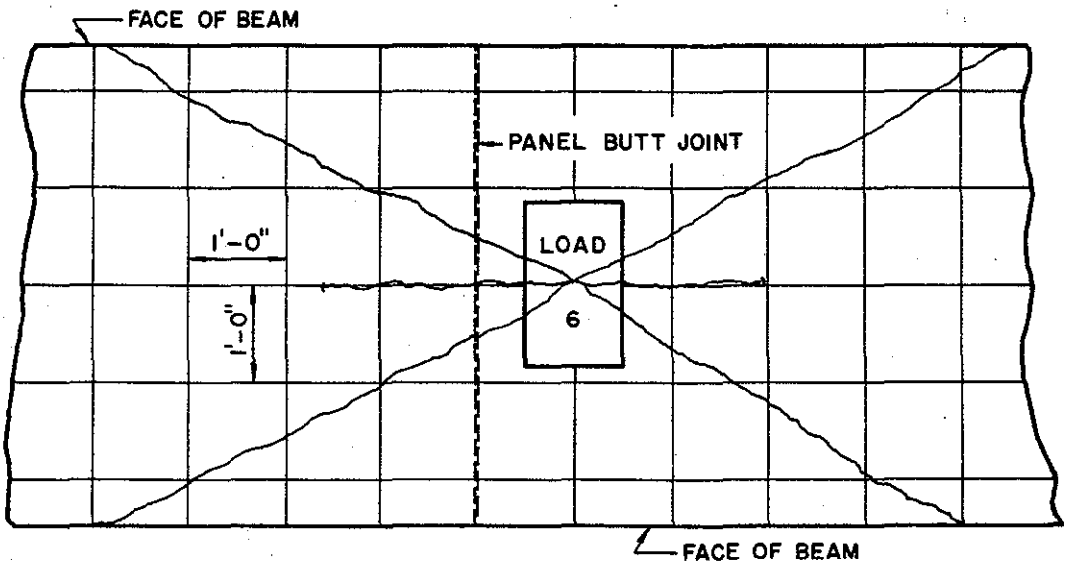

Bottom Surface

Figure 65. Cracking Pattern Developed in Slab in Static Failure Load Test 6 and Typical of Those Obtained in Tests 5 and 8.

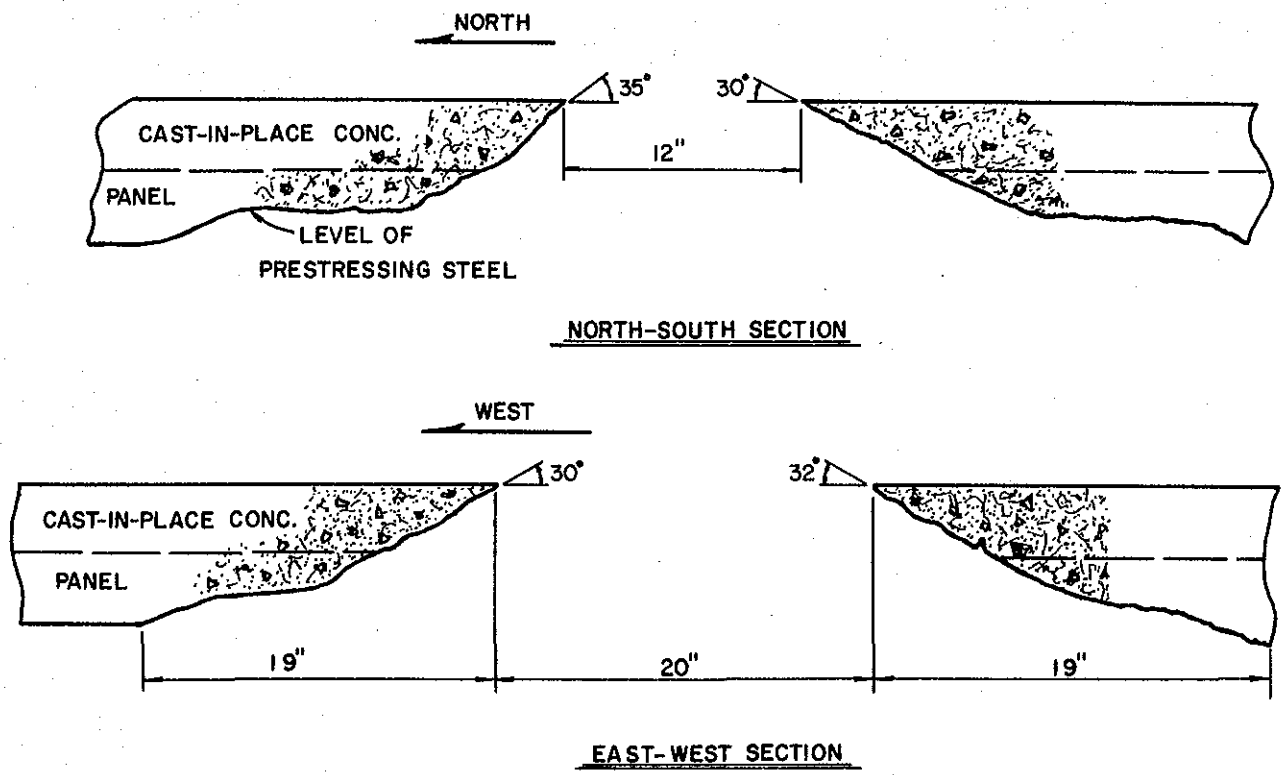

Figure 66. Sections through Failure Surface for Load 5. (Similar failure surfaces were developed in tests 6 and 7.)

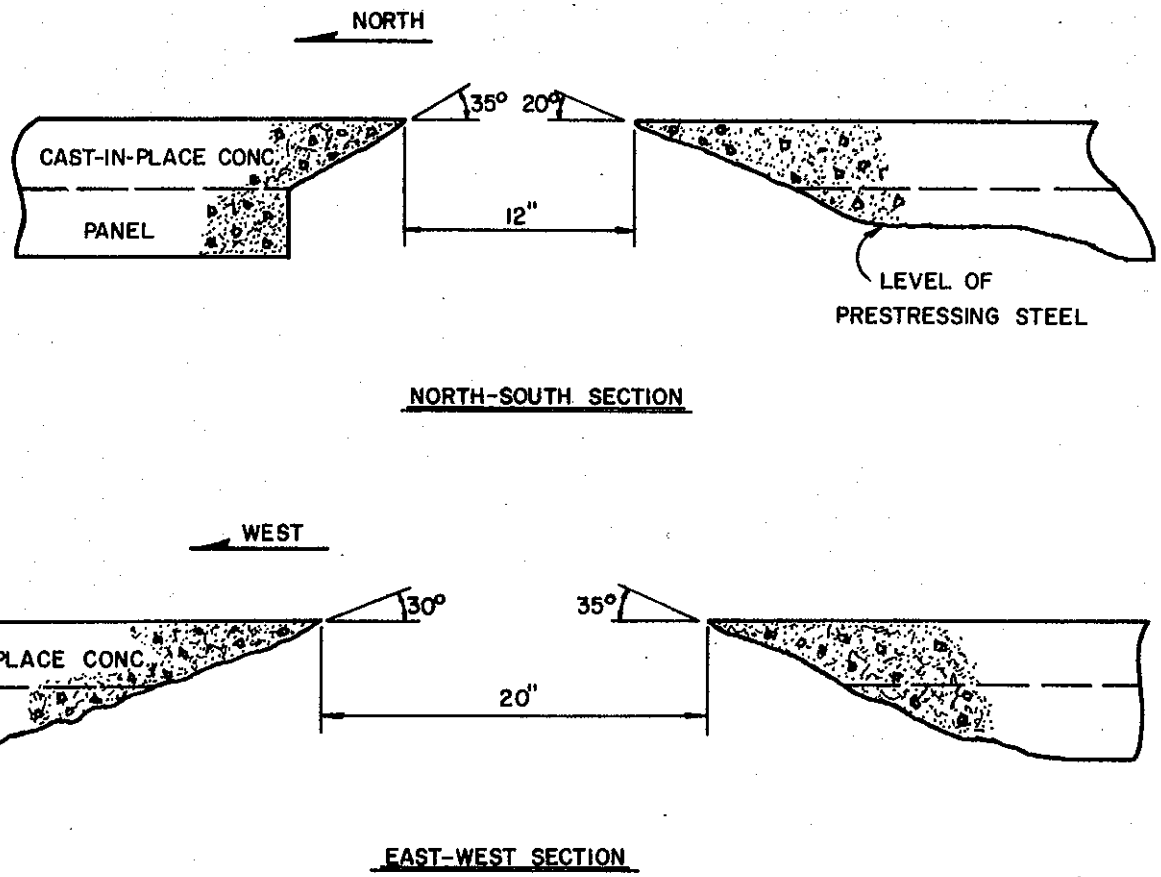

Figure 67. Sections through Failure Surface for Load 7.

effective width of the slab at ultimate strength, then, was about 10 percent greater than the AASHO effective width for working load analysis.

Plots of differential deflection of panels on opposite sides of the panel butt joint adjacent to the load pad are given in Figure 68. The values reflect elastic deformations as well as abrupt deformations resulting from cracking. A summary of the static failure load test results is given in Table 13. Experimental and theoretical values of failure load are compared in Figure 69. A yield line analysis, using a two-fan failure mechanism, was made to determine the theoretical load. This mechanism and its dimensions were selected on the basis of the cracking pattern that was observed in the tests. In this analysis, the slab was transformed into an equivalent ortropically reinforced slab (14). The ultimate load was computed to be 195 kips. Since the failure mode obtained experimentally was not a flexural failure, it can only be said that the ultimate flexural failure load for this slab was greater than the values attained when the punching shear failure occurred. One would have expected the predicted flexural failure load from the yield line analysis to be greater than the 280 kips obtained experimentally, particularly since the analysis results in an upper bound solution. However, this is seen not to be the situation. The first and most obvious factor that could have caused the actual flexural strength of the slab to be greater than that predicted by the yield line analysis is the enhancement of the strength of the slab by in-plane compressive stresses.

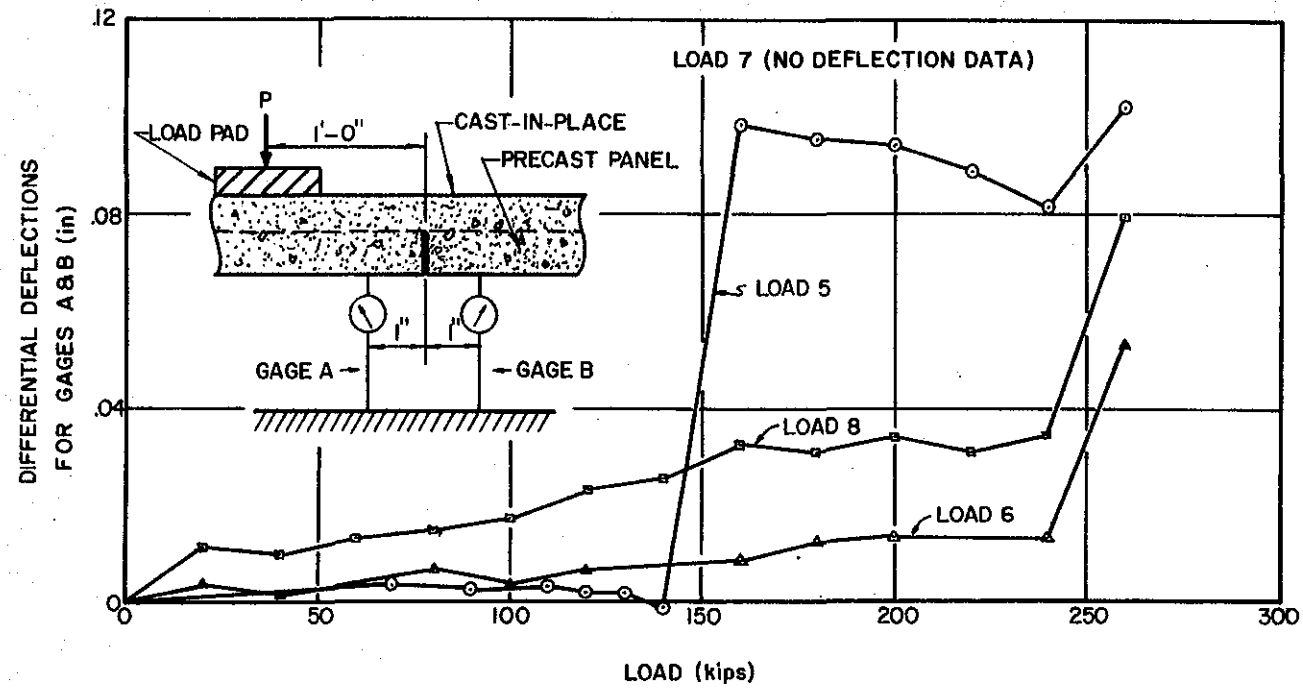

Figure 68. Differential Deflection across Panel Butt Joint vs. Applied Load in Static Failure Load Tests.

TABLE 13

SUMMARY OF STATIC FAILURE LOAD TEST RESULTS

Load Position	Date Tested	Cracking Load (kips)	Failure Load (kips)	Failure Mechanism	Remarks
5	3-09-72	90	270	Punching shear	Significant flexural distress had occurred.
6	2-17-72	110	280	Punching shear	Significant flexural distress had occurred.
7	4-06-72	120	250	Punching shear	Truncated pyramid did not fully develop in adjacent panel.
8	3-23-72	80	260	Punching shear	Significant flexural distress had occurred.

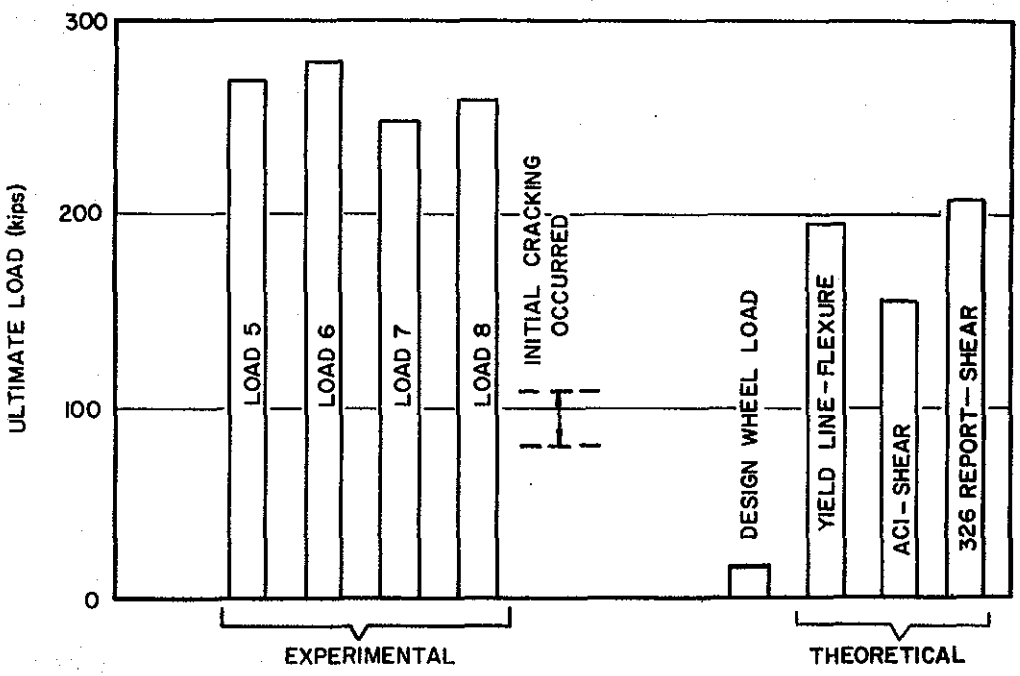

Figure 69. Comparison of Experimental Failure Loads with Theoretical Values.

Such stresses existed in the longitudinal direction of the slab due to bending of the entire structure as composite unit. Another source of in-plane compressive stresses has been observed in lightly reinforced slabs where the failure mechanism is confined to an interior portion of the slab (15, 16). With application of a concentrated load and partial development of the failure mechanism, in-plane extension of the slab occurs in the area of the failure mechanism. This extension is restrained by the surrounding portion of the slab and compressive in-plane stresses are thereby created in the area of the failure mechanism. This phenomenon, in a "rigidly" restrained slab, was observed by Wood (14) to increase the flexural strength of a lightly reinforced slab by 10.9 times. This same phenomenon also enhances the punching shear capacity of a slab (16).

The AASHO Code relationship between a wheel load and the maximum slab bending moment for this structure is $M = 0.18P$. If this relationship is used along with the ultimate moment capacity of the section, an ultimate wheel load can be calculated. This load is somewhat meaningless because the load-moment relationship is intended for an elastic slab, and the relationship would be disrupted by yielding and redistribution of stresses. Nonetheless, such a calculation results in an ultimate load of 123 kips.

The shear strength of concrete slabs is a very complex subject, and at present is handled with semi-empirical methods of analysis. The primary difficulties are the lack of understanding of the behavior

of concrete under multi-axial states of stress and inability to determine the state of stress at any given point in a concrete slab. An analysis of the slab studied here is further complicated by the use of both prestressed and conventionally reinforced concrete. The American Concrete Institute (ACI) (17) Code provisions for slabs and footings specify that the nominal shear stress for two-way action (neglecting the capacity reduction factor) be computed by $v_u = V_u/bd$, and this shear stress is specified not to exceed $4\sqrt{f'_c}$. If the average value of compressive strength for the slab from Table 2 is used, this method predicts the ultimate load, V_u, to be 140 kips if a panel butt joint is assumed, and 156 kips is no joint is assumed. The experimental failure surface did not intersect the panel joint in tests 5, 6 and 8, and the results of these tests should be compared with the predicted value of 156 kips. It should be realized that the ACI Code provision is a simplified design equation intended to provide a lower bound on the ultimate load. An equation which more closely approximates the lower bound of experimental data than does $4\sqrt{f'_c}$ is (18):

$$v_u = 4(d/r + 1)\sqrt{f'_c} \qquad (33)$$

Where: d = the effective depth of the slab

r = side dimension of the loaded area

This equation results in an ultimate shear strength of 457 psi if the average compressive strength for the slab is used. The resulting ultimate punching shear loads are 186 kips and 210 kips for the con-

ditions of an assumed joint and no assumed joint respectively. Experimental values, given in Table 13, exceed these theoretical values by 25 to 35 percent. Experimental values given in the ACI Committee Report (18) exceed the theoretical values by zero to 100 percent.

4.4 Static Load to Failure of Slab Segment Model

The static failure load was applied in 10 kip increments, with data being recorded after each load increment. Negative moment cracks initially occurred on the upper surface of the deck above the vertical faces of the beams nearest the loading pad. As loading progressed, the cracking extended the full length of the slab in the longitudinal direction of the beams. Upon further application of load, new cracks began to branch from these and eventually formed a curcular pattern around the loading pad. The circular crack pattern was disrupted on the west side of the loading pad where it intersected the edge of the structure. Two flexural tensile cracks initiated on the bottom face of the panel under the load pad and eventually extended the full width of that panel. No cracking was detected in the adjacent panel. At a load of 185 kips, it became necessary to release the load and place a thicker bearing pad between the loading ram and the testing frame. On reapplication of load, a punching shear failure occurred at 155 kips. The shear failure surface formed a truncated pyramid, similar to those observed during the full-scale bridge model tests.

4.5 Assessment of Panel Butt Joint Performance

A comparison between measured strains and those predicted from elastic analysis (Tables 7 through 11) are in rather poor agreement for longitudinal strains in the vicinity of butt joints between panels. This result was expected, since the folded plate analysis used to predict strains did not include the effect of this discontinuity in the slab. The discrepancy is most apparent for those cases where the load is in a position which causes a great deal of localized bending in the slab adjacent to a joint (load positions 3 and 4). For loading 4, the longitudinal compressive strain on the top of the deck, directly over the butt joint (Table 11, gage 113), were approximately three times greater than those predicted by elastic analysis. At the joint, most likely only the cast-in-place portion of the deck is effective in resisting longitudinal stress. At joints toward the ends of the bridge, where in-plane compressive stresses due to the overall bending of the bridge are relatively small, the localized bending of the slab adjacent to wheel load should produce tensile stresses in the underside of the cast-in-place slab that are approximately equal to the compressive stresses in the top of the deck. In spite of this concentration of tensile stresses at the bottom of the cast-in-place deck, no tendency toward premature cracking was observed. Several core samples and the observed failure surfaces after ultimate load (Figs. 66 and 67) showed no inherent weakness in the joint.

During the simulated service load testing phase of this investi-

gation, cracks in the upper surface of the cast-in-place deck, directly over butt joints between panels, were detected (Fig. 64). Since these cracks were small (.002 in. or less in width), occurred in both loaded and unloaded areas of the deck, and did not appear until several months after construction of the bridge, they most likely were formed through shrinkage and thermal effects. Cores taken after ultimate load tests of the structure indicated that the average depth of these cracks was approximately half the depth of the cast-in-place slab. In only one of the four ultimate load tests (load no. 7) was there any evidence that these cracks involved in the final failure of the deck (Fig. 67).

Similar crack patterns in the top surface of the cast-in-place deck were observed in an inspection of two existing bridges of the same type of construction as the full-scale laboratory model (Reference (2), Appendix A). Cores taken from those bridges indicated that the cracks also extended approximately half way through the cast-in-place portion of the deck. Load tests on one of the bridges indicated that transfer of wheel loads across the joints was unaffected by the presence of these cracks.

The diaphrams used in these two bridges were positioned so that they provided a transverse line of support for the deck. The shorter end spans of each bridge contained one line of diaphrams, while the longer interior spans contained two rows of diaphrams. With this type of diaphram arrangement, negative longitudinal moments are developed in the deck on both sides of the diaphram as wheel loads

move along the bridge. The magnitude of these localized longitudinal bending moments are fairly independent of the position of the wheel along the span. The substantial positive longitudinal moment produced in the deck by the overall bending of the bridge tends to cancel the localized negative moment produced as the wheel approaches a diaphram, when the load and diaphram are in the central portion of the span, and the span is sufficiently long to produce large overall positive bending moments. The net result is that the top surface of the deck is subjected only to compressive stresses. For shorter spans, and for regions adjacent to either end of longer spans, the compressive stresses in the top of the deck produced by overall bending of the bridge are not as large as the tensile stresses produced by localized bending of the deck adjacent to diaphrams. This results in longitudinal tensile stresses which can, under sufficiently high loads, cause transverse cracks to form in the top of the deck. If these cracks have already been initiated by shrinkage and thermal effects, as appears to be the case when prestressed panel, cast-in-place deck construction is used, these tensile stresses will cause the cracks to open and propagate under service load conditions.

This phenomenon can be observed in the nature and extent of the crack patterns found on the two in-service bridges which were inspected. The transverse cracks were more frequent and more severe along the wheel paths of the more heavily traveled traffic lane. The frequency of cracks was also higher for the shorter end spans, and toward either end of the longer interior spans.

The full-scale bridge model tested in the laboratory had one line of diaphrams at center-span, positioned so that they did not support the deck. As a result, no longitudinal tensile strains in the top of the cast-in-place deck were observed for any of the load tests, not was there any tendency for the transverse shrinkage cracks to grow and propagate under load.

4.6 Assessment of Shear, Bond and Load Transfer Performance

Mechanical shear connectors (Z-bars) and special surface treatment (grouting) were used in certain areas of the bridge deck (Fig. 13) to determine if they would enhance the bond between prestressed panel and cast-in-place deck. Dowel bars (Fig. 13) and dowel bars plus V-bars (Figs. 16 and 17) were located over some panel butt joints to determine if they would assist in transferring wheel loads across the joint.

The results of the load tests performed indicate that none of these details provide any measurable improvement in the performance of a bridge. Under the action of simulated service load conditions, no consistent distinguishing trends in measured strains (Tables 7 through 11) could be found to indicate superior performance, in terms of bond or load transfer, of one area of the deck over another. The range in values of failure load was 30 kips, which is only 12 percent of the lowest failure load. Recalling that load positions 5 and 6 (highest failure loads) were in areas where no grout, Z-bars, or dowels were employed leads to the conclusion that ultimate load

capacity of the deck was not enhanced by these special detials. The loads at which cracking first occurred were not greatly different, and the modes of failure were similar in all cases except load 7.

It is readily observed that the load at which cracking occurred and the ultimate load far exceeded the design wheel load. The lowest value of cracking load obtained experimentally was 3.8 times the design wheel load plus impact, the lowest ultimate load obtained experimentally was 12 times the design wheel load plus impact.

V. SUMMARY AND CONCLUSIONS

A full-scale bridge model and a slab segment model were evaluated experimentally in the laboratory and theoretical studies of the bridge model were made. The structures were subjected to cyclic simulated service loads and static failure loads.

The full-scale bridge model was designed in accordance with the provisions for conventional concrete slab and prestressed beam bridges of the AASHO Specifications. A rigorous elastic analysis of the bridge model was performed, assuming that prestressed beams, prestressed panels and cast-in-place deck behaved as a full composite unit. Strains predicted by analysis were compared with measured strains at various locations on the deck after application of static wheel loads. A comparison between measured and predicted strains and between strains measured before and after cyclic loading were examined to detect indications of bond failure between prestress panel and cast-in-place deck in the vicinity of the applied loads. Mechanical gages were also installed on the underside of the bridge deck to detect any relative motion between adjacent prestressed panels or between prestressed panels and the beams which supported them. Such motion would be possible only after bond failure between panels and cast-in-place deck or between panels and beams. An inspection of the data obtained from both types of instrumentation for both the full-scale bridge model and the slab segment model revealed no indications of bond failure in

either structure as a result of cyclic loading.

Several special reinforcing details and a special prestressed panel surface preparation were studied to determine if they would provide an improvement in the performance of the bridge. The results of the testing program indicate that such devices and preparations do not enhance performance. Under service load conditions, no distinction in performance between areas of the bridge deck with special reinforcing or surface treatment and those areas without them could be made. In static load to failure tests, the areas of the deck which required the greatest load to initiate significant cracking were those without special treatment or reinforcing. The failure load and mechanism for final failure of the deck appeared to be independent of the area of the deck where they were applied. Although no comparisons of the performance of the slab segment model with an identical structure without dowel and V-bar reinforcing of the butt-joint could be made, the test results gave no indication of superior performance as a result of these special reinforcing details.

A simplified prediction of the ultimate flexural strength of the bridge deck was made using yield line theory. The load predicted to cause flexural failure was considerably below all failure loads obtained from tests. In addition, the mode of failure observed in all tests was not flexural, but punching shear. A prediction of load at failure by the punching shear mode, based on the recommendations of

an ACI Committee Report (18) also gave very conservative results.

The following conclusions are drawn from the results of the theoretical and experimental work reported herein.

1. The bond at the interface between the prestressed, precast panels and the cast-in-place concrete performed well, with no indication of distress under cyclic design loads and static failure loads.

2. No distinction in performance between those areas of the deck with mechanical shear connectors (Z-bars) and grouting treatment, and those areas without could be made for 2 million cycles of design load or for static load to failure tests.

3. Wheel loads were transferred and distributed across transverse panel butt joints in a satisfactory manner. Those joints reinforced with dowel bars gave no indication of superior performance under 2 million cycles of alternating service wheel loads or static failure loads, when compared with those joints without special reinforcing.

4. With this type of construction, some small transverse cracking in the cast-in-place deck over panel butt joints is to be expected as a result of thermal and shrinkage effects. Such cracks have not been found to be detrimental to the overall performance of a bridge. Interior diaphrams should be positioned so that they do not provide a transverse line of support for the deck. If the diaphrams do support the slab, they produce negative longitudinal bending moments which tend to expedite the growth and propagation of these transverse cracks.

5. The full scale bridge model was designed in accordance with AASHO Specifications for conventional slab and prestressed beam construction. No special precautions were taken in the design to reflect the presence of a prestressed panel-cast-in-place slab interface or of the butt joint between panels. The only distinction between this design and conventional design was the calculations to determine the prestressed panel dimensions and reinforcing. The resulting bridge performed satisfactorily for all load tests.

REFERENCES

1. Standard Specifications for Highway Bridges, Tenth Edition, American Association of State Highway Officials, Washington, D. C., 1969.

2. Jones, H. L. and Furr, H. L., "Study of In-Service Bridges Constructed with Prestressed Panel Sub-Deck," Research Report 145-1, Texas Transportation Institute, Texas A&M University, July 1970.

3. Jones, H. L. and Furr, H. L., "Development Length of Strands in Prestressed Panel Sub-Decks," Research Report 145-2, Texas Transportation Institute, Texas A&M Univeristy, December 1970.

4. Sinno, R. and Furr, H. L., "A Study of Reinforced Concrete Bridge Deck Deterioration: Repair," Research Report 130-1, Texas Transportation Institute, Texas A&M University, March 1969.

5. Nossier, S. B. and Murtha, R. N., "Ultimate Horizontal Shear Strength of Prestressed Split Beams," Technical Report R707, Naval Civil Engineering Laboratory, Port Hueneme, California, January 1971.

6. Standard Specifications for Road and Bridge Construction, Texas Highway Department, Austin, Texas, January 1962.

7. Erps, H. R. and Googins, A. L., "Distribution of Wheel Loads and Design of Reinforced Concrete Bridge Floor Slabs," Public Roads, Vol. 18, No. 8, October 1937.

8. Westergaard, H. M., "Computation of Stresses in Bridge Slabs Due to Wheel Loads," Public Roads, Vol. 11, No. 1, March 1930.

9. Kelley, E. F., "Effective Width of Concrete Bridge Slabs Supporting Concentrated Loads," Public Roads, Vol. 7, No. 1, March 1926.

10. Goldberg, J. E. and Leve, H. L., "Theory of Prismatic Folded Plate Structures," International Association for Bridge and Structural Engineering Publications, Vol. 16, 1957, pp. 59-86.

11. Timoshenko, S. and Woinowsky-Krieger, S., Theory of Plates and Shells, McGraw Hill Book Co., Inc., New York, 1959, pp. 135.

12. Gustafson, W. C. and Wright, R. N., "Analysis of Skewed Composite Girder Bridges," Journal of the Structural Division, ASCE, Vol. 94, No. ST4, April 1968, pp. 919.

13. Jensen, V. P., "Solutions for Certain Rectangular Slabs Continuous Over Flexible Supports," Bulletin No. 303, Engineering Experiment Station, University of Illinois, Urbana, Illinois, June 1938.

14. Wood, R. H., "Plastic and Elastic Design of Slabs and Plates," Ronald Press So., New York, 1961.

15. Jacobson, Ammon, "Membrane-Flexural Failure Modes of Restrained Slabs," Journal of the Structural Division, ASCE, Vol. 93, No. ST5, October 1967.

16. Batchlor, B. De V. and Tong, P. Y., "An Investigation of the Ultimate Shear Strength of Two-way Continuous Bridge Slabs Subjected to Concentrated Loads," Report on Project Q-43, Department of Civil Engineering, Queen's University, Kingston, Ontario, September 1970.

17. Building Code Requirements for Reinforced Concrete, (ACI 318-71) American Concrete Institute, Detroit, Michigan 1971.

18. ACI-ASCE Committee 426 (326), "Shear and Diagonal Tension," ACI Journal. Vol. 59, No. 1-3, January-March 1962, pp. 1-30, 277-334, and 352-396.

APPENDIX A

A.1 Expressions for Fixed-edge Forces in Equation (23)

The parameters P, α, β, η, ξ, a, b, and h are defined in Figure 46. Additional parameters contained in the fixed-edge force expressions are listed below.

η = Poisson's ratio for plate material

E = modulus of elasticity of plate material

$$D = \frac{Eh^3}{12(1-\eta^2)}$$

$$T = \frac{Eh}{(1+\eta)^2}$$

$$\alpha_m = \frac{m\pi b}{2a}$$

$$q_m = \frac{16P}{\pi^2\alpha\beta m} \sin\frac{m\pi\xi}{a} \sin\frac{m\pi\alpha}{2a}$$

$$a_n^A = \frac{1}{n} \sin\frac{n\pi\eta}{b} \sin\frac{n\pi\beta}{2a}$$

$$a_n^S = \frac{1}{n} \cos\frac{n\pi\eta}{b} \sin\frac{n\pi\beta}{2b}$$

$$Q_{mn}^A = \frac{a_n^A}{D[(\frac{m\pi}{a})^2 + (\frac{n\pi}{b})^2]^2}$$

$$Q_{mn}^S = \frac{a_n^S}{D[(\frac{m\pi}{a})^2 + (\frac{n\pi}{b})^2]^2}$$

$$\lambda_{1m} = (\alpha_m \operatorname{sech}\alpha_m + \sinh\alpha_m)^{-1}$$

$$\lambda_{2m} = (\alpha_m \operatorname{csch}\alpha_m - \cosh\alpha_m)^{-1}$$

$$k_{tm} = \alpha_m \tanh\alpha_m$$

$$k_{cm} = \alpha_m \coth\alpha_m$$

$$B_m = \lambda_{1m}\, q_m \frac{a}{mb} \sum_{n=1,3,\ldots} Q_{mn}^S \sin(n\tfrac{\pi}{2})$$

$$A_m = -k_{tm}\, B_m$$

$$D_m = \lambda_{2m}\, q_m \frac{a}{mb} \sum_{n=2,4,\ldots} n\, Q_{mn}^A \cos(n\tfrac{\pi}{2})$$

$$B_m = -k_{cm}\, D_m$$

The fixed-edge forces are given by

$$M_{fijm} = D(\tfrac{m\pi}{a})^2\{(1-\eta)A_m\cosh\alpha_m + [2\cosh\alpha_m + (1-\eta)\alpha_m\sinh\alpha_m]B_m + (1-\eta)$$

$$C_m \sinh\alpha_m + [2\sinh\alpha_m + (1-\eta)\alpha \cosh\alpha_m]D_m - q_m \sum_{n=1,3,\ldots}[(\frac{an}{bm})^2 + \eta] \cdot$$

$$Q^S_{mn}\cos(n\tfrac{\pi}{2}) - q_m \sum_{n=2,4,\ldots}[(\frac{an}{mb})^2 + \eta]Q^A_{mn}\sin(n\tfrac{\pi}{2})\}\sin\frac{m\pi x}{a} \qquad \text{(A-1)}$$

$$M_{fjim} = D(\frac{m\pi}{a})^2\{-(1-\eta)A_m\cosh\alpha_m - [2\cosh\alpha_m + (1-\eta)\alpha_m\sinh\alpha_m]B_m +$$

$$(1-\eta)C_m\sinh\alpha_m + [2\sinh\alpha_m + (1-\eta)\alpha_m\cosh\alpha_m]D_m + q_m \sum_{n=1,3,\ldots}[(\frac{an}{bm})^2 + \eta] \cdot$$

$$Q^S_{mn}\cos(n\tfrac{\pi}{2}) - q_m \sum_{n=2,4,\ldots}[(\frac{an}{bm})^2 + \eta]Q^A_{mn}\sin(n\tfrac{\pi}{2})\}\sin\frac{m\pi x}{a}$$

$$V_{fijm} = D(\frac{m\pi}{a})^3\{(\eta-1)A_m\sinh\alpha_m + [(1+\eta)\sinh\alpha_m + (\eta-1)\alpha_m\cosh\alpha_m]B_m + (\eta-1) \cdot$$

$$C_m\cosh\alpha_m + [(1+\eta)\cosh\alpha_m + (\eta-1)\alpha_m\sinh\alpha_m]D_m + q\frac{a\pi}{mmb}\sum_{n=1,3,\ldots}[(\frac{an}{mb})^2 + 2-\eta] \cdot$$

$$nQ^S_{mn}\sin(n\tfrac{\pi}{2}) - q\frac{a}{mnb}\sum[(\frac{an}{mb})^2 + 2 - \eta]nQ^A_{mn}\cos(n\tfrac{\pi}{2})\}\sin\frac{m\pi x}{a}$$

$$V_{fjim} = D(\frac{m\pi}{a})^3\{(\eta-1)A_m\sinh\alpha_m + [(1+\eta)\sinh\alpha_m + (\eta-1)\alpha_m\cosh\alpha_m]B_m - (\eta-1) \cdot$$

$$C_m\cosh\alpha_m - [(1+\eta)\cosh\alpha_m + (\eta-1)\alpha_m\sinh\alpha_m]D_m + q\frac{a}{mmb}\sum_{n=1,3,\ldots}[(\frac{an}{mb})^2 + 2-\eta] \cdot$$

$$nQ^S_{mn}\sin(n\tfrac{\pi}{2}) + q\frac{a}{mmb}\sum_{n=2,4,\ldots}[(\frac{an}{mb})^2 + 2 - \eta]nQ^A_{mn}\cos(n\tfrac{\pi}{2})\}\sin\frac{m\pi x}{a}$$

A.2 Expressions for Constants C_{kijm} in Equation (23)

Using these quantities

$$C1 = (\alpha_m \text{sech}\alpha_m + \sinh\alpha_m)^{-1} \qquad C5 = (\alpha_m \text{sech}\alpha_m - \frac{3-\eta}{1+\eta} \sinh\alpha_m)^{-1}$$

$$C2 = (\alpha_m \text{csch}\alpha_m - \cosh\alpha_m)^{-1} \qquad C6 = (\alpha_m \text{csch}\alpha_m + \frac{3-\eta}{1+\eta} \cosh\alpha_m)^{-1}$$

$$C3 = (\alpha_m \text{sech}\alpha_m - \sinh\alpha_m)^{-1} \qquad C7 = (\alpha_m \text{csch}\alpha_m - \frac{3-\eta}{1+\eta} \cosh\alpha_m)^{-1}$$

$$C4 = (\alpha_m \text{csch}\alpha_m + \cosh\alpha_m)^{-1} \qquad C8 = (\alpha_m \text{sech}\alpha_m + \frac{3-\eta}{1+\eta} \sinh\alpha_m)^{-1}$$

the constants are given by

$$C_{1ijm} = -[C1\cosh\alpha_m + C2\sinh\alpha_m] \frac{m\pi}{a} D \qquad \text{(A-2)}$$

$$C_{2ijm} = -[C1\cosh\alpha_m + C2\sinh\alpha_m] \frac{m\pi}{a} D$$

$$C_{3ijm} = [C4\cosh\alpha_m - C3\sinh\alpha_m - (1-\eta)] (\frac{m\pi}{a})^2 D$$

$$C_{4ijm} = -[C4\cosh\alpha_m + C3\sinh\alpha_m] (\frac{m\pi}{a})^2 D$$

$$C_{5ijm} = C_{3ljm}$$

$$C_{6ijm} = C_{4ijm}$$

$$C_{7ijm} = [C4\sinh\alpha_m - C3\cosh\alpha_m] (\frac{m\pi}{a})^3 D$$

$$C_{8ijm} = [C4\sinh\alpha_m + C3\cosh\alpha_m] (\frac{m\pi}{a})^3 D$$

$$C_{9ijm} = [-C5\cosh\alpha_m + C6\sinh\alpha_m] (\frac{m\pi}{a}) T$$

$$C_{10ijm} = [C5\cosh\alpha_m + C6\sinh\alpha_m] (\frac{m\pi}{a}) T$$

$$C_{11ijm} = [C7\cosh\alpha_m - C8\sinh\alpha_m + (1+\eta)] (\frac{m\pi}{a}) T$$

$$C_{12ijm} = -[C7\cosh\alpha_m + C8\sinh\alpha_m] (\frac{m\pi}{a}) T$$

$$C_{13ijm} = C_{11ijm}$$

$$C_{14ijm} = C_{12ijm}$$

$$C_{15ijm} = [- C7\sinh\alpha_m + C8\cosh\alpha_m] \left(\frac{m\pi}{a}\right) T$$

$$C_{16ijm} = [C7\sinh\alpha_m + C8\cosh\alpha_m] \left(\frac{m\pi}{a}\right) T$$

A.3 Expressions for Constants B_{kim} in Equation (26)

The constants are defined in terms of the parameters

$\bar{d}$ = distance from center of gravity of beam cross section to top face of beam

$\bar{h}$ = thickness of two slabs which beam supports

E = modulus of elasticity of beam material

G = shear modulus of beam material

J = polar moment of inertia of cross section

I_Z = moment of inertia about the Z-axis (see Fig. 47)

I_y = moment of inertia about the y-axis

A = cross sectional area of beam

giving

$$B_{1im} = \left(\frac{m\pi}{a}\right)^4 (\bar{d}^2 + \bar{d}\bar{h} + \bar{h}^2/4)\, EI_Z + \left(\frac{m\pi}{a}\right)^2 GJ \qquad \text{(A-5)}$$

$$B_{2im} = - \left(\frac{m\pi}{a}\right)^4 (\bar{d} + \bar{h}/2)\, EI_Z$$

$$B_{3im} = - \left(\frac{m\pi}{a}\right)^4 [EI_y + EA(\bar{d}^2 + \bar{d}\bar{h} + \bar{h}^2/4)]$$

$$B_{4im} = \left(\frac{m\pi}{a}\right)^3 EA\, (\bar{d} + \bar{h}/2)$$

$$B_{5im} = \left(\frac{m\pi}{a}\right)^4 EI_Z \left(\bar{d} + \bar{h}/2\right)$$

$$B_{6im} = -\left(\frac{m\pi}{a}\right)^4 EI_Z$$

$$B_{7im} = EA \left(\frac{m\pi}{a}\right)^3 \left(\bar{d} + \bar{h}/2\right.$$

$$B_{8im} = -EA \left(\frac{m\pi}{a}\right)^2$$